

‘Investigating the use of Raman spectroscopy as a histopathological tool to identify metastatic brain tumours and their sites of origin’

by

Leanne M. Fullwood

A thesis submitted in partial fulfilment for the requirements for the degree of Master of Science (by Research) at the University of Central Lancashire

November 2013

Student Declaration

Concurrent registration for two or more academic awards

I declare that while registered as a candidate for the research degree, I have not been a registered candidate or enrolled student for another award of the University or other academic or professional institution

Material submitted for another award

I declare that no material contained in the thesis has been used in any other submission for an academic award and is solely my own work

Signature of Candidate



Type of Award

Master of Science (by Research)

School

School of Forensic and Investigative Sciences

Abstract

It is reported that 13,000 people in the UK are diagnosed with tumours in the brain every year, of which 60% are metastatic. Current methods for diagnosing the disease can be subjective, invasive and have long diagnostic windows. Raman spectroscopy provides a non-destructive, non-invasive, rapid and economical method for diagnosis.

The aim of this study was to assess the use of Raman and immersion Raman spectroscopy for diagnosing metastatic brain and glioblastoma multiforme tumours and identifying primary sites of origin, and investigate the substrate effect on sample preparation and resultant spectra.

The tissue specimens used in this study were formalin fixed-paraffin preserved and were supported on spectroscopic substrates for analysis. Samples were dewaxed prior to analysis to reduce/eliminate the paraffin contributions in the Raman spectra. The substrate was shown to have a significant influence on this dewaxing procedure and thus resulting spectra. It was also observed that specimens on CaF₂ and Spectrosil quartz retained paraffin after dewaxing, whereas specimens on Low-E substrates did not.

Through data examination, the 721 cm⁻¹ and 782 cm⁻¹ peaks were identified as being the most distinct peaks for discriminating between glioblastoma multiforme, metastatic and normal brain tissue spectra. A ratio score plot of these peaks determined classification sensitivities and specificities as 100% and 94.44% for glioblastoma multiforme, 96.55% and 100% for metastatic brain, and 85.71% and 100% for normal brain tissue respectively. Cancerous tissue was observed to retain more wax than normal tissue. This difference in dewaxing efficiency was attributed to alterations in tissue density between the histological types. Principle component-discriminant function

analysis revealed separation between metastatic sites: breast, lung, melanoma, colon/rectum and oesophagus and stomach, showing the potential of Raman spectroscopy to identify primary sites of origin from metastatic brain tissue.

Overall, this study demonstrated the diagnostic ability of Raman spectroscopy and the importance of substrate influence on tissue preparation and the quality of spectra.

Acknowledgements

Firstly, I would like to thank my Director of Studies, Dr Matthew Baker, for his consistent support, patience and contribution to this research. His training and direction has been invaluable over the last year in assisting my academic development and understanding. I am grateful to Mr David Griffiths for his time, help and guidance in all histological related matters and Dr Konrad Dorling for his invaluable Matlab training.

During this research I was able to spend three months at the Focas Institute (DIT) in Dublin. I would like to thank Professor Hugh Byrne, Dr Franck Bonnier and Dr Luke O'Neill for their constant kindness and assistance in this project, and for being so welcoming and generous in allowing me to use their resources and intelligence.

I am also very grateful to Reece Hall for his SEM/EDAX expertise, without which I would still be in the lab trying to figure out the instrumentation.

I would like to acknowledge the Sydney Driscoll Neuroscience Foundation, Brain Tumour Northwest, the Association of British Spectroscopists and ERASMUS and thank them for their funding and provisions which facilitated this project.

Lastly, I would like to thank my Mother, Father and four sisters for their love and tolerance over the years, without their support and encouragement I would be lost.

List of Contents

	Page number
List of Figures	1
List of Tables	3
List of Abbreviations	4
Chapter 1 Introduction	5
1.1 Metastatic brain cancer	5
1.1.1 Introduction and Epidemiology	5
1.1.2 Carcinogenesis	6
1.2 The diagnostic modalities of metastatic brain cancer	10
1.2.1 Associated symptoms of brain cancer	10
1.2.2 Preoperative diagnosis	10
1.2.3 Biomarkers	11
1.2.4 Histopathological diagnosis	12
1.3 Raman Spectroscopy	13
1.3.1 Fundamentals of Raman spectroscopy	13
1.3.2 Application of Raman spectroscopy in cancer diagnostics	16
1.3.3 Raman spectra of cancerous tissue	19
1.3.4 Raman Spectroscopy Substrates	20
1.4 Dewaxing of Paraffin embedded tissue samples	21
1.5 Scanning Electron Microscope/Energy dispersive analysis of x-rays	24

1.6 Study aims and rationale	25
1.6.1 Working hypothesis and rationale	25
1.6.2 Main aim of study	25
1.6.3 Secondary aims of study	26
Chapter 2 Materials and Methods	27
2.1 Summary of materials used in the study	27
2.2 Study participants	27
2.3 Tissue preparation for histological examination	29
2.4 Tissue section preparation for Raman spectroscopic analysis	30
2.5 Raman spectroscopy instrumentation and analysis	30
2.6 Data pre-processing and multivariate analysis	33
2.7 SEM-EDAX	36
2.8 Atomic force microscope (AFM)	36
2.9 Statistical Analysis	
Chapter 3 Results and Discussion	37
3.1 Microscopic examinations of H&E stained sections	37
3.2 Substrate Study	38
3.3 Immersion vs. Non-Immersion Raman spectroscopy	51
3.4 532 nm vs. 785 nm laser line	55
3.5 Spectral Histopathology: Discrimination of metastatic tumours	57
Chapter 4 Conclusions	82
Chapter 5 Future Work	85
Bibliography	87
Appendices	93

List of Figures

Figure Number	Title	Page Number
Figure 1	The basic process of carcinogenesis. Adapted from [1].	7
Figure 2	Schematic diagram showing the process of metastasis. Replicated from [2].	9
Figure 3	Energy level diagram for Rayleigh and Raman scattering. Adapted from [3].	14
Figure 4	Diatomic and polyatomic modes of vibration adapted from [4].	16
Figure 5	Molecular structure of paraffin replicated from [5].	23
Figure 6	Horiba Jobin-Yvon LabRAM HR800 Raman spectrometer.	31
Figure 7	The Horiba Jobin-Yvon LabRAM HR800 confocal Raman Spectrometer used to take paraffin wax measurements.	33
Figure 8	Microscopic images of H&E stained tissue samples of normal brain, metastatic brain (from oesophagus and stomach, breast, colon/rectum, lung and melanoma as labelled above) and GBM brain WHO grade IV (x 100).	37
Figure 9	Original spectral plot showing raw spectra of the substrate backgrounds: low-E (top), Spectrosil (middle) and CaF ₂ (bottom).	39
Figure 10	SEM-EDAX of Low-E substrate acquired from three different areas.	41
Figure 11	SEM-EDAX of Spectrosil substrate acquired from three different areas.	42
Figure 12	SEM-EDAX of CaF ₂ substrate acquired from three different areas.	43
Figure 13	Original spectral plot showing the average of 458 CaF ₂ acquisitions, 210 low-E acquisitions and 465 Spectrosil acquisitions from all tissue specimens and a raw spectrum of paraffin wax. The tissue spectra have been vector normalised and offset for visual clarity. The asterisks above the peaks correspond to the paraffin contributions.	45
Figure 14	Original spectral plot showing vector normalised, background-subtracted spectra of substrates after dewaxing from: 1 CaF ₂ acquisition, 1 Spectrosil acquisition and 10 averaged low-E acquisitions. The raw spectrum of paraffin wax (bottom cyan spectra) is included as a reference. The spectra have been appropriately scaled and offset for visual clarity.	47
Figure 15	Photographs showing microscopic Raman images at x 10 of the substrate surfaces after dewaxing. Wax residuals can be observed on the CaF ₂ and Spectrosil substrates.	48
Figure 16	Photographs showing AFM images of Spectrosil, CaF ₂ and Low-E substrates.	50
Figure 17	Original spectral plot showing averaged raw spectra of 1116 immersion acquisitions using, a x 50 objective, and 458 non-immersion acquisitions using a x 60 objective from all tissue specimens on CaF ₂ .	53

Figure 18	Photograph showing Raman (x 50) and immersion Raman (x60) image of brain tissue.	55
Figure 19	Original spectral plot showing averaged raw immersion Raman spectra of 996 acquisitions using the 532 nm laser line and 1116 acquisitions using the 785 nm laser line from all tissue specimens.	56
Figure 20	Original spectral plot showing averaged immersion spectra of 127 GBM acquisitions, 668 metastatic acquisitions and 157 normal brain acquisitions. Spectra have been vector normalised, the backgrounds have been corrected using a 5th order polynomial fit and subtraction and 7 points of smoothing. The asterisks correspond to paraffin peaks from residual wax in the tissue.	59
Figure 21	Chemical structures of the molecules contributing to spectra differences between GBM, normal and metastatic brain tissue.	62
Figure 22	Original discriminant function plot showing the separation between GBM (1), metastatic (2) and normal (3) brain tissue, at spectral level, based on the training set (red) and test set (blue) with 95% (outer ellipse) and 90% (inner ellipse) confidence limits.	64
Figure 23	PC-DFA loadings plot of discriminant functions 1 and 2 from the GBM vs. metastatic vs. normal (Figure 9) PC-DFA model.	66
Figure 24	2D score plot of the 620 cm^{-1} to 782 cm^{-1} peak ration versus the 721 cm^{-1} to 620 cm^{-1} peak ratio. Each data point is the patient average from spectra that have been vector normalised and 5 th order polynomial subtracted.	69
Figure 25	Score plot of intensity measurements from the 1061 cm^{-1} peak and the 1131 cm^{-1} peak of patient averaged normal, GBM and metastatic spectra.	71
Figure 26	Bar chart of three paraffin peak intensities with standard deviation from 127 GBM acquisitions (n=5 patients), 668 metastatic acquisitions (n=29 patients) and 157 normal brain acquisitions (n=7 patients) on CaF_2 substrates.	72
Figure 27	Original spectral plot of averaged immersion spectra: 141 breast met acquisitions, 138 colon/rectum met acquisitions, 127 GBM acquisitions, 194 lung met acquisitions, 102 melanoma met acquisitions, 157 normal brain acquisitions and 93 oesophagus and stomach met acquisitions. Spectra have been vector normalised and offset for visual clarity. The asterisks represent the paraffin contributed peaks.	74
Figure 28	Discriminant function plot displaying the separation of breast met (1), colon/rectum met (2), lung met (3) melanoma met (4) and oesophagus & stomach met (5) based on the train set (red) and test set (blue) with a 95% confidence limit represented by ellipse.	76
Figure 29	Discriminant function plot displaying the separation of primary breast (1), primary colon/rectum (2), primary melanoma (3) and primary oesophagus & stomach (4) cancers based on the train set (red) and test set (blue) with 99% (outer ellipse) and 95% (inner ellipse) confidence limits.	78
Figure 30	Original spectral plot of averaged 95 primary breast acquisitions and 96 breast met acquisitions (top left), 22 primary colon acquisitions and 22 metastatic colon/rectum acquisitions (top right), 22 primary oesophagus & stomach acquisitions and 22 oesophagus & stomach met acquisitions (bottom left) and 25 primary melanoma acquisitions and 20 melanoma met acquisitions (bottom right). The spectra have been vector normalised, baseline corrected by 5 th order polynomial fit and subtraction, and 7 points of smoothing	81

List of Tables

Table Number	Title	Page Number
Table 1	Established biomarkers and the corresponding cancer they relate to. Adapted from [1].	11
Table 2	Summary of tissues, reagents, instrumentation and materials used in the study	27
Table 3	Patient details with histological subtype and metastatic origin.	28
Table 4	Data showing tentative biomolecular assignments of main spectral peaks.	60
Table 5	Data showing PC-DFA model details, including spectral numbers and the resulting sensitivities and specificities.	65
Table 6	Data showing Raman shifts of the main peaks from the PC-DFA loadings.	67

List of Abbreviations

AFM	Atomic force microscope
ASS	Anti-Stokes Scatter
AU	Arbitrary units
BMUP	Brain metastases of unknown primary
BTNW	Brain tumour north west
CCD	Charged coupled device
CNS	Central nervous system
cnt	Counts
CT	Computed tomography
DFA	Discriminant function analysis
DNA	Deoxyribonucleic acid
DOB	Date of birth
EDAX	Energy dispersive analysis of x-rays
EM	Electromagnetic
F	Female
FFPP	Formalin fixed paraffin preserved
FN	False negative
FP	False positive
GBM	Glioblastoma Multiforme
gr	grating
H&E	Haematoxylin and Eosin
IR	Infrared
Low-E	low-emissivity
M	Male
Mets	Metastases
MRI	Magnetic resonance imaging
PCA	Principle component analysis
PET	Positron emission tomography
SEM	Scanning electron microscope
SL	Scattered light
SS	Stokes scatter
TN	True negative
TP	True positive
WHO	World health organisation

Chapter 1

Introduction

1.1 Metastatic brain cancer

1.1.1 Introduction and epidemiology

More than one in three people in the UK will develop cancer at some point during their lifetime and 50% of these individuals will die from the disease within 5 years of diagnosis. Cancer is responsible for one in four deaths and in 2010 it was estimated that one person died from the disease every 4 minutes [1].

Metastatic brain tumours are intracranial neoplasms that originate from cancers located outside the central nervous system (CNS), but have spread there via haematogenous routes or invasion from surrounding tissue. Less than 1 in 100,000 people below 25 years old are reported to have brain metastases, this occurrence increases to approximately 30 individuals per 100,000 above the age of 60 [2]. Currently, no significant association has been observed between gender and tumour incidence [2]. It is estimated that 20–40% of cancer patients develop brain metastases, making them the most common form of intracranial neoplasm in adults [3]. Approximately, 13,000 people in the UK are diagnosed with tumours of the brain every year, of which, 60% are reported to be metastatic tumours [4].

Any malignant tumour has the potential to metastasise to the brain; however, the location of the primary tumour is highly dependent on its probability of doing so. Lung cancer is the most common primary cancer to metastasise comprising 50% of all brain

metastases, breast cancer constitutes 15–25%, and melanoma cancer is responsible for 5–20% of all metastases, the remaining 5–30% occur as a result of other primary cancers. Renal and colon cancers are also known to commonly metastasise to the CNS. The primary cancer site is frequently known before the diagnosis of a metastatic brain tumour. However, nearly 30% of metastases are detected either before or at the time of primary diagnosis [5] and approximately 15% of primary tumour locations remain unknown. Identification of the primary tumour significantly increases the efficiency of the cancer treatment, and thus patient survival [6].

Over 80% of brain metastases are located in the cerebral hemispheres, due to its mass and blood supply [7], roughly 10–15% are situated in the cerebellum and 1–3% are found in the brainstem [8]. About 50% of metastatic brain tumours exist as the only metastasis in the brain but very rarely do they exist as the only metastasis in the body [2]. Breast, colon and renal cancers typically produce only a single metastasis, whereas lung and melanoma cancers are often responsible for multiple metastases. Although, MRI studies suggest that the number of patients with single metastases is lower than previously thought. The number of brain metastases present is important due to the influence it has over the selected treatment; and thus all existent metastases should be identified [9].

1.1.2 Carcinogenesis

Carcinogenesis is a multistage process whereby cells progress into cancerous cells, and is typically divided into three stages: initiation, promotion and progression [10]. Figure 1 diagrammatically shows the basic process of carcinogenesis. Initiation occurs when exposure to a chemical carcinogen, radiation or other insults results in an

interaction with an organism, causing a change to its molecular deoxyribonucleic acid (DNA) structure; hence, mutations arise during DNA synthesis. It causes an irreversible increase in the susceptibility of a cell to develop cancer, but does not necessarily alter its morphology. Promotion occurs when clonal expansion of the initiated cell, due to genetic alteration, results in the formation of a benign tumour. In the progression stage, the benign tumour becomes malignant, invades local tissue and has the potential to metastasise. At this point, genetic instability increases and karyotype alterations occur [10-12].

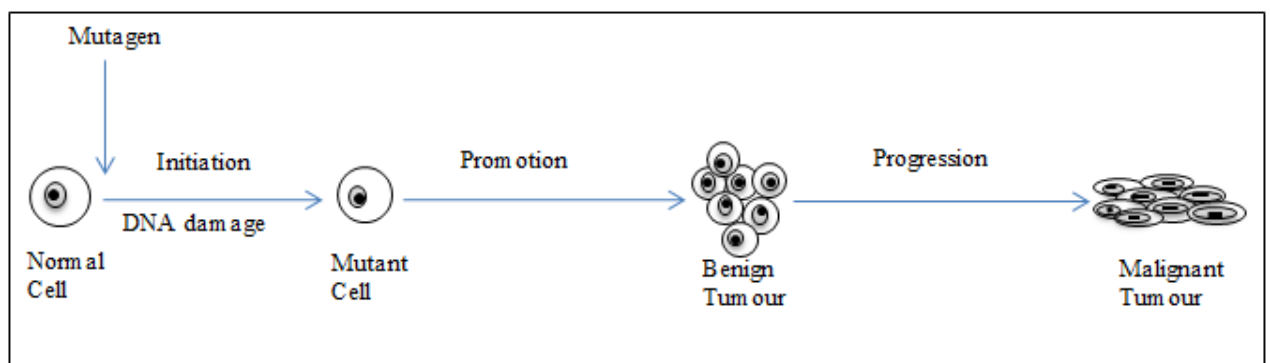


Figure 1: The basic process of carcinogenesis. (Adapted from [13]).

A stable equilibrium between cell proliferation, growth arrest and differentiation, and apoptosis is successfully controlled in normal tissue. Alterations to the homeostatic mechanisms that control this stability can result in tumour formation. The disparity between cell proliferation and apoptosis causes an increase in tissue mass. [11]. Cell proliferation is the production of cells, through replication, needed for normal growth and development. The majority of normal human cells have the ability to divide once or twice a day, thus replication must be controlled to prevent over-proliferation. Differentiation is when cells become specialised and is directly related to a cells ability to proliferate. The differentiation of a cell is tightly regulated in normal tissue.

Apoptosis refers to cell death and is essential for homeostatic maintenance in normal tissue. In neoplastic tissue, the following cellular functions are usually incorrectly regulated: cell proliferation is not controlled effectively, cell differentiation is distorted, chromosomal and genetic organisation is weakened and apoptosis is inefficiently monitored [14].

Cells that are neoplastic exhibit cytological differences including: increased nuclear material, increased nuclear-to-cytoplasmic ratio, increased nuclear staining, abnormal nuclear shape and size, abnormal chromatin distribution, decreased differentiation and increased mitotic activity [15]. The conformations and quantities of nucleic acids, proteins, lipids and carbohydrates are also altered when a normal cell becomes neoplastic. These morphological and biochemical changes vary between the type and location of the cancer [16].

Benign tumours are rarely fatal, but can cause health problems depending on their anatomical location. Malignant tumours, on the other hand, progress and usually result in mortalities if the tumour goes unnoticed or treatment is not successful. Malignant tumours are typically differentiated from benign tumours by histopathological observation of invasion and identification of tumour metastasis within the tissue [17].

A metastasis occurs when cancer cells detach themselves from the malignant tumour and travel to other sites where they form deposits [18]. Within 24 hours of tumour cells entering the blood stream only about 0.1% is still viable, and of those, only 0.01% will go on to produce metastases; consequently, only a minority of primary malignancies result in the formation of metastases at other locations [19]. The process

of metastasis from the primary cancer to a secondary organ is displayed in Figure 2. Tumour cells are genetically less stable than normal cells [20] and are highly heterogeneous. Cells with a high metastatic potential have been reported to have a higher rate of mutation than those with a low metastatic potential and thus may genetically differ from their primary cells [19]. Conversely, comparative genomic hybridisation has produced data showing a high level of conformity between brain metastases and their corresponding primary cancers at a chromosomal level [21].

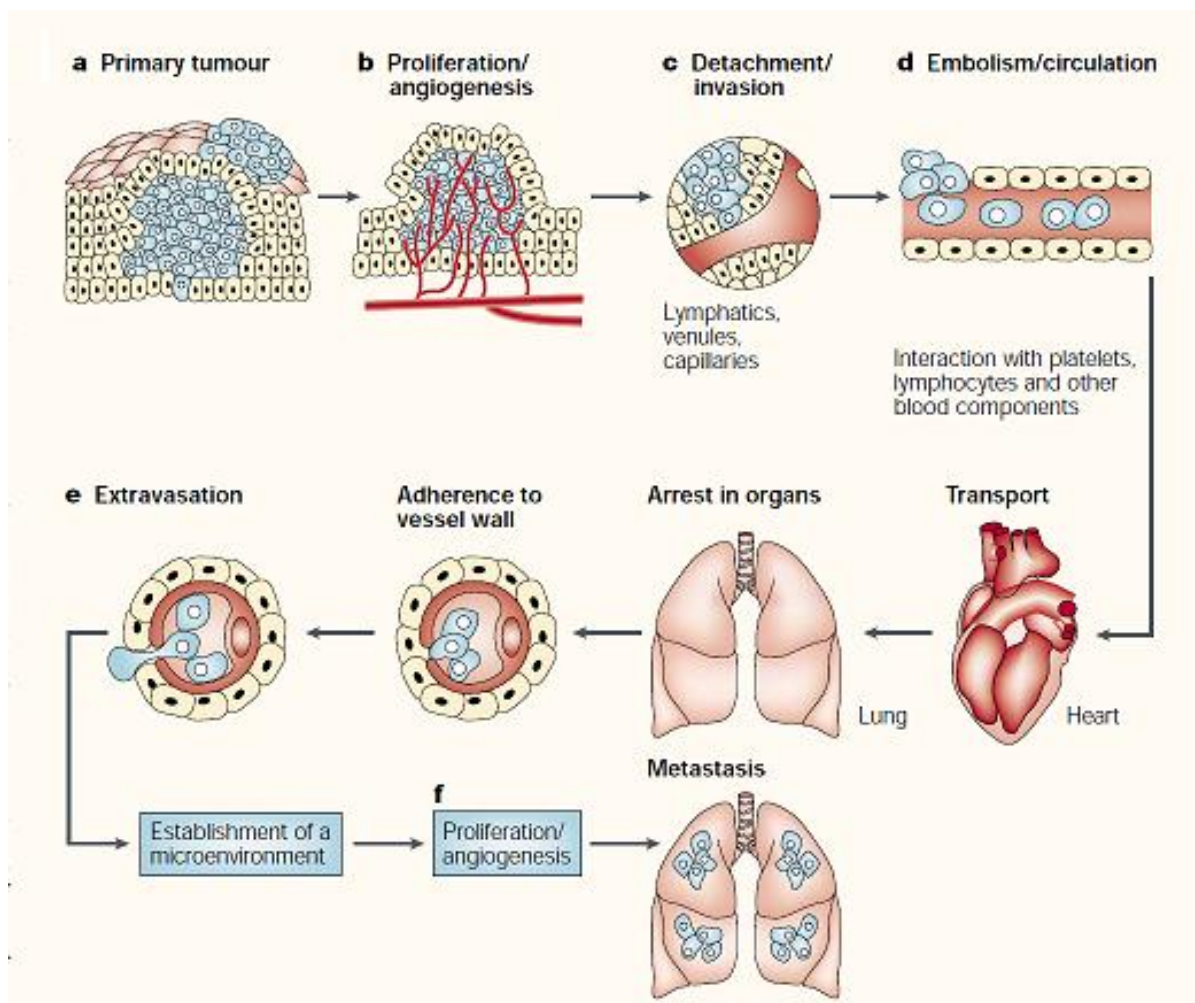


Figure 2: Schematic diagram showing the process of metastasis. Replicated from [19].

1.2 The diagnostic modalities of metastatic brain cancer

1.2.1 Associated symptoms of brain cancer

The symptoms associated with brain tumours can be produced as a result of an increase in intracranial pressure caused by the tumour mass and have a significant impact on a patient's quality of life. Approximately, 66% of people with brain metastases exhibit neurological symptoms at the time of diagnosis, including: headaches, seizures, altered vision, neurocognitive dysfunction and strokes, however, the other 33% do not [8]. The prognosis of patients is poor and individuals are expected to live only a few months after diagnosis of the brain metastasis [22]. The accurate and rapid diagnosis of disease allows early intervention of the correct treatment. This leads to an increase in life expectancy and quality of life for the patient, which in turn relieves economic resources within healthcare [23]. Currently, diagnosis of a brain tumour is carried out by a series of various components, comprising of: medical history, physical, neurological and laboratory examinations [24].

1.2.2 Preoperative diagnosis

At present, neurological examinations consist of brain scans, such as magnetic resonance imaging (MRI), computed tomography (CT) and positron emission tomography (PET), to initially detect and assess the suspected brain tumour [25]. These imaging techniques allow non-invasive, in vivo monitoring of the brain enabling analysis of the existent mass, its tumour margins and its location [24]. These examinations are only used as a preliminary assessment due to the risk of misdiagnosis when using the aforementioned methods alone for identification of tumours. False

positive (FP) diagnoses of either metastatic or primary cancers occur in 11% of patients with brain lesions when based only on the MRI scan. Further examinations must be conducted to allow a more accurate diagnosis [26].

1.2.3 Biomarkers

Biomarkers are used in population screening studies, disease diagnosis, prognosis and monitoring. Biomarkers have been identified through techniques such as immunological assays [27]; Table 1 shows a selection of the biomarkers that are currently used for cancer detection. Biomarkers have the potential to be very beneficial for population screening and early disease detection. However, they are not universally accepted as their specificities and sensitivities are not high enough and false positives occur too frequently. It is thought that the most single powerful biomolecules have already been identified and thus sensitivities and specificities can only improve by the identification and analysis of multiple biomarkers to enable cancer diagnosis [27].

Table 1: Established biomarkers and the corresponding cancer they relate to. (Adapted from [27]).

Biomarker	Cancer
α -Fetoprotein (AFP)	Hepatoma; testicular cancer
Carcinoembryonic antigen (CEA)	Colon; breast; lung; pancreatic
PSA	Prostate cancer
CA125	Ovarian cancer
CA15.3	Breast cancer
CA19.9	Gastrointestinal
Immunoglobulins	B cell discrasias
Chroriogonadotropin (hCG)	Testicular cancer
Steroid hormone receptors	Breast cancer

1.2.4 Histopathological diagnosis

The current method of choice for diagnosing metastatic brain tumours and their primary sites is histopathological analysis of stained tissue sections. Staining is carried out in order to visualise cellular components. Haematoxylin and Eosin (H&E) staining is the most common and well established method for staining tissue sections for examination of cancers. Haematoxylin dyes the nuclear component of cells blue and eosin dyes the cytoplasm and connective tissue pink [28]. Neoplasms are identified histologically by increased cellular crowding and disorder in the tissue [16]. Analysis consists of assessment of the morphology, architecture and staining of the tissue. However, this method of diagnosis requires a trained neuropathologist, is invasive and has a lengthy processing time, delaying treatment. Histopathological examination is also a highly subjective method of diagnosis [29, 30] and it has been reported that pathological diagnostic discrepancy can occur in 1-43% of specimen [31, 32]. False negatives (FN) may occur as a result of the biopsy procedure failing to locate and remove the abnormal lesion leading to only normal tissue being analysed. Treatments are then chosen based only on the histopathological diagnosis which could potentially be life threatening [33].

Adenocarcinoma is the most frequent type of primary cancer for brain metastases of unknown primary (BMUP). Tumours can be poorly differentiated in adenocarcinomas and the resulting brain metastases. The microscopic appearance of adenocarcinoma metastases from different primary locations is similar, and consequently impairs histopathological examination and hence diagnosis. The development of diagnostic techniques that can accurately identify the primary cancer

origin from analysis of the metastatic brain tissue alone is needed to allow early intervention and correct treatment in order to increase patient survival time [34].

1.3 Raman Spectroscopy

1.3.1 Fundamentals of Raman spectroscopy

Raman spectroscopy is based on the interaction of electromagnetic radiation, in the form of monochromatic light, with matter. Light is scattered either elastically or inelastically as it hits the sample. The majority of light is elastically scattered, known as Rayleigh scattering, and does not involve an exchange in energy between the incident light and the molecules within a sample. Rayleigh lines are thus scattered at the same frequency as that of the incident light. Inelastically scattered light, known as Raman scattering, involves an energy exchange between the incident light and the molecules within a sample in accordance with quantal laws [35]. Raman scatter is less intense than Rayleigh scatter and generally comprises no more than 0.001% of the total scattered light [36]. The energy change (ΔE) must be equal to the difference in energy between two allowed states of the molecule, thus, representing a change in the molecules rotational or vibrational energy. When a molecule gains energy photons will be scattered with $h\nu - \Delta E$ and the light will have a frequency of $\nu - \Delta E/h$. Conversely, if a molecule loses energy, photons will be scattered with $h\nu + \Delta E$ and the light will be scattered with a frequency of $\nu + \Delta E/h$. Where $h\nu$ is the photon energy, ν is the radiation frequency and h is Planck's constant [35]. Scattered light (SL) with a lower frequency to that of the incident light is called Stokes scattering (SS). This is where energy is transferred from the incident light to the molecule; the excited molecule does not return

to its ground state from the virtual state, but to its vibrational state, and a lower energy photon is emitted. Scattered light of a higher frequency to that of the incident light is called Anti-Stokes scattering (ASS). This is where the molecule is already at its vibrational state, due to prior excitement or thermal disturbance, and the molecule is excited to a virtual state. Energy is transferred to the incident light from the molecule, returning it to its ground state, and a photon of higher energy is emitted [37, 38]. Figure 3 displays a basic diagram of energy levels for Rayleigh and Raman: Stokes and Anti-Stokes scatter.

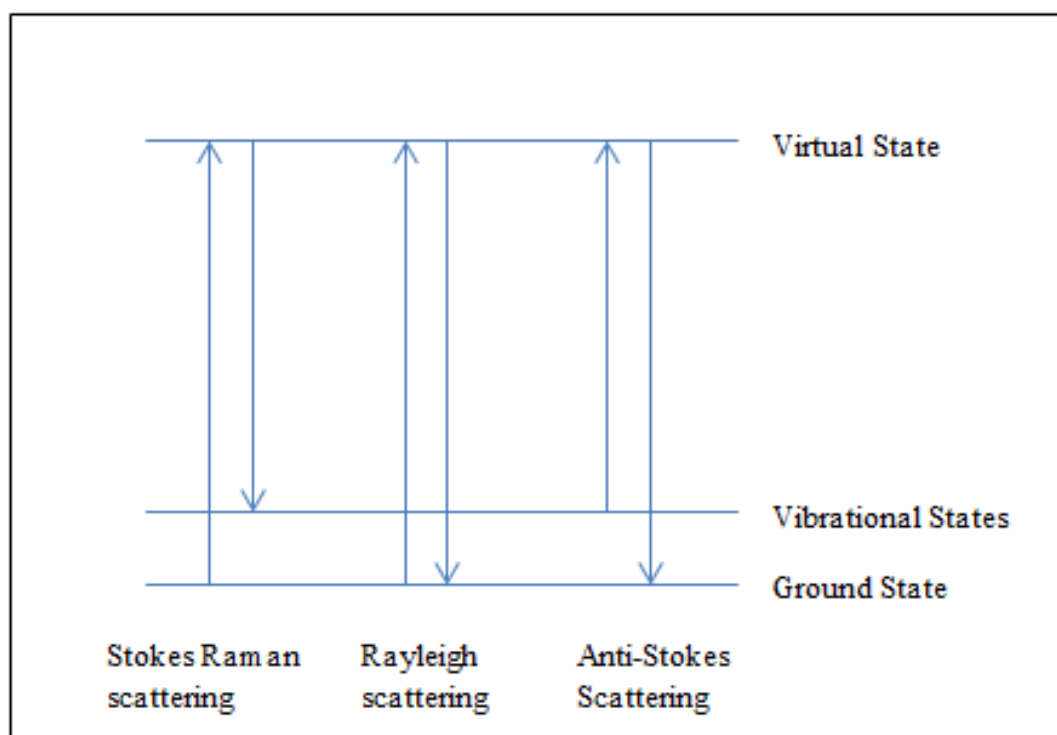


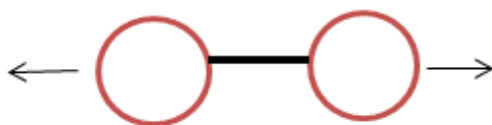
Figure 3: Energy level diagram for Rayleigh and Raman scattering. (Adapted from [39]).

If a molecule is exposed to a static electric field it becomes distorted as the positively charged nuclei are attracted toward the negative pole and the negatively charged electrons are attracted toward the positive pole. The charge centre separates and an induced dipole moment occurs as a result, the molecule is polarised. A change in the

polarisability, reflected in the magnitude or direction of the polarisability ellipsoid, must be caused by molecular rotations and vibrations for its modes to be Raman active. The number of normal vibrational modes a molecule has can be calculated by the degrees of freedom: either $3N-5$ for linear molecules, such as CO_2 , or $3N-6$ for non-linear molecules, such as H_2O ; where N represents the number of atoms in the molecule. The vibrational modes of a molecule can include symmetric stretching, asymmetric stretching and bending, but not all vibrational modes will be Raman active (Figure 4) [35].

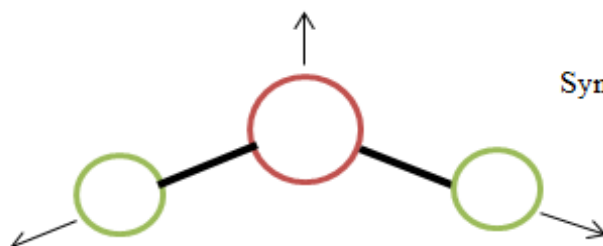
Diatomic Molecules

Stretch

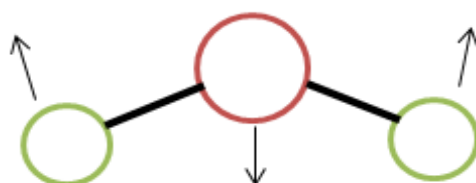


Polyatomic Molecules

Symmetric stretch



Bend



Asymmetric stretch

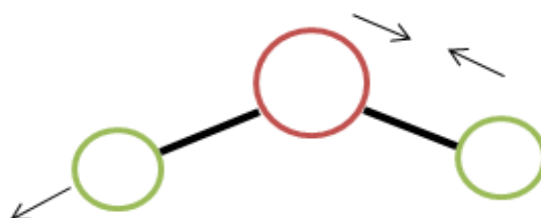


Figure 4: Diatomic and polyatomic modes of vibration (adapted from [35]).

1.3.2 Application of Raman spectroscopy in cancer diagnostics

Raman spectroscopy measures the energy shift and intensities of scattered photons [40]. It is both a quantitative and qualitative technique which is able to provide molecular information about samples from their spectra, regarding conformation and

composition [41, 42]. The frequencies and intensities of Raman bands are based on the atoms involved, the conformations and the chemical environments of the bonds, and their concentrations within a molecule; and are thus unique to specific molecules, enabling the production of characteristic spectra and the identification of molecules within a sample [43].

Raman spectroscopy is a non-destructive technique which is able to analyse samples in any state, without extensive solvent use or sample preparation. It is a rapid and economical method of analysis. Moreover, it is a relatively low-risk and easy technique to use [44]. Measurement of a single cell can be achieved with Raman spectroscopy due to its good spatial resolution [45]. It is a non-ionising technique and water presence does not significantly alter spectra produced, as it is a weak light scatterer. With the use of fibre optic probes, Raman spectroscopy can be used for *in vivo* measurements, giving it an advantage over other vibrational techniques, such as infrared spectroscopy, which is highly affected by H₂O absorption bands in spectra [46] [47]. With the use of deep Raman spectroscopic techniques, measurements can be made up to several millimetres into tissue samples [48].

Tumours that are not completely resected during surgery to remove all neoplastic and pre-neoplastic cells have a greater chance of reoccurrence [49]. Within five years after simple surgical excision of the tumour, cancer recurrence is reported to occur in 10.1% of basal cell carcinoma cases [50]. There cannot be an application of safety margins for the excision of brain tumours, as there is in extracerebral cancers, due to the brain's high level of functional responsibility. Thus, accurate identification of tumour margins is essential for an optimistic prognosis [51]. The advantage of *in vivo* analysis that Raman spectroscopy offers allows real-time analysis of tissue. This can aid

tumour margin identification during surgery, help direct biopsies to enable complete removal of cancerous tissue [52], whilst preserving the surrounding healthy tissue [53].

When analysing biological tissue at short wavelengths, below 500 nm, Raman spectroscopy can suffer from intense spectral backgrounds, thought to be as a result of fluorescence, which can significantly affect the quality of the spectra. The use of near infrared (NIR) lasers, such as 785 nm, to irradiate the sample reduces this phenomenon; as wavelengths in this region do not typically induce the electronic transitions in tissue chromophores that contribute to fluorescence. Dispersive Raman spectrometers enable the use of 785 nm lasers and help to reduce the spectral background that can result when analysing biological materials. Charged coupled device detectors are employed in dispersive instruments and have assisted the development of portable Raman spectrometers [54].

Immersion Raman spectroscopy utilises an immersion lens which is in direct contact with an appropriate liquid, such as deionised water, which covers the sample under analysis. Bonnier *et al.* [55] describe and demonstrate the successful use of immersion Raman spectroscopy for both live cell and *in vitro* tissue specimens on CaF₂ substrate, and observe the improvement of spectral quality, sample stability and the reduction of spectral background [55, 56]. They determined that fluorescence, contributing to spectral background, is only significant at short wavelength laser sources, as proteins typically only fluoresce with wavelengths below 500 nm. Hence, the background of spectra acquired using 785 nm lasers should not be attributed to fluorescence but to sample morphology, associated with scattering of the incident light and Raman lines that cause non-collimated entry into the spectrometer. The exchange of a tissue/air interface with a tissue/liquid interface results in more uniform refractive

indices thus, reducing this level of stray light, and in turn, the intensity of the spectral background. Submerging the sample in liquid also protects tissue specimens from photo-damage. In turn this enabling more powerful lasers of shorter wavelengths to be used and longer acquisition times and a higher number of accumulations to be employed, hence, improving spectral quality [55-57].

The potential of Raman spectroscopy as a diagnostic tool for diseases has been demonstrated by a variety of studies [33, 58-69]. Many papers have shown the ability of Raman spectroscopy to diagnose cancers, including: brain cancers using tissue on low-E microscope slides and CaF₂ slides [58, 59], lung tumours through the analysis of bronchial tissue sections [60], gastric adenocarcinomas using tissue samples [61, 62], non-melanoma skin cancers from the analysis of tissue *in vivo* [63], laryngeal cancers from tissue at endoscopy [64], breast cancers using both fresh and frozen tissue specimens [65, 66], cervical cancers from tissue *in vivo* [67], bladder and prostate cancers from tissue sections [68, 69] and oesophagus and colon cancers through the analysis of snap frozen tissue on CaF₂ [33].

1.3.3 Raman spectra of cancerous tissue

Significant biochemical differences should be present between neoplastic and healthy tissue that arise as a result of an alteration in biological processes [70]. When a tissue becomes diseased, molecular composition is altered, DNA concentrations in the cell increase and the amounts of other components in the cell vary compared with non-diseased cells [71]. These molecular changes should be expressed in its vibrational spectra, enabling the spectral discrimination between diseased and healthy tissue. As a

result, significant spectral differences can act as markers for the identification of specific diseases [52].

Gajjar *et al.* [58] observed significant ($P \leq 0.0001$) differences between the Raman spectra of brain tumour tissue and healthy brain tissue at the following spectral points: 1483 cm^{-1} (CH_2 bend), 852 cm^{-1} (tyrosine and proline), $\approx 1235\text{ cm}^{-1}$ and 1276 cm^{-1} (Amide III), 1654 cm^{-1} (Amide I) and 997 cm^{-1} (phospholipids and glucose-I-phosphate). They also reported the ability of Raman spectroscopy to successfully discriminate between different brain tumour types. They observed that metastatic brain tissue could be differentiated from healthy brain tissue at the following spectral points: 997 cm^{-1} (phospholipids and glucose-I-phosphate), 1077 cm^{-1} and 1446 cm^{-1} (lipids and proteins), 1241 cm^{-1} (Amide III), $\approx 1460\text{ cm}^{-1}$ (cytosine) and 1654 cm^{-1} (Amide I) [58].

The Raman spectra of biological samples can be largely affected by artefacts. Gaussian noise, as a result of fluorescence of the sample or thermal fluctuations on the charged coupled device (CCD), can result in unwanted intense backgrounds. The result of this effect needs to be reduced prior to data analysis through background correction pre-processing methods. Cosmic spikes can also occur in the spectrum, caused by high energy particles hitting the CCD, but this effect can be eliminated during measurements by accumulating the spectra more than once [72].

1.3.4 Raman Spectroscopy Substrates

Substrates are needed in Raman spectroscopy to support the samples during analysis. Samples are often relatively thin allowing incident light the opportunity of interacting with the substrate below. This interaction has an effect on the spectral

background; thus, the correct choice of substrate for Raman analysis is essential for reducing this background and optimising the quality of the spectral data [57].

Common spectroscopy substrates used currently include quartz, calcium fluoride (CaF_2) and low-emissivity (low-E) microscope slides. Spectrosil, a type of quartz substrate, is approximately 0.5 mm thick, has a perimeter of 7.5 cm x 2.5 cm and costs typically £9.00 per slide. CaF_2 is approximately 1 mm thick, has a perimeter of 2.5 cm x 2.5 cm and costs £35 per slide. MirrIR, a low-E slide, is approximately 2 mm thick, has a perimeter of 7.5 cm x 2.5 cm and costs £1.50 per slide. Low-E substrates are glass slides that are coated with a metallic reflective coating, such as tin oxide/silver, allowing high transmission of visible light [73].

Draux *et al.* [74] investigated the use of different optical substrates for Raman measurements of live cells. The substrates they analysed were CaF_2 , quartz and zinc selenide (ZnSe). They reported that ZnSe is toxic to living cells and hence were unable to take measurement of the live cells using this substrate. They found that both the CaF_2 and quartz produced Raman spectra with comparable signal-to-noise ratios and that neither substrate interfered with the obtained results. Although, they concluded that due to quartz having no effect on cell growth and morphology, it is the best substrate to use for Raman spectroscopic measurement of live cells [74].

1.4 Dewaxing of Paraffin embedded tissue samples

Raman spectroscopy can analyse tissue samples in a variety of different conditions. These most commonly consist of tissues that have been formalin fixed paraffin preserved (FFPP), frozen, and fresh tissue. Using tissue in an unaltered state is

desirable for Raman analysis, but fresh tissue is not easily accessible and is difficult to section [75]. Frozen and FFPP tissues are frequently used as alternatives to fresh tissue due to better accessibility. FFPP tissue is often chosen over frozen tissue due to its long preservation time, easy obtainability and storage and the ability to use it for carrying out retrospective studies [76].

In order to prevent degradation, by halting biochemical processes, biological tissues must be fixed. The most frequently used fixative solution is formalin which uses bonding reactions to work on tissue proteins [77]. Huang *et al.* [78] investigated the impact of fixation on tissues; they observe formalin fixation artefacts at $980\text{ cm}^{-1} - 1100\text{ cm}^{-1}$ and $1480\text{ cm}^{-1} - 1650\text{ cm}^{-1}$; yet, they report that the major Raman peaks for proteins and lipids are not altered by formalin fixation. However, they conclude that with a large focus being on *in vivo* applications, fresh tissue is always preferable for analysis in order to generate results that would be more similar to those experienced in clinical settings [78].

Tissue is often impregnated with a medium for preservation and to add support to aid sectioning through microtomy. The most common and efficient medium for embedding tissue sections is paraffin wax. The sections are dehydrated, washed in an organic solvent, saturated with molten paraffin wax and are then left to cool to enable the wax to solidify. FFPP tissue has to be dewaxed prior to spectroscopic analysis to reduce the spectral contribution of the paraffin wax and allow the tissue to be as similar to an *in vivo* state as possible for analysis [79]. Ó Faoláin *et al.* [79] observed that paraffin wax contributes to Raman spectra at wavenumbers; 1063 cm^{-1} , 1133 cm^{-1} , 1296 cm^{-1} and 1441 cm^{-1} corresponding to C-C, CH₂ and CH₃ bonds as a result of its straight hydrocarbon chain structure. They also reported a less intense peak at 1004 cm^{-1}

corresponding to the C-C bonds of an aromatic ring, due to a small number of cycloparaffins [79]. The structure of paraffin is displayed in Figure 5. Xylene is frequently the method of choice for dewaxing FFPP tissue sections due to its efficacy and rapidity in doing so. However, associated problems such as its high toxicity and flammability can lead to the use of histoclear as it is a suitable alternative. Histoclear is not toxic or flammable and is biodegradable [79]. Ó Faoláin *et al.* [79] evaluated the efficacy of these two common dewaxing solvents and also looked into the potential use of hexane for dewaxing tissue. They observed that hexane is better at dewaxing FFPP tissue than both xylene and histoclear; however, requires 18 hours of tissue submersion in the solvent and is currently not an accepted solvent for dewaxing tissue sections [79].

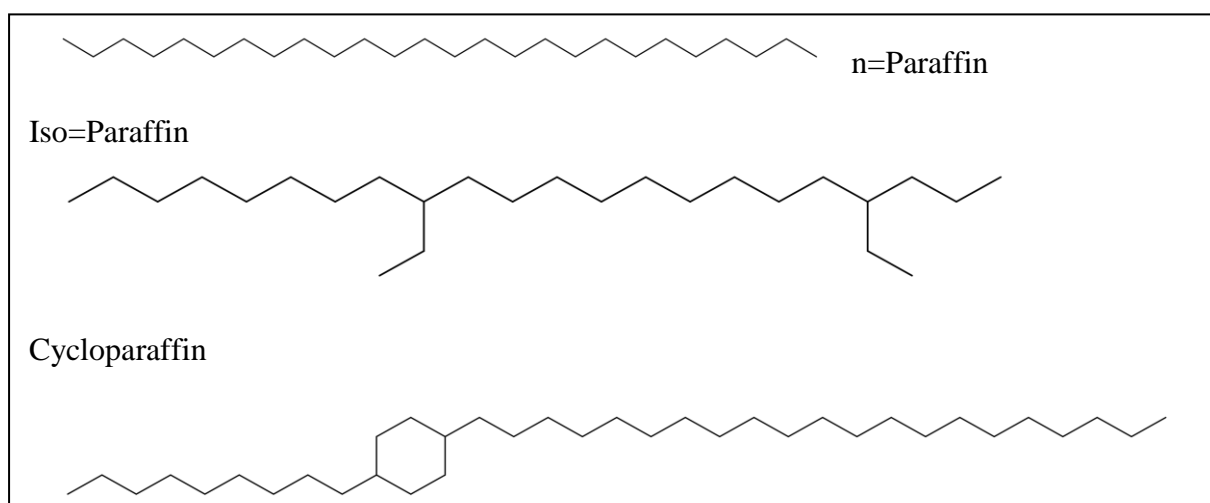


Figure 5: Molecular structure of paraffin (Replicated from [79]).

Chemical dewaxing is not 100% efficient and can also alter samples. Digital dewaxing methods have been developed, utilising the application of independent component analysis, to identify and subtract paraffin peaks in the spectra [80].

1.5 Scanning Electron Microscope/Energy dispersive analysis of X-rays

Scanning electron microscopy (SEM) combined with energy dispersive analysis of X-rays (EDAX) is used to observe and analyse specimens microscopically, and tentatively identify and quantify the elements present in samples. SEM is based on the detection of secondary electrons and it takes place under vacuum to enable an optimum mean free path, so the electrons are not scattered. An electron gun emits high energy electrons which are focused into a small-diameter electron probe by magnetic lenses and serially scanned across the specimen surface by scanning coils. When the primary electron beam hits the surface of the specimen, secondary electrons are knocked loose from its surface. These electrons are detected and then amplified to produce an image of the specimen, created using the count of secondary electrons at each scanned point along the surface. Instrumental resolution is typically between 1 nm -10 nm [81, 82].

Samples are often placed on aluminium stubs for analysis and held there using carbon tape which enables good electrical contact between the sample and the aluminium stub. Samples are illuminated with a high energy beam of electrons; thus, SEM analysis requires samples to be good electrical conductors. A sputter coater is used prior to SEM analysis which coats samples with gold to ensure they conduct electricity [83].

EDAX uses X-rays, which are generated as a result of the interaction between a high-energy electron beam and a solid, to produce a chemical spectrum of the analysed material. Essentially, all elements with atomic numbers 4 to 92 can be detected. It is both a qualitative and quantitative technique for the analysis of elemental components within materials. For qualitative analysis, detection of the specific x-ray wavelengths is

required. Quantitative analysis requires measurement of the intensities of the wavelengths for each element, which are compared with the intensities produced from known calibration standards [84].

1.6 Study aims and rationale

1.6.1 Working hypothesis and rationale

The working hypothesis of this study is that Raman spectroscopy will be able to discriminate metastatic brain tumours from normal brain and GBM tissue based on Raman spectra.

Current detection methods for metastatic brain cancer have a long diagnostic window, require highly trained personnel and are subjective. Raman spectroscopy can provide non-subjective, minimally invasive, non-destructive, rapid and economical diagnosis and would thus be an ideal method for diagnosing metastatic brain cancer [85].

1.6.2 Main aim of study

The primary aim of this study was to assess the diagnostic potential of Raman and immersion Raman spectroscopy for metastatic brain cancer. This was done by analysing metastatic, normal and GBM brain tissue, to identify if any spectral differences can be observed.

1.6.3 Secondary aims of study

A further aim of this study was to investigate the ability of Raman spectroscopy to identify the primary cancer site of origin of brain metastases. This was conducted by analysing metastatic brain tissue from various primary cancers of: lung, breast, oesophagus and stomach, colon/rectum and melanoma, and identifying if any spectral differences are present that can demarcate the groups and thus enable identification of the primary cancer.

The study also involved an investigation into the effect of spectroscopic substrates on tissue preparation methods and the outcome of spectra. This was carried out by comparing the background and tissue spectra produced from Raman spectroscopy of three common substrates: CaF₂, Spectrosil quartz and Low-E, to analyse the quality of both the spectra and the dewaxing procedure.

A comparison between Raman and immersion Raman spectroscopy, using a 785 nm laser, was carried out to ascertain which method yields better quality spectra for spectral histopathology. This involved an examination of the tissue spectra produced by both methods.

Raman spectroscopy can be carried out using a variety of wavelengths for the incident laser. This study evaluated the differences in the resulting spectra of tissue samples produced from Raman spectroscopy using a 532 nm laser line and a 785 nm laser line. This was carried out in order to assess which wavelength laser produces the better quality spectra for the specimens in this study.

Chapter 2

Materials and Methods

2.1 Summary of materials used in the study

Table 2 displays a summary of all the materials employed to carry out this study.

Table 2: Summary of tissues, reagents, instrumentation and materials used in the study

Tissue	Reagents	Instrumentation	Materials
Normal brain	Ethanol	Raman spectrometer	Spectrosil substrate
Metastatic brain	Haematoxylin	microtome	CaF2 substrate
Colon/rectum	Eosin	Desiccator	Low-E substrate
Oesophagus/stomach	Deionised water	SEM-EDAX	
Breast		Atomic force microscope	
Skin		Optical microscope	

2.2 Study participants

Tissue samples were obtained from formalin fixed paraffin preserved (FFPP) tissue blocks from the Brain Tumour North West (BTNW) bio-bank under ethical approval (BTNW/WRTB 13_01). Patient data consisted of histological information, patient gender and date of birth, origin of metastasis/histological subtype. A total of 48 tissue specimens were obtained from 41 different patients. Tissue consisted of normal brain samples (n=7), glioblastoma multiforme (GBM) brain samples WHO (world health organisation) grade IV (n=5), metastatic brain samples (n=29) and primary cancer tissue samples (n=7). The normal tissue all had a normal microscopic appearance with no detectable tumour present, coming from patients with meningiomas, aneurisms, chondrosarcomas, oedematous changes or no disease. Table 3 displays further information about the tissue specimens. Sections were cut, by microtomy, at both 4 μ m

onto glass microscope slides and 10 µm onto spectroscopic substrates: low-E MirrIR slides (Kevley Technologies, Chesterland, OH, 44026, USA), Spectrosil quartz (Starna Scientific) and calcium fluoride (CaF₂) (Crystran).

Table 3: Patient details with histological subtype and metastatic origin.

BTNW no.	Gender	DOB	Origin of metastasis/histological subtype
119	F	26/06/1963	Breast (met and primary site)
707	F	07/08/1945	Breast (met and primary site)
756	F	15/03/1957	Breast (met and primary site)
888	M	25/11/1948	Colon/rectum (met and primary site)
985	M	05/02/1933	Melanoma (met and primary site)
988	M	30/12/1949	Oesophagus & stomach (met and primary site)
1001	F	20/12/1944	Lung (met only)
690	F	25/10/1960	Breast (met and primary site)
1004	F	03/09/1956	Breast (met only)
998	M	25/07/1946	Colon (met only)
1020	F	05/06/1948	Breast (met only)
2	F	28/10/1937	GBM
3	F	22/09/1981	GBM
4	M	08/12/1942	GBM
5	F	29/10/1958	GBM
7	M	14/04/1939	Normal Brain
10	F	13/06/1929	GBM
78	F	24/09/1955	Lung (met only)
106	F	14/02/1965	Normal Brain
132	F	24/06/1943	Normal Brain
136	F	25/09/1956	Normal Brain

137	M	26/04/1944	Colon/rectum (met only)
164	M	10/04/1954	Oesophagus & stomach (met only)
184	F	21/11/1948	Lung (met only)
215	M	21/01/1973	Lung (met only)
274	M	12/07/1940	Colon/rectum (met only)
295	F	12/06/1936	Lung (met only)
358	M	08/05/1935	Melanoma (met only)
409	F	08/08/1925	Colon/rectum (met only)
444	M	30/01/1978	Normal Brain
509	M	11/02/1930	Melanoma (met only)
517	F	05/06/1955	Lung (met only)
521	M	18/01/1949	Oesophagus & stomach (met only)
562	F	12/03/1953	Lung (met only)
567	F	09/04/1947	Melanoma (met only)
668	F	30/08/1943	Colon/rectum (met only)
678	F	13/11/1961	Normal Brain
688	F	15/06/1965	Melanoma (met only)
694	M	18/09/1951	Lung (met only)
721	F	04/01/1976	Oesophagus & stomach (met only)
772	M	21/09/1972	Normal Brain

2.3 Tissue preparation for histological examination

Tissue sections on the microscope slides needed to undergo staining with Haematoxylin and Eosin (H&E) for parallel histological examination; to allow microscopic examination the sections cannot be too thick and 4 μm is standard. Using standard procedures, the sections were de-waxed before staining by: 2 x 5 minute baths of histoclear followed by 2 x 5 minute baths of ethanol. The tissue sections were

washed in distilled water for 5 minutes after de-waxing, prior to H&E staining. Sections were bathed in haematoxylin for 5 minutes and then washed in warm tap water to allow the nuclei to turn blue. The sections were then covered in eosin for 4 minutes and rinsed with distilled water. Finally, the tissue sections were dehydrated in 2 x 5 minute baths of ethanol and cleared in 2 x 5 minute baths of histoclear, and then protected and preserved through the application of histomount and a coverslip. The sections were then microscopically examined in order to identify the metastatic sites present in the tissue.

2.4 Tissue section preparation for Raman spectroscopic analysis

The tissue sections on Raman substrates must be thick enough for spectral analysis, to avoid large amounts of substrate contribution to the spectra, and needed to be de-waxed prior to Raman analysis in order to reduce paraffin peaks in the spectra. The de-waxing procedure, consistent with standard procedures [58], was carried out by an initial 3 x 5 minute baths of histoclear followed by 3 x 5 minute baths of ethanol. The sections were left to air dry for 30 minutes, placed in a Petri dish and stored in a desiccator until spectroscopic analysis.

2.5 Raman spectroscopy instrumentation and analysis

Spectroscopic measurements were carried out using a Horiba Jobin-Yvon LabRAM HR800 spectrometer (Figure 6). An air cooled CLDS point mode diode 785 nm laser with a single edge filter (cut off to 100 cm^{-1}) and an output power of 300 mW was used to acquire spectra. A narrow bandwidth, solid state diode 532 nm laser with single edge filter (120 cm^{-1}) and an output power of 50 mW was also used for spectral

acquisition. The aforementioned lasers were used with gratings of 300 gr/mm and 600 gr/mm respectively and blazed at 1000 nm for the near-infrared region and 500 nm respectively. Non-immersion point spectra were acquired using a 0.9 (x 100) (MPlanN) objective, with a 1 μm spot size, non-immersion spectral maps were collected using a 0.75 (x 50) (MPlanN, Olympus) objective and immersion point spectra and maps were taken using a 1 (x 60) objective (LUMPlanFLN, Olympus), with a 1.5 μm spot size. The confocal hole was set at 100 μm for the 785 nm spectral collections and 200 μm for the 532 nm spectral collections. The detectors used were an Andor electromagnetic (EM) CCD and a Synapse CCD, with 1024 x 256 pixels and cooled at $-70\text{ }^{\circ}\text{C}$, for the laser line 785 nm and 532 nm respectively. The spectra were measured across the wavelength range of 400 cm^{-1} – 1800 cm^{-1} .



Figure 6: Horiba Jobin-Yvon LabRAM HR800 Raman spectrometer.

The instrumentation was calibrated before operation to silicon at the spectral line at 520.8 cm^{-1} . Spectra collected using a 100% exposure 785 nm laser were acquired for 30 seconds and accumulated twice, with both the immersion and non-immersion objectives. Spectra collected using the 532 nm laser were 100% exposed with an acquisition time of 4 seconds and accumulated twice. Three to five areas were used to produce at least 20 spectra per tissue sample, targeting the nucleus of cells. A total of 3054 spectra were generated through the production of at least 20 spectra from three to five areas on each tissue samples, depending on size, to enable the production of results that are good representations of each sample. Immersion Raman spectroscopy consisted of tissue submersion in deionised water which was then placed in direct contact with the immersion objective lens.

Spectroscopic measurements of the paraffin wax were carried out on a Horiba Jobin-Yvon LabRAM HR800 confocal Raman Spectrometer (Figure 7). The detector used with this system was an air-cooled open electrode 1024 x 256 pixel CCD detector. A x 50/0.55 long working distance microscope objective (PL FLUOTAR, Leica) was employed for the measurements. Spectral acquisition was carried out for 30 seconds and accumulated twice using a 785 nm laser as the incident source with a filter set to 100%. The 785 nm laser line has an output power of 400 mW and has a power at the sample of 100 mW.

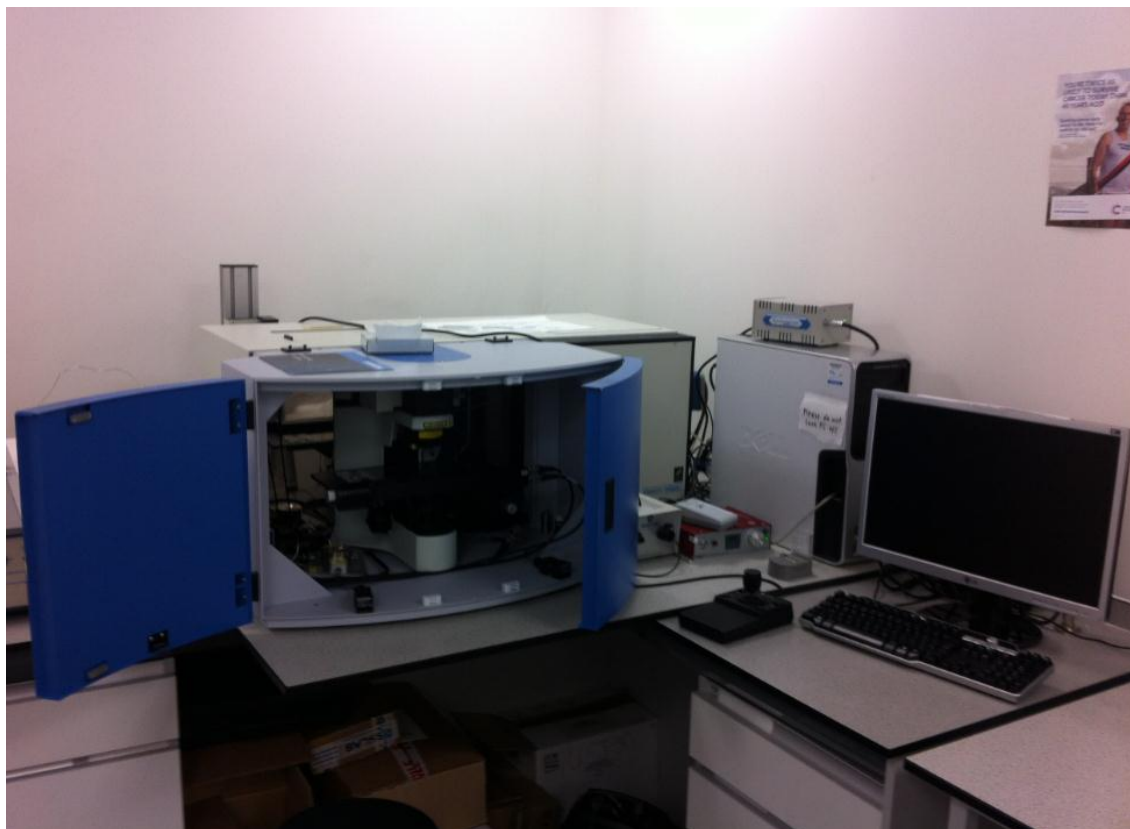


Figure 7: The Horiba Jobin-Yvon LabRAM HR800 confocal Raman Spectrometer used to take paraffin wax measurements.

2.6 Data pre-processing and multivariate analysis

Pre-processing and multivariate analysis were carried out on the raw data using LabSpec 6 spectroscopy software suite (HORIBA Scientific) and MATLAB version 7.11.0 (R2010b) (The MathWorks, Inc., USA) using in-house written software.

Pre-processing of the data was kept minimal to allow a better level of reproducibility. Initially, all the data were subjected to a visual quality test to ensure only adequate spectra were included in the analysis. Vector normalisation was applied to all the raw data in MATLAB using codes written by Dr A. Henderson. Biological

samples are heterogeneous and the environmental and instrumental settings are changeable, thus, normalisation is applied to mathematically account for this inconsistency through the identification of non-disease attributed variability between the data prior to adjustment [86]. A fifth order polynomial fit was applied and then subtracted to each of the spectra followed by 7 point smoothing in the LabSpec 6 software. A polynomial fit is a method of baseline correction whereby non-constant, low frequency baselines are adjusted for. Smoothing is a method of local averaging that is applied to the data to produce de-noised spectra [86]. Paraffin peaks were manually removed from the spectra for multivariate analysis at the following wavenumbers: 882 cm^{-1} - 912 cm^{-1} , 1051 cm^{-1} - 1071 cm^{-1} , 1115 cm^{-1} - 1143 cm^{-1} , 1163 cm^{-1} - 1187 cm^{-1} , 1284 cm^{-1} - 1305 cm^{-1} and 1407 cm^{-1} - 1501 cm^{-1} .

Multivariate analysis was then carried out on the spectral set, employing principal component-discriminant function analysis (PC-DFA). Principle component analysis (PCA) is an unsupervised method of identifying patterns in data, and expressing the data in such a way to highlight similarities and differences. PCA can be used to reduce the dimensionality of the dataset prior to DFA. Spectra for PC-DFA were organised into two sets: a training set and a blind test set. DFA is a supervised technique, based on the PCs and the DFA algorithm's prior informed knowledge of group memberships. It maximises the intergroup variance and minimises the intragroup variance. Hence, discrimination between groups is achieved. The PC-DFA model was tested by a blind test set using one third of the total dataset which was randomly selected, supplied to the model and then analysed on a graphical output by identifying what group they were classified as belonging to [87].

Error ellipses were used to highlight 90%, 95% and 99% confidence limits on the PC-DFA graphical output, using `error_ellipse.m` written by A.J. Johnson and obtained from Matlab central file exchange. These were formed by calculated the covariance matrices from the discriminant function score matrix. The mean of each data group defined the centroid of the ellipsoid.

The classification sensitivities and specificities were calculated from the DFA score plot based on the error ellipses. This study investigated three different PC-DFA models. Sensitivity is the percentage of a population with a disease that are classified as positive and specificity is the percentage of a population without a disease that are classified as negative [88] .

$$\text{Sensitivity} = [TP/TP+FN] \times 100$$

$$\text{Specificity} = [TN/TN+FP] \times 100$$

Where:

TP = true positive

- Number of spectra correctly classified as cancerous

FN = false negative

- Number of spectra incorrectly classified as not-cancerous

TN = true negative

- Number of spectra correctly classified as not cancerous

FP = false positive

- Number of spectra incorrectly classified as cancerous

[89]

2.7 SEM-EDAX

The FEI Company Quanta series 200 SEM/EDAX, with an xT microscope system, was used to generate microscopic images and produce information on elemental composition of the three substrates. The substrates were coated in gold prior to SEM/EDAX analysis and situated on a carbon tape for analysis.

2.8 Atomic force microscope (AFM)

The atomic force microscope (AFM) model used to image the samples for surface morphology for this study is the MFP-3D-BIO (Asylum Research), with Olympus silicon AC160 cantilevers. The tips were 160 nm long with resonant frequencies typical of 320 kHz. A/C mode was employed for operation to reduce tip/sample interaction.

2.9 Statistical Analysis

All data were analysed using relevant statistical test. All data were analysed using in-house written software on Matlab. The data was interrogated using PCA and PC-DFA methods. All experiments were performed more than three times to ensure reproducibility of the results.

Chapter 3

Results and Discussion

3.1 Microscopic examinations of H&E stained sections

Figure 8 shows the microscopic images of the H & E stained tissue specimens at x 100 magnification of normal brain, GBM, Oesophagus and stomach metastasis, breast metastasis, colon/rectum metastasis, lung metastasis and melanoma metastasis. It can be observed that normal brain, metastatic brain and GBM brain tissue architecturally differ from one another and between the metastatic types.

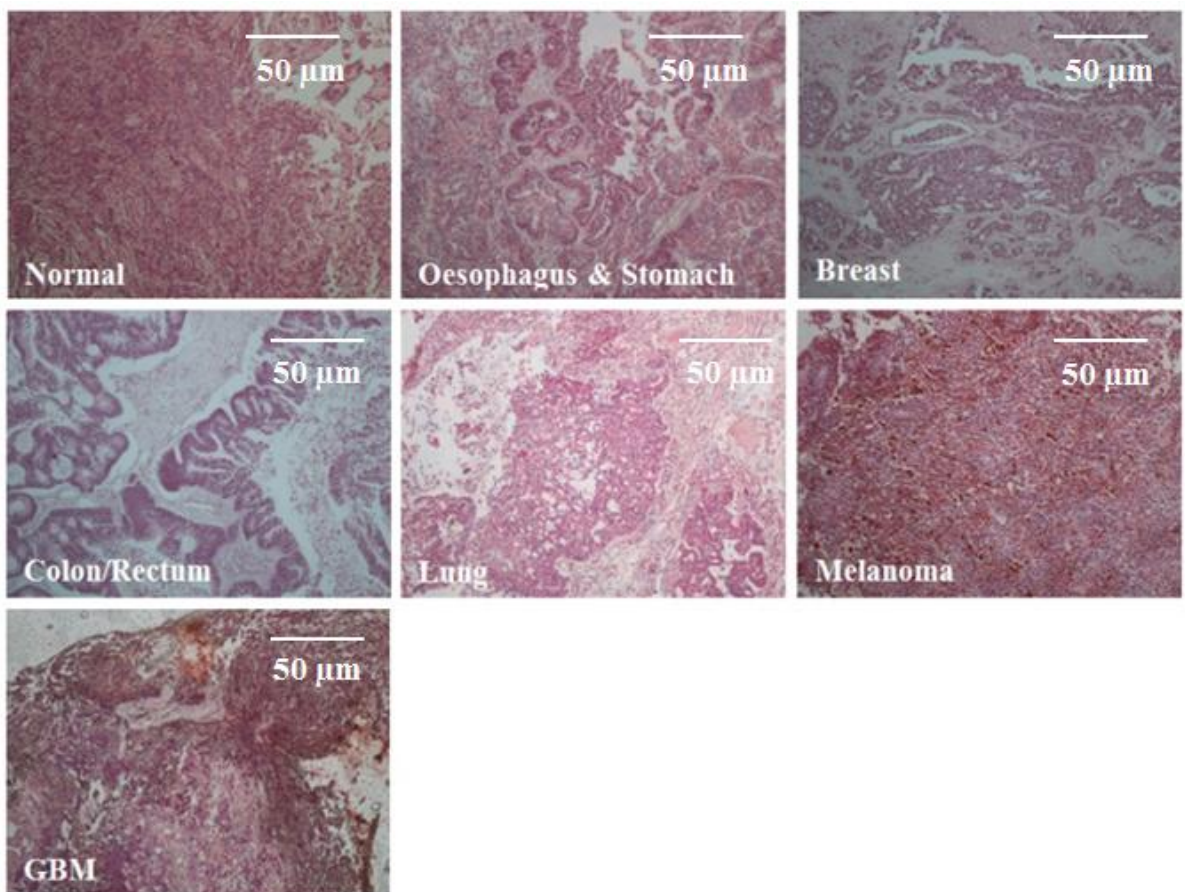


Figure 8: Microscopic images of H&E stained tissue samples of normal brain, metastatic brain (from oesophagus and stomach, breast, colon/rectum, lung and melanoma as labelled above) and GBM brain WHO grade IV (x 100).

3.2 Substrate Study

Raman spectra were acquired of the three substrates: low-E, Spectrosil and CaF_2 using the 785 nm laser under the same conditions, which display the spectral ‘fingerprints’ of the substrates, shown in Figure 9. This is to ascertain the impact of the substrates’ contribution to the spectral background and hence establish their level of interaction with the incident light source and the impact they have on the spectra of tissue samples.

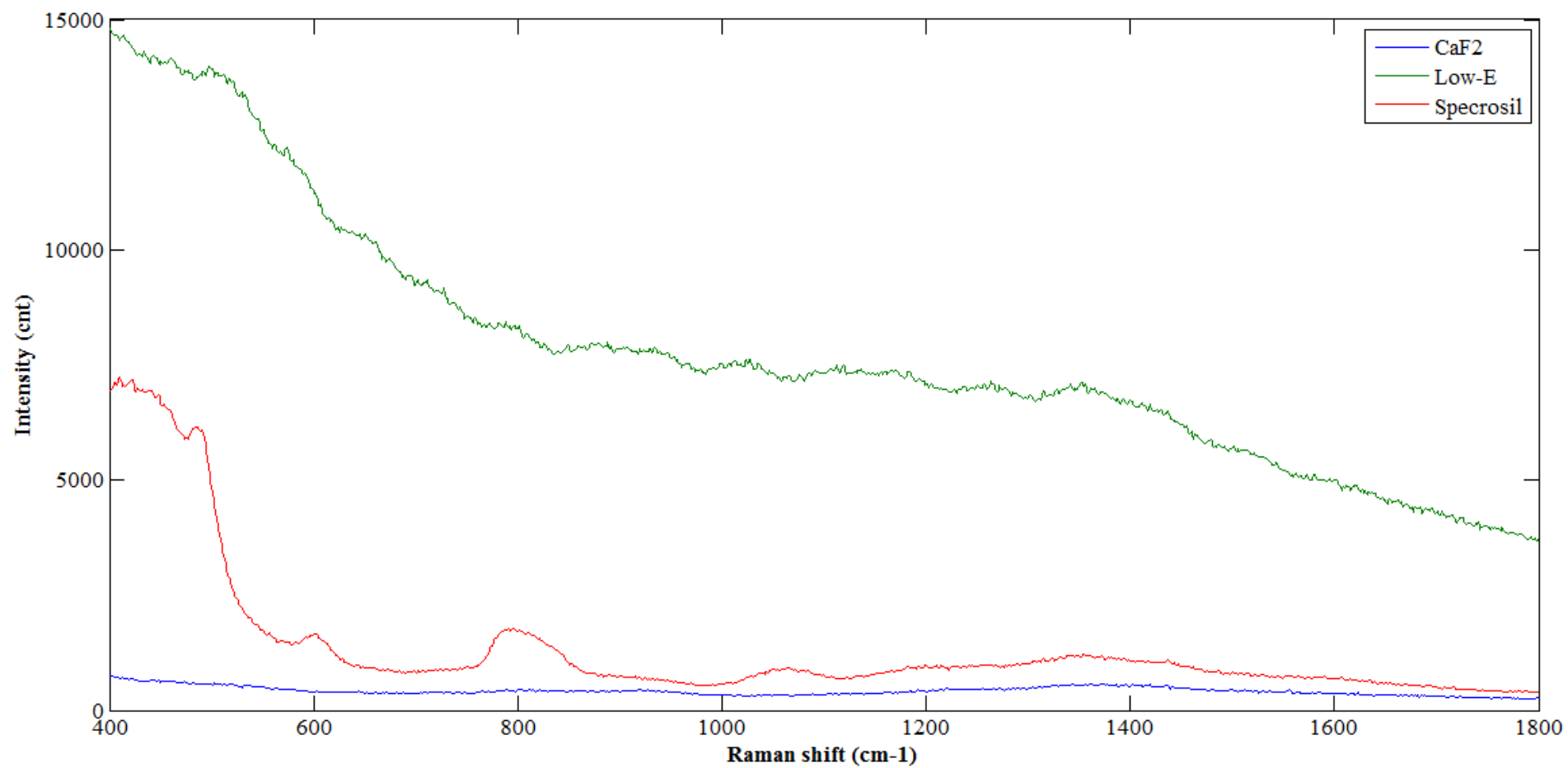


Figure 9: Original spectral plot showing raw spectra of the substrate backgrounds: low-E (top), Spectrosil (middle) and CaF₂ (bottom).

It can be observed that low-E has the highest intensity baseline and CaF_2 has the lowest intensity baseline of the three substrates. The baseline of Spectrosil is slightly higher than that of CaF_2 and has apparent peak contributions at approximately 600 cm^{-1} and 800 cm^{-1} . These results indicate that the spectra taken from samples on CaF_2 are less affected by substrate background and should display spectral information relating only to the sample of interest and low-intensity peaks more clearly than either low-E or Spectrosil substrates.

Each substrate was analysed using the scanning electron microscope and energy dispersive analysis of X-rays (SEM/EDAX) instrument, in order to assess the chemical constituents present and microscopically observe the substrate surface. Figures 10-12 show the results of the analysis and the associated microscopic images of these substrates. The Spectrosil substrate exhibits peaks of silicon and oxygen. CaF_2 exhibits peaks of calcium, fluoride and oxygen. Low-E substrates exhibit peaks of silicon, oxygen, cobalt, nickel, magnesium sodium, palladium, silver, cadmium, tin and calcium. The gold peak and carbon peak are not contributed by the specimen, but are present as a result of the gold used to coat the samples and the carbon tape used to situate the sample on.

The higher number of constituents present in the low-E substrate provides more molecules that can interact with the incident laser of Raman spectroscopy. Thus, providing an explanation for the substrate's high spectral baseline when compared with CaF_2 and Spectrosil, which is only composed of two elements and three elements respectively.

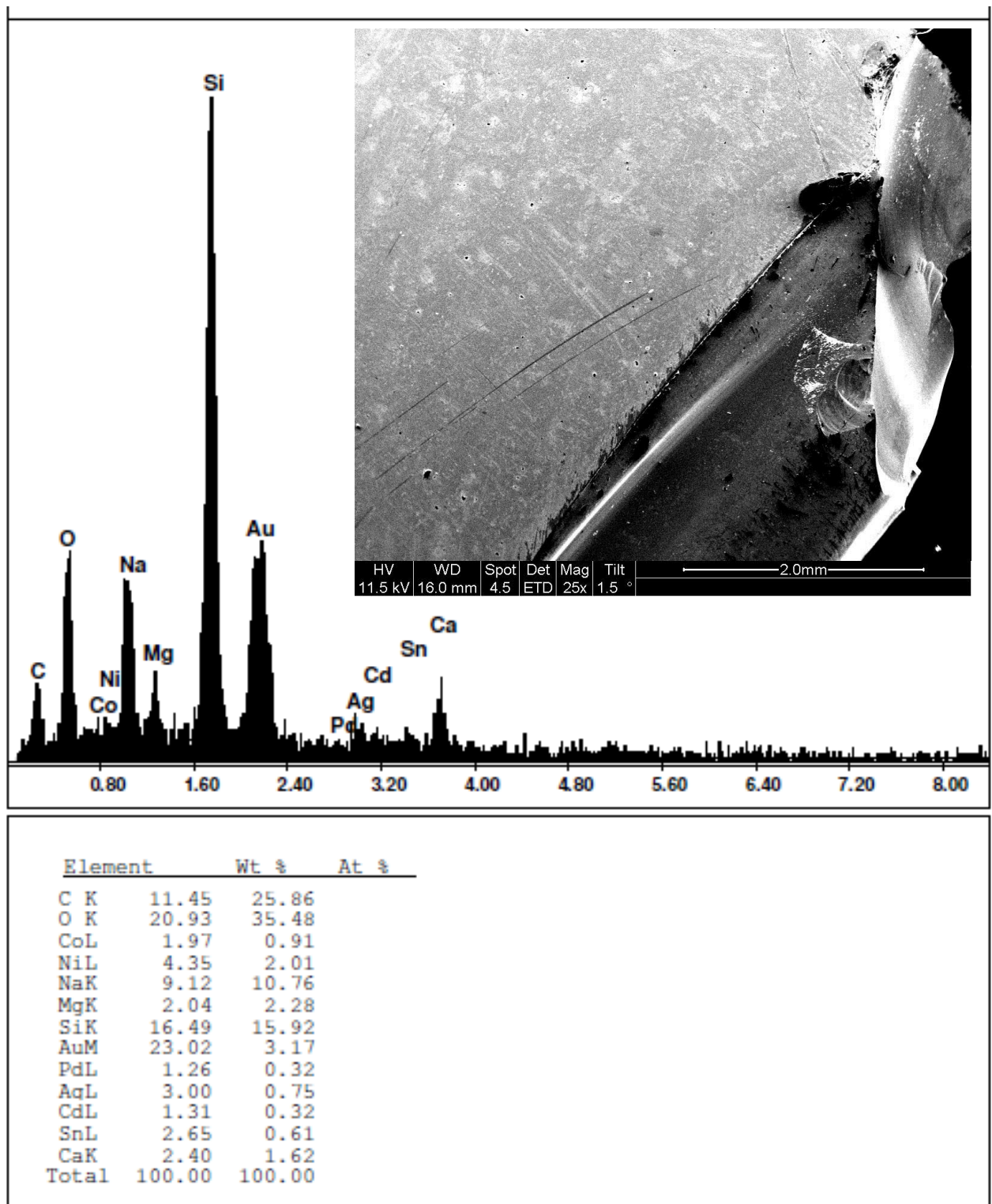


Figure 10: SEM-EDAX of Low-E substrate acquired from three different areas.

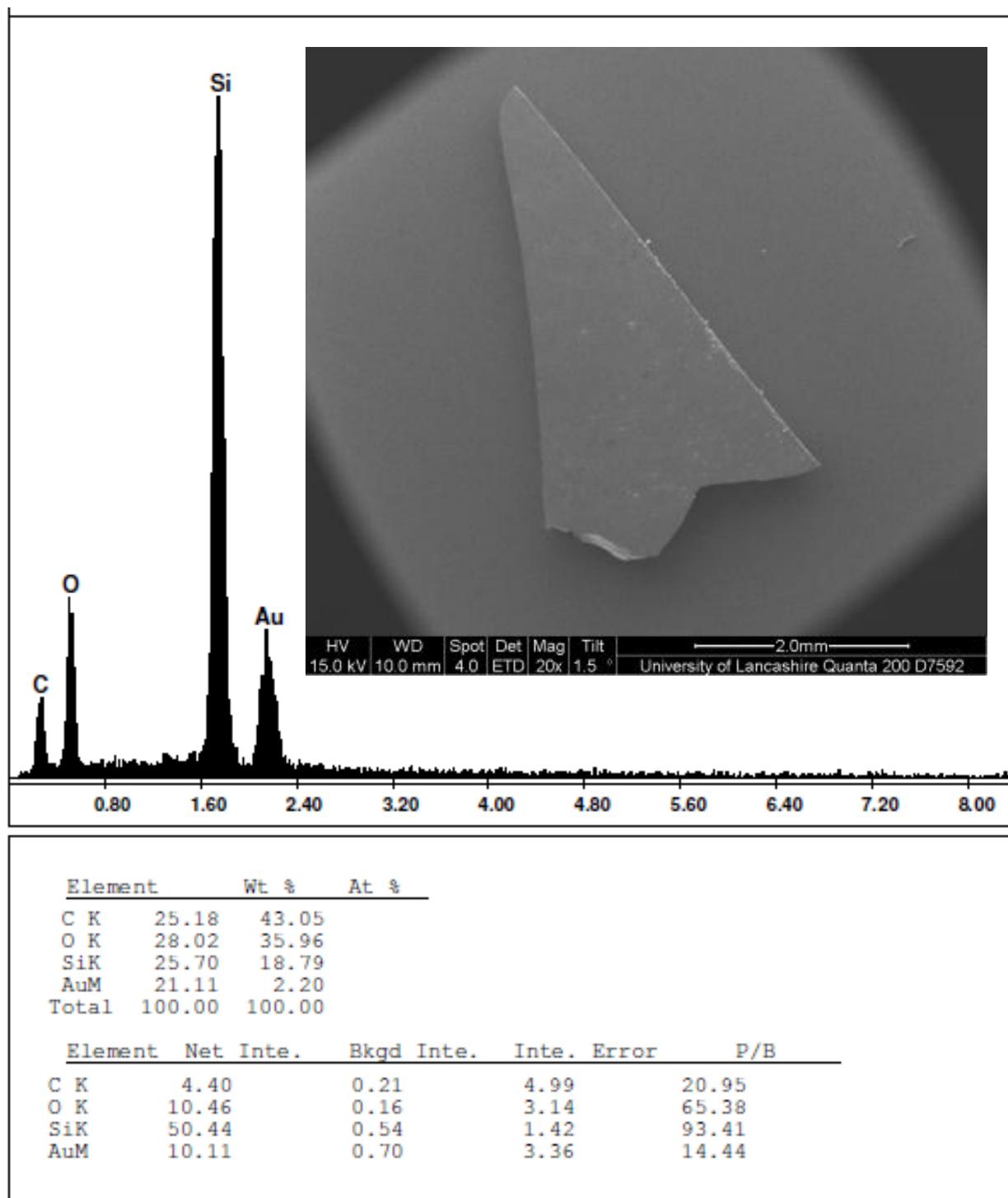


Figure 11 SEM-EDAX of Spectrosil substrate acquired from three different areas.

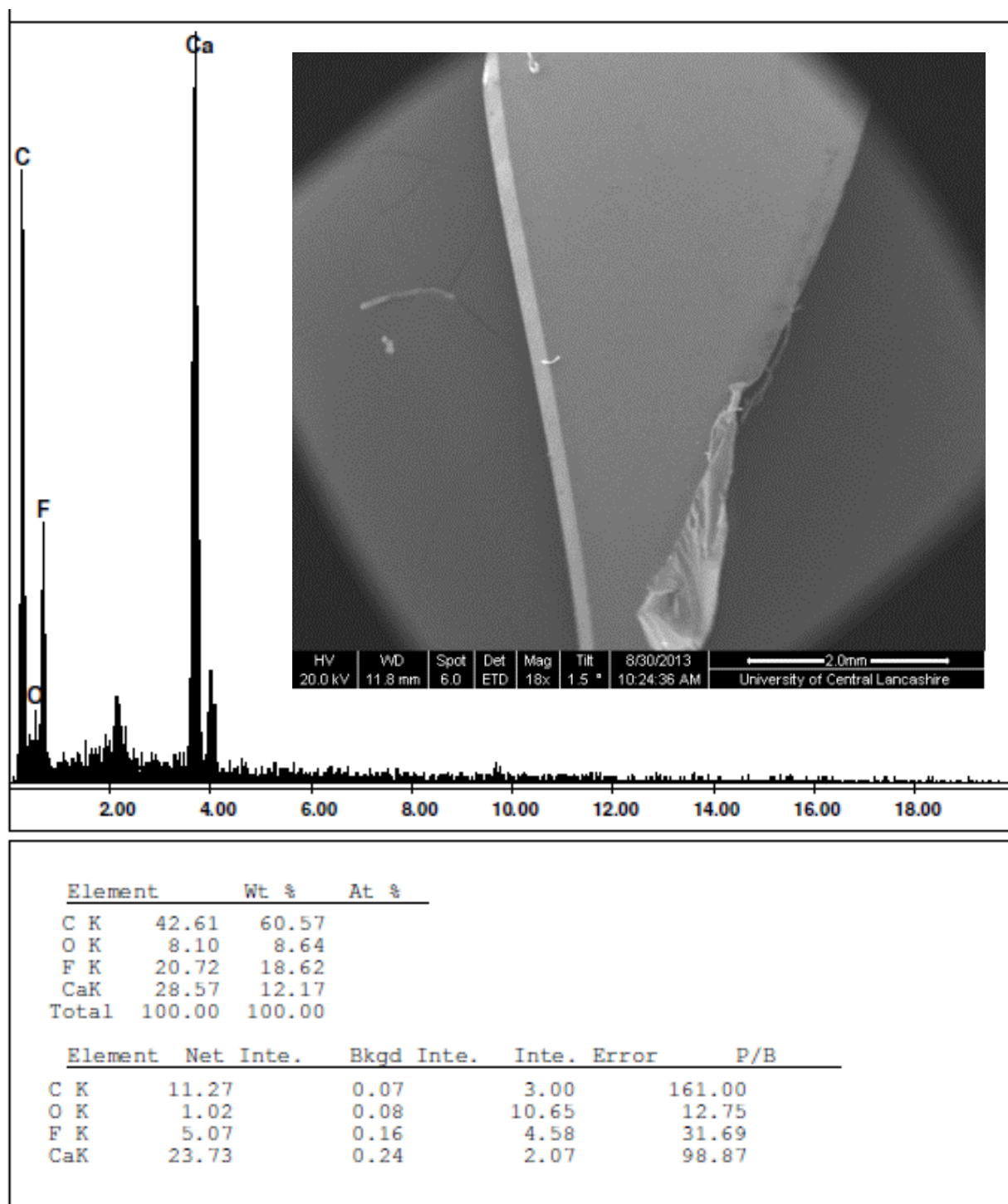


Figure 12 SEM-EDAX of CaF_2 substrate acquired from three different areas.

Spectra were acquired of the tissue samples situated on the three different substrates, under the same conditions using the 785 nm laser, to further ascertain the level of influence substrate type has on the outcome of spectra. It can be observed from the averaged, vector normalised spectra displayed in Figure 13 that the tissue spectra on Low-E has a lower signal-to-noise ratio and the peaks are visually less clear and not as distinguishable as those produced from tissue on either CaF₂ or Spectrosil. The discrepancy between the spectra on different substrates shows that the substrate used has an effect on signal-to-noise ratio, and thus influences the resulting Raman spectra.

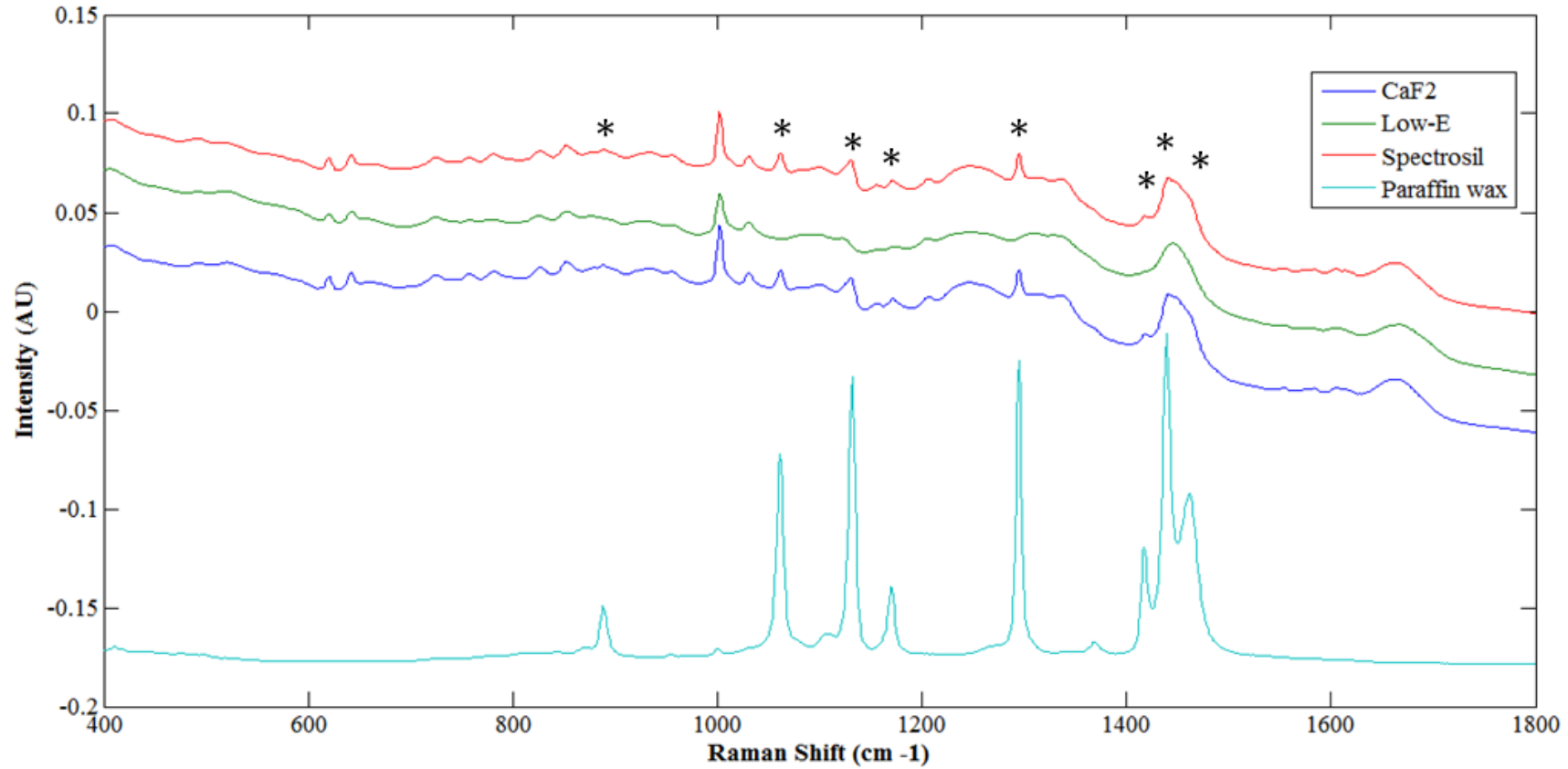


Figure 13: Original spectral plot showing the average of 458 CaF₂ acquisitions (18 specimens from n=11 patients), 210 low-E acquisitions (10 specimens from n=10 patients and 465 Spectrosil (18 specimens from n=11 patients) acquisitions from all pathologies and a raw spectrum of paraffin wax. The tissue spectra have been vector normalised and offset for visual clarity. The asterisks above the peaks correspond to the paraffin contributions.

A paraffin spectrum displays notable spectral peaks at 888 cm^{-1} , 1061 cm^{-1} , 1131 cm^{-1} , 1171 cm^{-1} , 1294 cm^{-1} , 1417 cm^{-1} , 1440 cm^{-1} , 1462 cm^{-1} , which can be assigned to C-C stretching and CH_2 and CH_3 deformations within the molecule [79]. It can be seen from Figure 13 that the spectra of tissue samples on Spectrosil and CaF_2 still exhibit paraffin peaks after the samples have been dewaxed, however, dewaxed tissue spectra from low-E substrates do not display any visible paraffin peaks.

In order to investigate any substrate effect on the dewaxing process, the wax was analysed on each of the substrates without tissue present. Paraffin wax was cut at $10\text{ }\mu\text{m}$ sections, the same thickness as that of the tissue sections, and mounted onto the three different substrates. The wax was then left to melt onto the substrate for 20 minutes in an oven set at $60\text{ }^\circ\text{C}$ and allowed to cool. The paraffin only samples were then dewaxed by the same method as the FFPP tissue samples and analysed; Figure 14 displays the resulting vector normalised and background subtracted spectra. Spectrosil and CaF_2 substrates continue to exhibit large paraffin peaks in their spectra, which correspond to the peaks displayed in the spectra of paraffin, whilst the low-E substrate exhibits no such peaks.

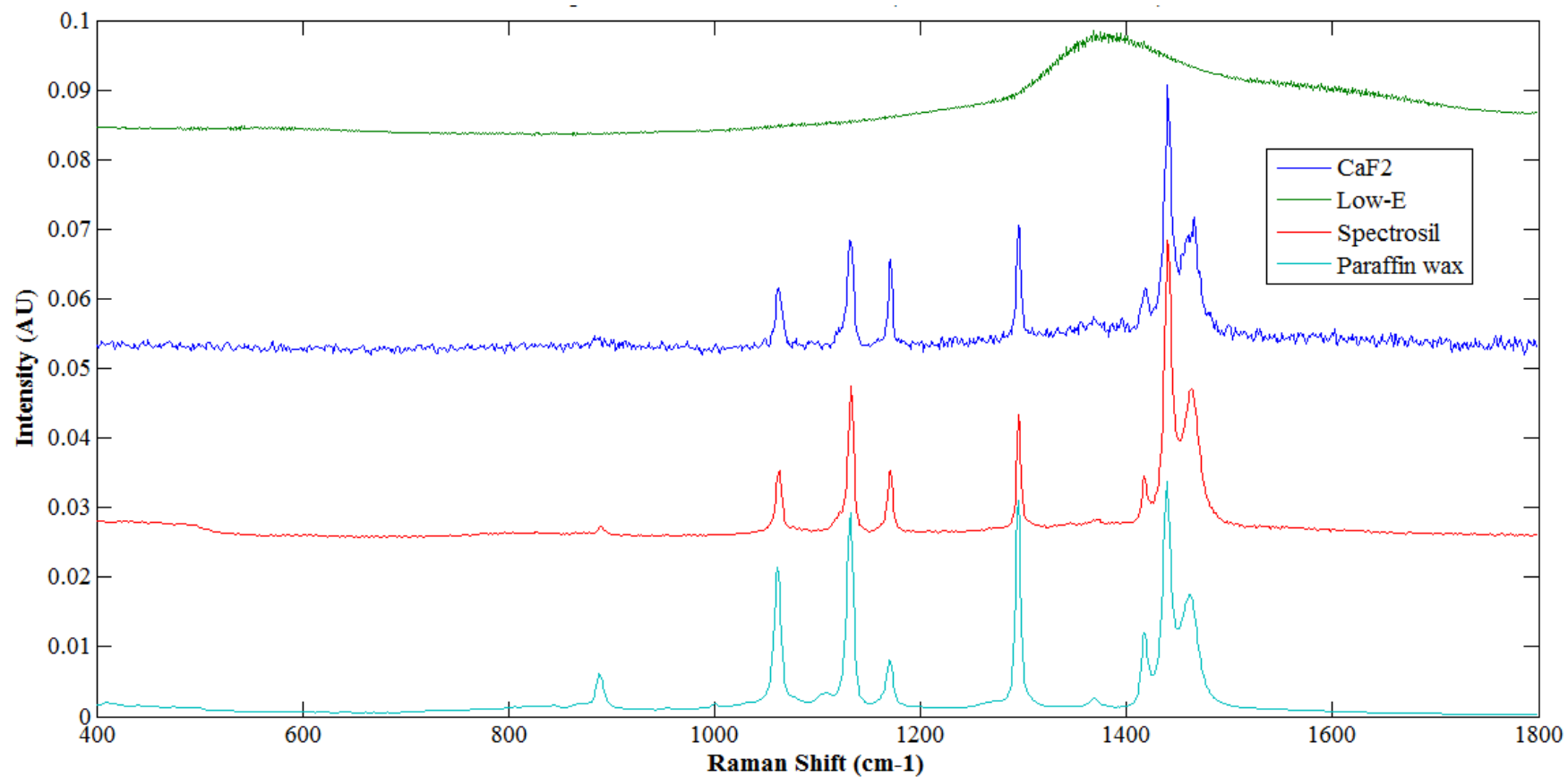


Figure 14: Original spectral plot showing vector normalised, background-subtracted spectra of substrates after dewaxing from: 1 CaF₂ acquisition, 1 Spectrosil acquisition and 10 averaged low-E acquisitions. The raw spectrum of paraffin wax (bottom cyan spectra) is included as a reference. The spectra have been appropriately scaled and offset for visual clarity.

From both Raman analysis and visual inspection it is clear that, using the same dewaxing procedure, the low-E substrate is fully dewaxed, yet the CaF₂ and Spectrosil substrates retain paraffin wax. Residual wax, still present on both the Spectrosil and CaF₂ substrate, could be seen visually both macroscopically and microscopically (Figure 15). Its presence is confirmed by paraffin peak contributions in their spectra. The low-E substrate did not retain any visual paraffin wax and no paraffin peaks were present in the 10 spectra taken at different points along the surface of the substrate. This observation infers that the difference of surface chemistry, properties or morphology between the substrates causes low-E slides to dispel wax more readily than either CaF₂ or Spectrosil. This shows, for the first time, that substrate type has an effect on the dewaxing process. The difference in dewaxing between Low-E, CaF₂ and Spectrosil slides will reflect in the spectra produced from specimen situated on these different substrate types through their input of paraffin contributions.

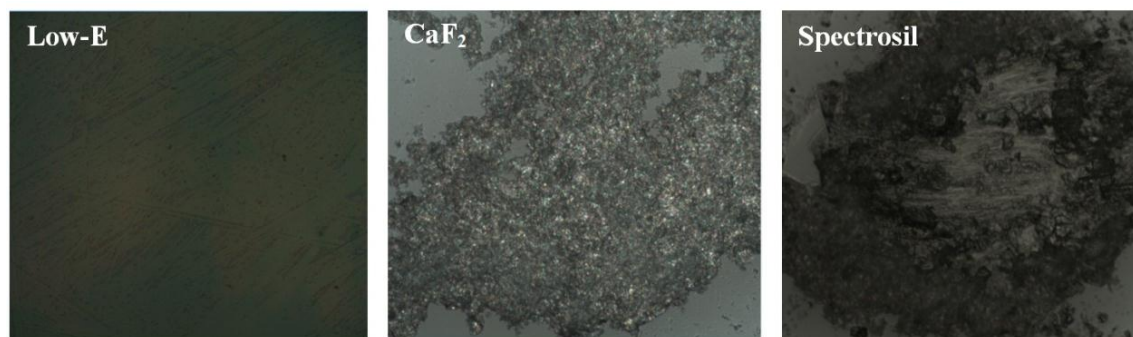


Figure 15: Photographs showing microscopic Raman images at x 10 of the substrate surfaces after dewaxing. Wax residuals can be observed on the CaF₂ and Spectrosil substrates.

Atomic force microscopy (AFM) was used to analyse the three substrates' surface composition. The AFM images of the three substrates are displayed in Figure 16, showing the surface morphology at a nanoscopic level. The low-E substrate was observed to have a far smoother surface than either CaF₂ or Spectrosil with an average

surface roughness of 1.10 nm compared to 4.76 nm and 3.88 nm respectively. Low-E slides are coated with a metal oxide layer [73]. This could provide an explanation for why their surface is far smoother than the other polished substrates.

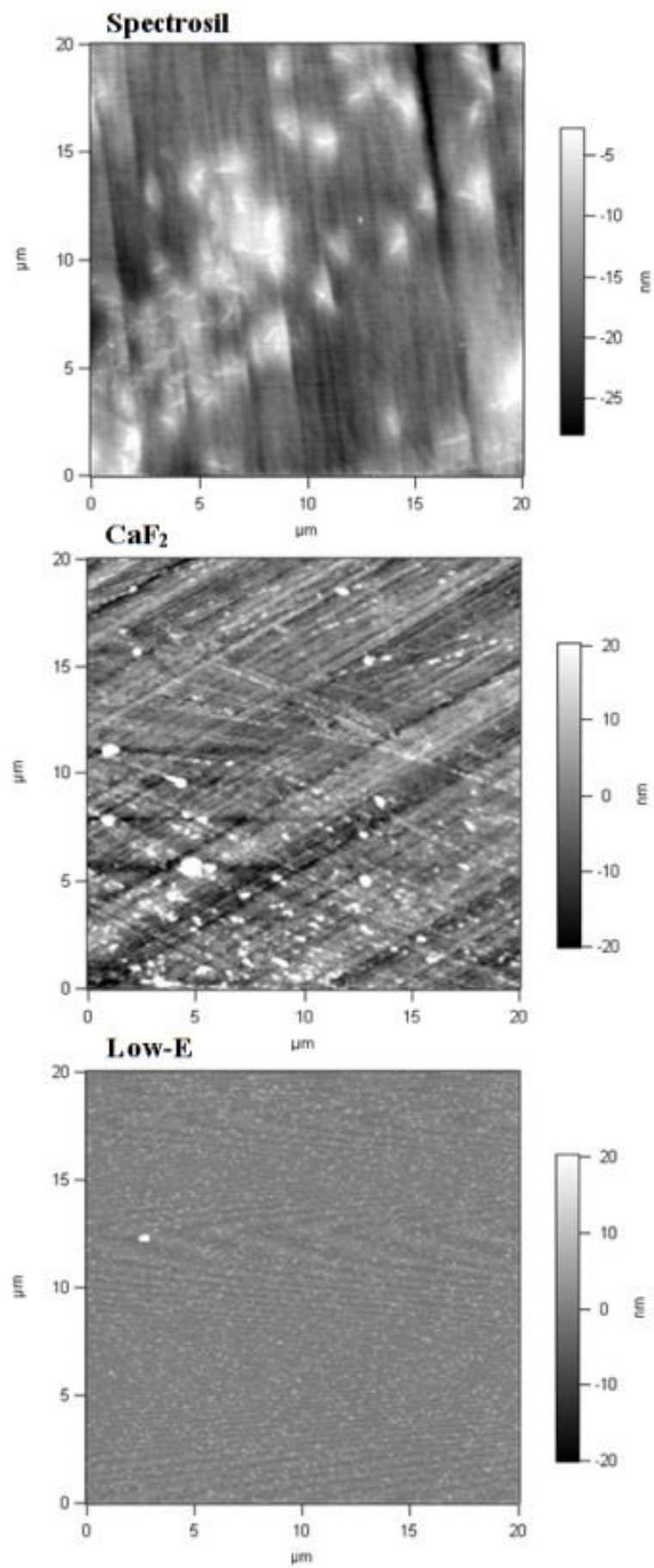


Figure 16: Photographs showing AFM images of Spectrosil, CaF₂ and Low-E substrates.

The clinical application of spectral histopathology is the primary aim of this research field and the ability to fit into the current clinical processes is desired. The use of Low-E slides has more advantages for this application than the other substrates, such as lower cost, larger slide size and higher levels of slide resilience. Although high spectral background and undefined peaks lead to a poor signal-to-noise ratio, spectra generated using low-E substrates still exhibit all the major peaks that are present in the spectra of CaF₂ and Spectrosil. Further work is needed to understand the variation that occurs between the Raman spectra of different substrates and assess the significance of this impact upon clinical application.

3.3 Immersion vs. Non-Immersion Raman spectroscopy

Immersion and non-immersion Raman spectroscopy, using an incident wavelength of 785 nm, are investigated to initially assess the two techniques as diagnostic tools by comparison of the tissue spectra quality produced by both methods.

Spectral acquisition of tissue on Low-E slides was attempted via immersion Raman, but produced a saturated spectral baseline. After observation of a burned hole in the substrate from the live video image, this has been attributed to substrate photodamage caused by the incident laser source. Therefore, CaF₂ substrates were used for further Immersion Raman measurements.

Figure 17 shows the averaged, raw spectra of tissue on CaF₂ using immersion and non-immersion Raman spectroscopy. It is clear that the averaged immersion Raman spectrum initially has a lower spectral background, from 600 cm⁻¹ to 930 cm⁻¹, than the averaged non-immersion spectrum. It remains at a relatively stable intensity throughout

all the Raman shifts. The non-immersion spectrum has an intense spectral background, where it starts at 600 cm^{-1} , but becomes dramatically less intense as the Raman shifts increase, without an increase in the signal-to-noise ratio of the peaks-of-interest. Immersion Raman produces spectra of higher signal-to-noise ratios and peaks with larger areas than those acquired by non-immersion Raman. The observed results give evidence that immersion Raman spectroscopy receives stronger Raman scatter signals than the standard technique.

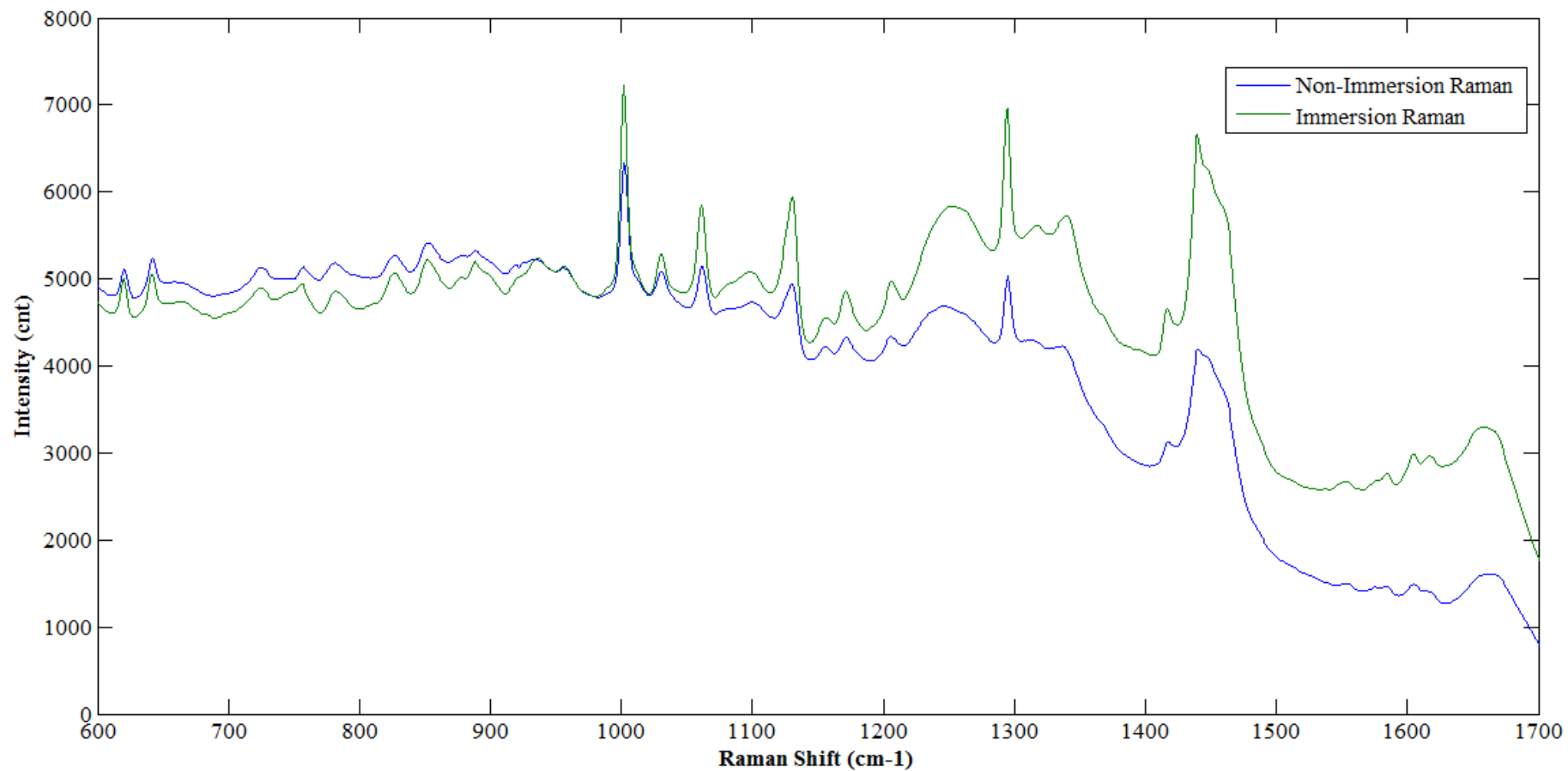
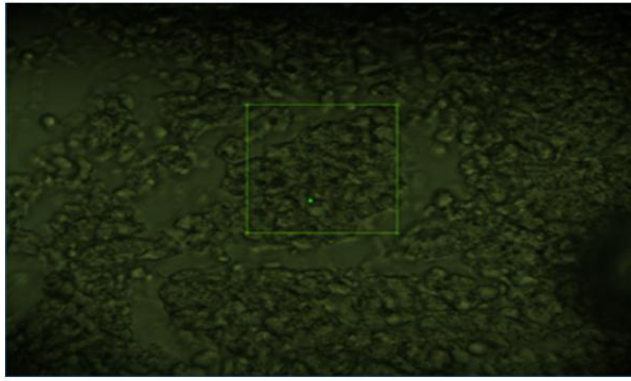


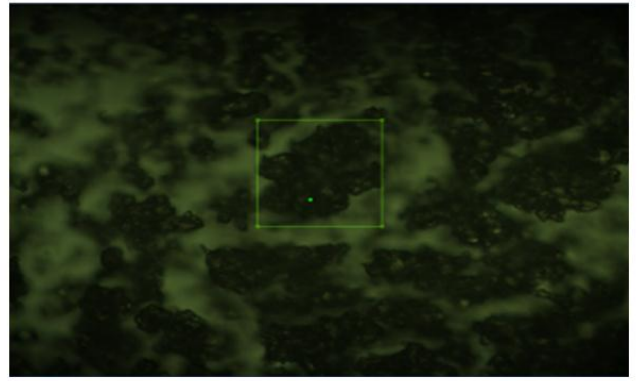
Figure 17: Original spectral plot showing averaged raw spectra of 1116 immersion (48 samples from n=41 patients) acquisitions using, a x 50 objective, and 458 non-immersion acquisitions (18 samples from n=11 patients) using a x 60 objective from all tissue specimens on CaF₂.

In Figure 18 the morphological differences of the same brain tissue sample can be observed between Raman and immersion Raman spectroscopy. The tissue analysed by immersion Raman analysis is saturated in deionised water prior the acquisition of measurements. The cells appear clearly delineated and transparent and the nucleus of cells can also be seen. The cells of the dry tissue are much less delineated and appear as a mass of cells. The heterogeneity of the cell thickness of the dry tissue causes some areas of the sample to look out of focus, whereas the immersed sample is made to look homogenous by their visual clarity throughout the tissue. The transition of the tissue from a dry state to a saturated state was seen through observation of the microscopic image in real time. The tissue was seen to absorb the water and the cells became visually clearer and more demarcated. Full saturation was concluded to occur after approximately 10 minutes when no further visual changes were detected, after this time Raman analysis could proceed and spectroscopic measurements acquired.

The observed advantages, including visual clarity and better spectral quality, led to the further use of immersion Raman spectroscopy, over dry tissue techniques, for the analysis of the tissue samples and assessment of the ability of the technique as a diagnostic tool for metastatic brain cancer.



Immersion Raman image (x 60)



Non-Immersion Raman image (x 50)

Figure 18: Photograph showing Raman (x 50) and immersion Raman (x60) image of brain tissue.

3.4 532 nm vs. 785 nm laser line

Figure 19 shows the averaged, raw spectra of tissue taken using both the 532 nm and 785 nm laser line. It is obvious that the baseline of the averaged spectrum taken using the 785 nm laser line is lower in intensity than the averaged spectrum taken using the 532 nm laser line. As a result of the advantage of a lower spectral background using the 785 nm laser line, its use was continued on tissue spectra acquisition for assessment of its use in spectral histopathology.

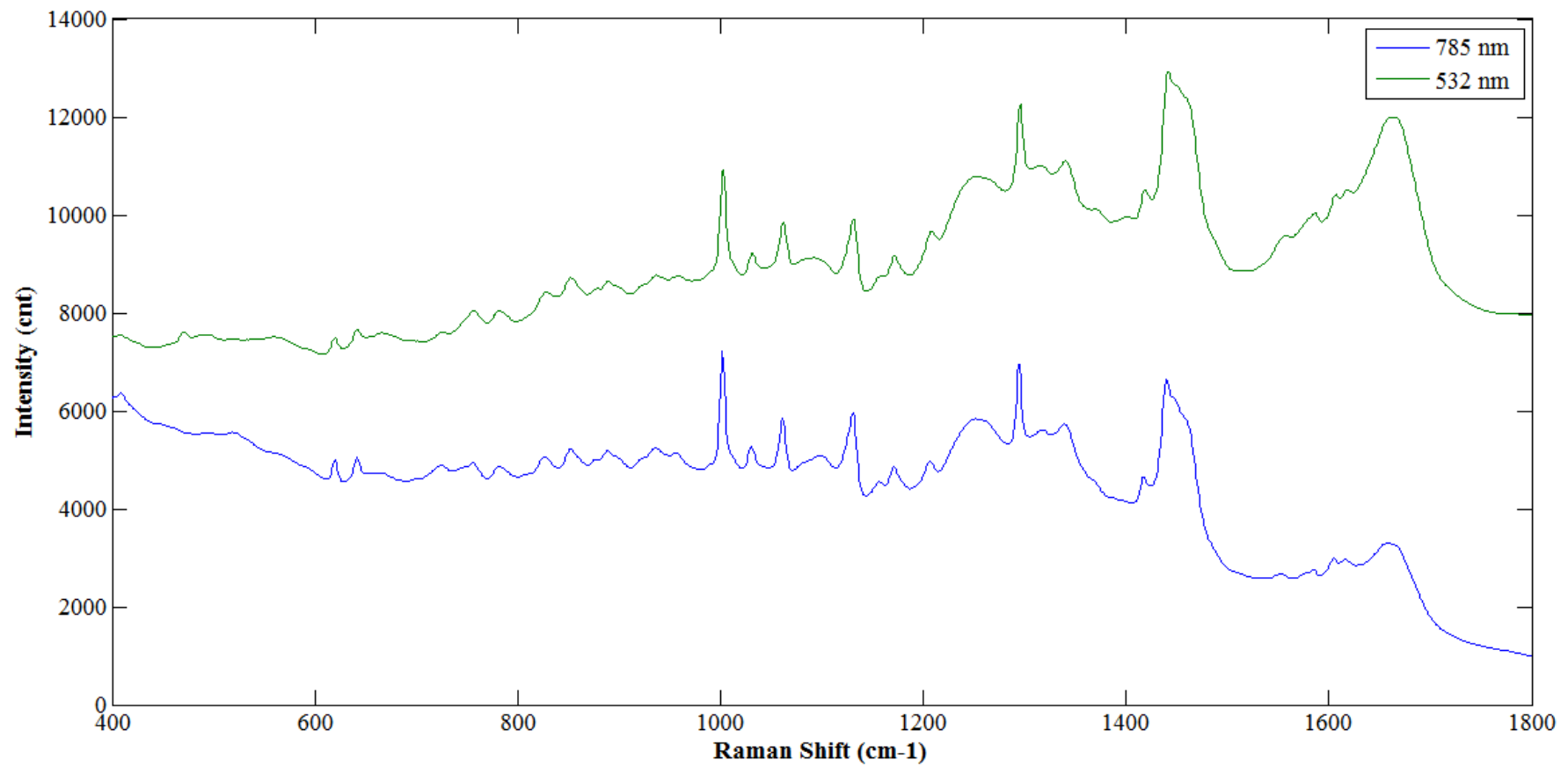


Figure 19: Original spectral plot showing averaged raw immersion Raman spectra of 996 acquisitions (48 samples from n=41 patients) using the 532 nm laser line and 1116 acquisitions (48 samples from n=41 patients) using the 785 nm laser line from all tissue specimens.

3.5 Spectral Histopathology: Discrimination of metastatic tumours

Although low-E substrates were demonstrated to aid tissue dewaxing more efficiently than the other substrates, CaF_2 is a commonly used substrate for Raman spectroscopy due to the small background it produces. CaF_2 was used to support tissue samples under spectral histopathology analysis.

Figure 20 shows the averaged, vector normalised and background-subtracted immersion Raman spectra of normal (157 spectra from 7 patients), metastatic (668 spectra from 31 patients) and GBM (127 spectra from 5 patients) brain tissue on CaF_2 substrates. Table 4 lists the tentative assignments of the major peaks present in these spectra [33, 60, 90-92].

Spectral differences between these tissue types are observed at various peaks throughout the averaged spectra. The peak at 721cm^{-1} , assigned to the C-N symmetric stretch (Figure 21) of choline [90, 91], is prominently observed in GBM tissue. In normal and metastatic tissues this peak is not present, although a 725 cm^{-1} peak assigned to adenine (Figure 21) is present [93]. Choline has been observed, in studies employing magnetic resonance spectroscopy, to increase in content in GBM tissue and all primary tumours. This is thought to be caused by increased cell proliferation and cell membrane turnover, resulting in an increased production of choline transporters and kinase enzymes [94, 95].

Both GBM and metastatic tissues exhibit 782 cm^{-1} peaks of a considerable intensity in their spectra, assigned to nucleotide ring breathing [33] (Figure 21), whereas the peak in the normal tissue spectrum is either absent or of a much weaker intensity,

making it unidentifiable as a major peak. A peak at 1083 cm^{-1} , assigned to the C-N stretch of proteins [33] is observable in the averaged spectrum of normal brain tissue yet appears absent from the spectra of cancerous tissue.

A peak at 1263 cm^{-1} , assigned to CN and CH_2 vibrational modes of amide III [92] (Figure 21), is present in the normal tissue spectrum but is shifted to 1250 cm^{-1} and exhibits higher intensities in the spectra of GBM and metastatic brain tissue. Amide III is a component of the collagen within the tissue samples. Increased collagen in cancerous tissue is consistent with other Raman spectroscopy studies and is attributed to fibrosis association with lesion formation [96]. Additionally, women with dense breast tissues, which are normally associated with increased collagen, are found to have an elevated chance of developing breast cancer [97].

The peak present at approximately 1658 cm^{-1} is attributed to the C=O stretch of amide I [33], and appears to be shifted in the average spectrum of metastatic tissues to a higher Raman shift of 1661 cm^{-1} . The intensity of this peak is also decreased in both the cancerous spectra. This is consistent with the results of Gniadecka *et al.* who found reduced intensities of the amide I band of proteins in the spectra of melanoma. The changes in the amide bands between the normal and melanoma specimens are attributed to conformational changes to the protein structures [98].

Intensity changes between spectral peaks of normal, GBM and metastatic brain tissue indicate alterations in specific biomolecule concentrations when the tissue is in different states of health. These observable spectral differences demonstrate the ability of Raman spectroscopy as a potential diagnostic tool for brain cancer.

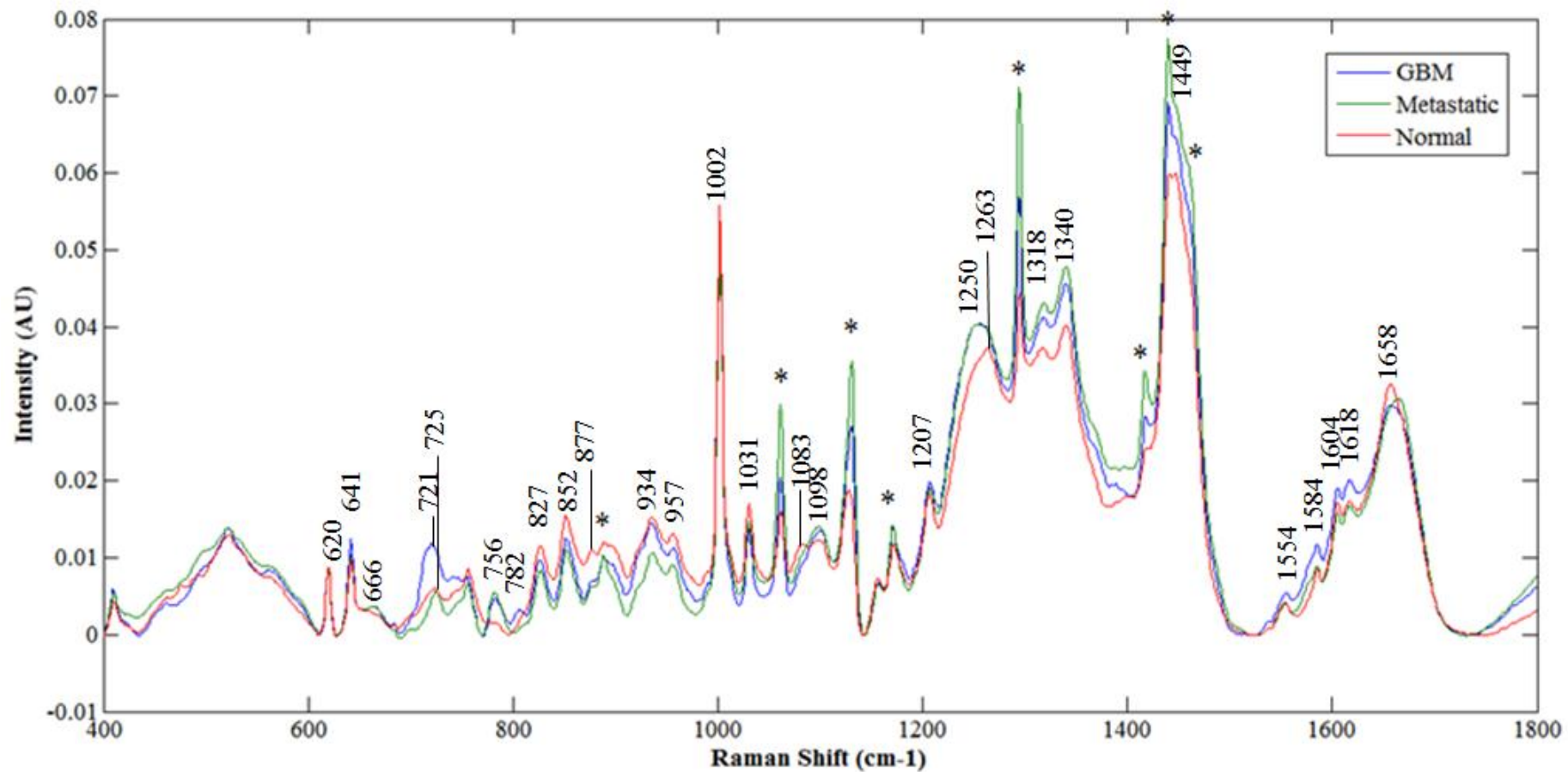


Figure 20: Original spectral plot showing averaged immersion spectra of 127 GBM acquisitions (n=5 patients), 668 metastatic acquisitions (n=29 patients) and 157 normal brain acquisitions (n=7 patients). Spectra have been vector normalised, the backgrounds have been corrected using a 5th order polynomial fit and subtraction and 7 points of smoothing. The asterisks correspond to paraffin peaks from residual wax in the tissue.

Table 4: Data showing tentative biomolecular assignments of main spectral peaks.

Raman Shift (cm⁻¹) of peak	Tentative assignment [33, 60, 90-92]
620	C-C twisting mode of phenylalanine
641	C-C twisting mode of tyrosine
666	C-S stretching mode of cystine
721 (only GBM)	Symmetric choline C-N stretch (membrane phospholipid head)/adenine
725	Adenine/C-S (protein)/C-H ₂ rocking
756	Symmetric breathing of tryptophan
782	Cytosine/uracil ring breathing of nucleotide
827	DNA O-P-O, cytosine, uracil, thymine
852	(CCH) ring breathing mode of tyrosine and C-C stretch of proline ring
877	Proline
888	Paraffin wax
934	C-C stretching mode of proline and valine and α -helix protein backbone/glycogen
957	Hydroxyapatite (PO ₄ ³⁻ symmetric stretching) /carotenoid/cholesterol
1002	Symmetric ring breathing mode of phenylalanine
1031	C-H in-plane bending mode phenylalanine
1061	Paraffin wax
1083 (only normal)	C-N stretching mode of proteins
1098	C-C/C-O phospholipids
1131	Paraffin wax
1156	C-C carotenoids, C-N stretching of proteins
1171	Paraffin wax
1207	Tyrosine, Hydroxyproline/tryptophan, phenylalanine (C-C ₆ H ₅)
1250	Amide III: collagen (C-H ₂ wag, C-N stretch)/Pyrimidine bases C, T
1263 (only normal)	Amide III: collagen (C-H ₂ wag, C-N stretch)/Pyrimidine bases C, T
1294	Paraffin wax

1318	CH ₃ CH ₂ twisting mode of collagen/lipids
1340	CH ₃ CH ₂ wagging mode of collagen, nucleic acids
1389	CH ₃ bend
1417	Paraffin wax
1440	Paraffin wax
1449	CH ₂ bending mode of proteins/(CH ₃) (CH ₂) collagen
1462	Paraffin wax
1554	C=C Tryptophan, porphyrin
1584	Pyrimidine ring (nucleic acids) and heme protein/C=C phenylalanine
1604	C=C in-plane bending mode of phenylalanine and tyrosine, C=C porphyrin
1618	C=C stretching mode of tyrosine and tryptophan
1658	Amide I (C=O stretching mode of proteins, α -helix conformation)/C=C lipid stretch

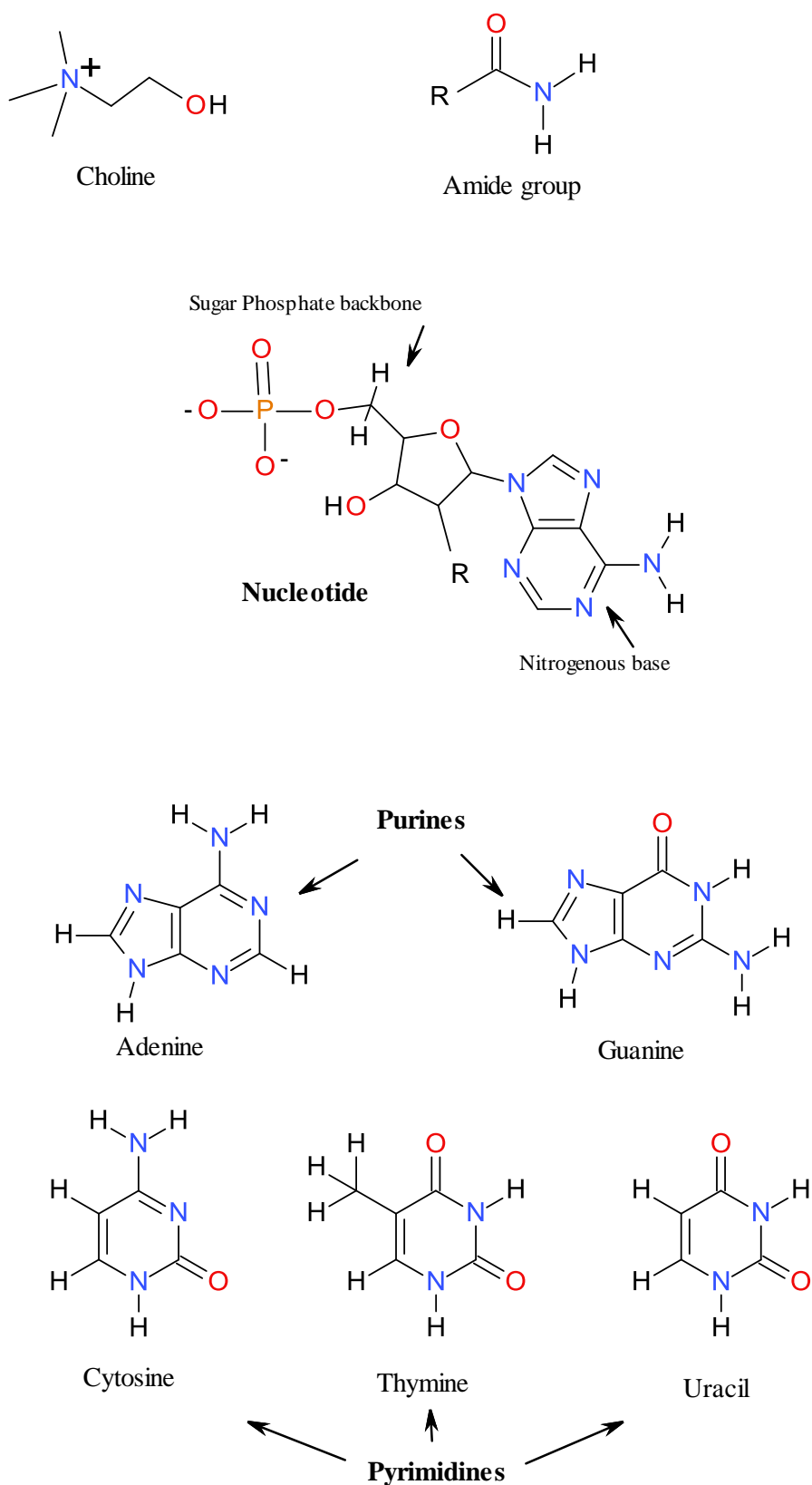


Figure 21: Chemical structures of choline, amide, nucleotide and the bases of nucleotides: adenine, guanine, cytosine, thymine and uracil, which contribute to peaks in the spectral differences between GBM, normal and metastatic brain tissue.

It can be seen from Figure 22, that on a spectral level the data assembles together in their histopathological groups for GBM, metastatic and normal brain respectively. However, there is a degree of overlap between the groups. Details of the PC-DFA model and the number of spectra used can be found in Table 5. At a 95% confidence limit, GBM classification has a sensitivity of 95.24% and a specificity of 36.13%, metastatic classification has a sensitivity of 95.47% and a specificity of 81.05% and normal brain classification has a sensitivity of 90.38 % and a specificity of 56.82%. At a 90% confidence interval GBM classification has a sensitivity of 92.86% and a specificity of 72.63%, metastatic classification has a sensitivity of 91.82% and a specificity of 90.43% and normal brain classification has a sensitivity of 88.46% and a specificity of 78.41%.

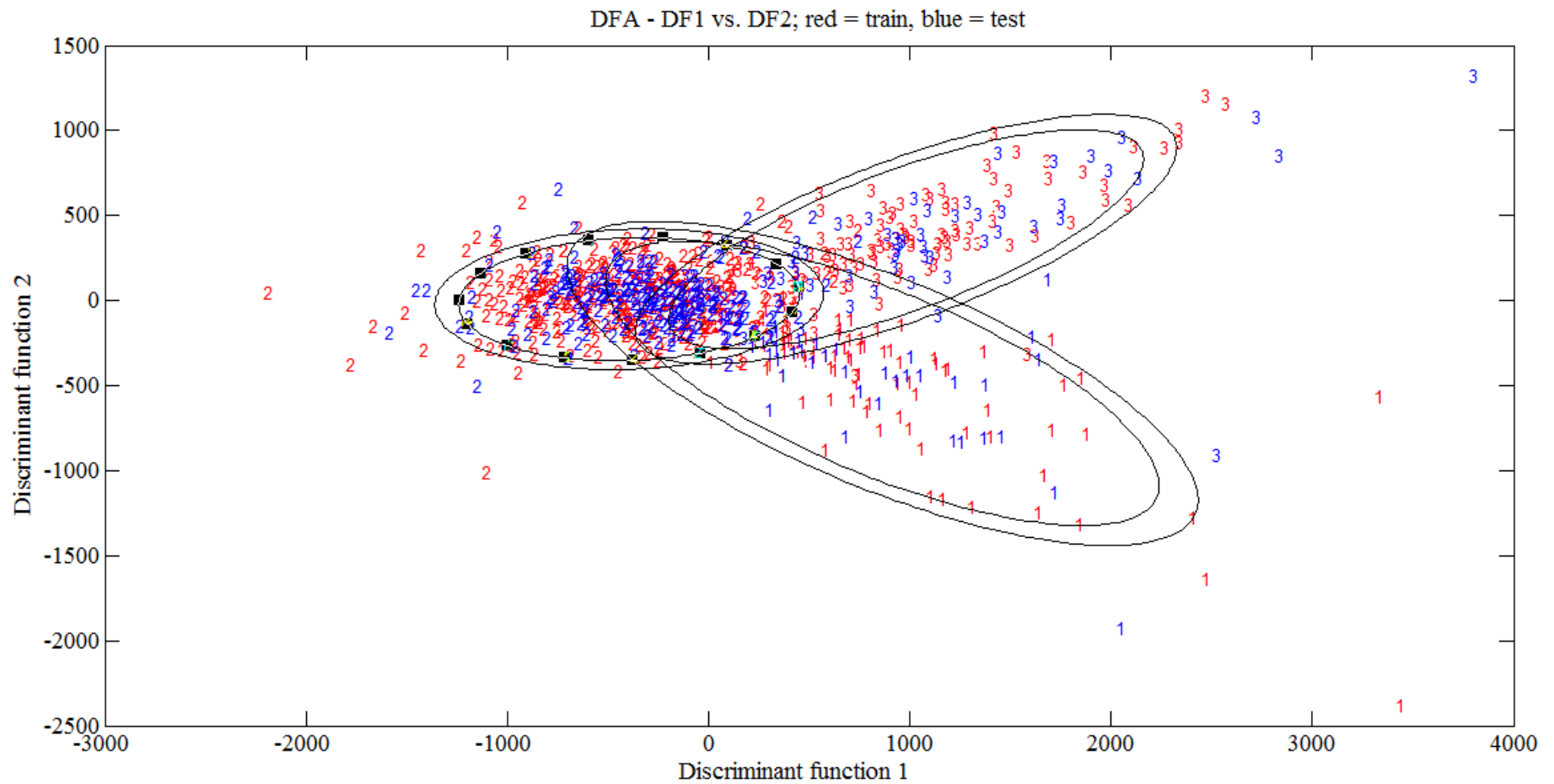


Figure 22: Original discriminant function plot showing the separation between GBM (n=5 patients) (1), metastatic (n=29 patients) (2) and normal (n=7 patients) (3) brain tissue, at spectral level, based on the training set (red) and test set (blue) with 95% (outer ellipse) and 90% (inner ellipse) confidence limits.

Table 5: Data showing the PC-DFA model details, including spectral numbers and the resulting sensitivities and specificities.

		Train	Test	Confidence	Histopathological	Sensitivity	Specificity
		spectra	spectra	level	type	(%)	(%)
GBM vs. norm vs. met		639	316	90%	GBM	92.86	72.63
					Normal	88.46	78.41
					Metastatic	91.82	90.43
				95%	GBM	95.24	36.13
					Normal	90.38	56.82
					Metastatic	95.47	81.05
Metastatic comparison		449	222	95%	Breast	95.74	44
					Lung	93.75	30.38
					Colon/Rectum	76.08	50
					Melanoma	97.06	20.21
					Oesophagus & stomach	96.67	47.64
primary comparison		111	53	95%	Breast	77.42	89.66
					Colon/Rectum	57.14	100
					Melanoma	100	55.56
					Oesophagus & stomach	14.29	100
				99%	Breast	87.1	86.36
					Colon/Rectum	71.43	100
					Melanoma	100	42.22
					Oesophagus & stomach	42.86	100

Figure 23 displays the discriminant function loadings plots relating to this PC-DFA and Table 6 identifies the Raman shifts of the main peaks. The loadings contain

the peaks 721 cm^{-1} , 725 cm^{-1} and 782 cm^{-1} which were visibly identified as being different in the metastatic, normal and GBM brain tissue spectra. Therefore, the discriminatory power of these peaks were further tested through calculation of their ratios to the 620 cm^{-1} peak, which appeared to be more uniform across the spectra, to analyse the importance of the intensity differences between the spectra.

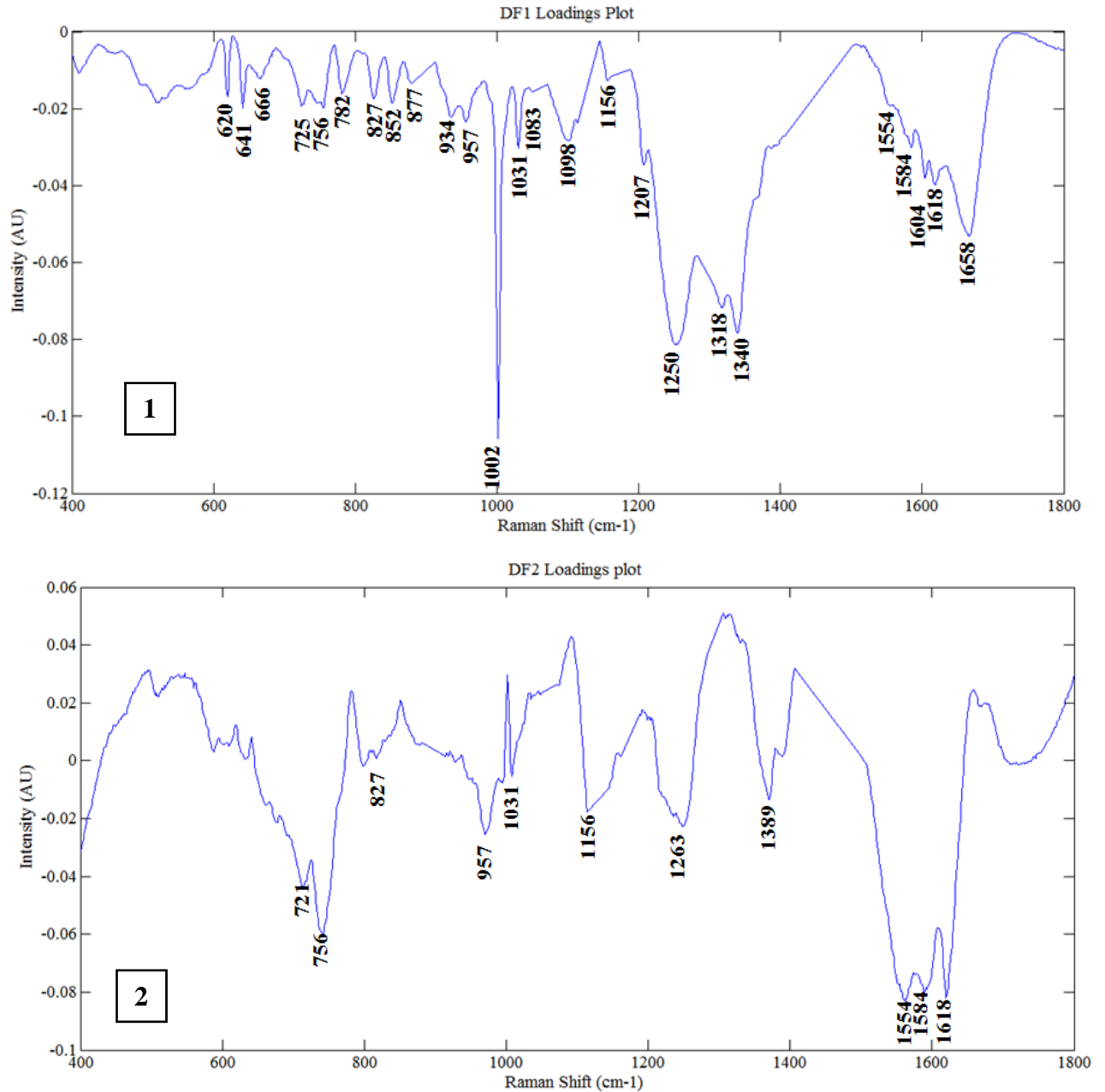


Figure 23: PC-DFA loadings plot of discriminant functions 1 and 2 from the GBM vs. metastatic vs. normal (Figure 9) PC-DFA model.

Table 6: Data showing the Raman shifts of the main peaks from the PC-DFA loadings.

Raman Shift (cm⁻¹) of PC-DFA loadings peak	
DF 1 loadings	DF2 loadings
620	721
641	756
666	827
725	957
756	1031
782	1156
827	1263
852	1389
877	1554
934	1584
957	1618
1002	
1031	
1083	
1098	
1156	
1207	
1250	
1318	
1340	
1554	
1584	
1604	
1618	
1658	

Figure 24 displays the 2D score plot of peak intensity ratios and further shows separation between metastatic, GBM and normal brain tissues based on the intensity ratios of the 620 cm^{-1} peak, which is uniform in all the spectra, to the 782 cm^{-1} peak, which appears absent in normal brain, and the 721 cm^{-1} peak, present in only GBM tissue spectra. It can be seen that the ratios calculated from the spectra of GBM, metastatic and normal brain tissue clearly group together in their tissue types. Two outliers can be seen from the ratio graph at location (1.45, 2.19) and (1.9, 1.09), belonging to the normal and metastatic group, identified as patient 007 and 509 respectively. Upon inspection of these patients' averaged spectra, it was observed that they notably differed from the other averaged spectra from the same histological group and also from the total averaged spectra of the histological group.

GBM classification has a sensitivity of 100% and a specificity of 94.44% based on the 721 cm^{-1} to 620 cm^{-1} ratio data above 1. Metastatic classification has a sensitivity of 96.55% and a specificity of 100% based on the 721 cm^{-1} to 620 cm^{-1} ratio data below 1 and 620 cm^{-1} to 782 cm^{-1} ratio data below 5, respectively. Moreover, normal brain classification has a sensitivity of 85.71% and a specificity of 100% based on the 721 cm^{-1} to 620 cm^{-1} ratio data below 1 and 620 cm^{-1} to 782 cm^{-1} ratio data above 5. The ratios of peaks in the low wavenumber regions, $600\text{-}800\text{ cm}^{-1}$, allow rapid, directed Raman analysis to discriminate GBM, metastatic and normal brain tissue.

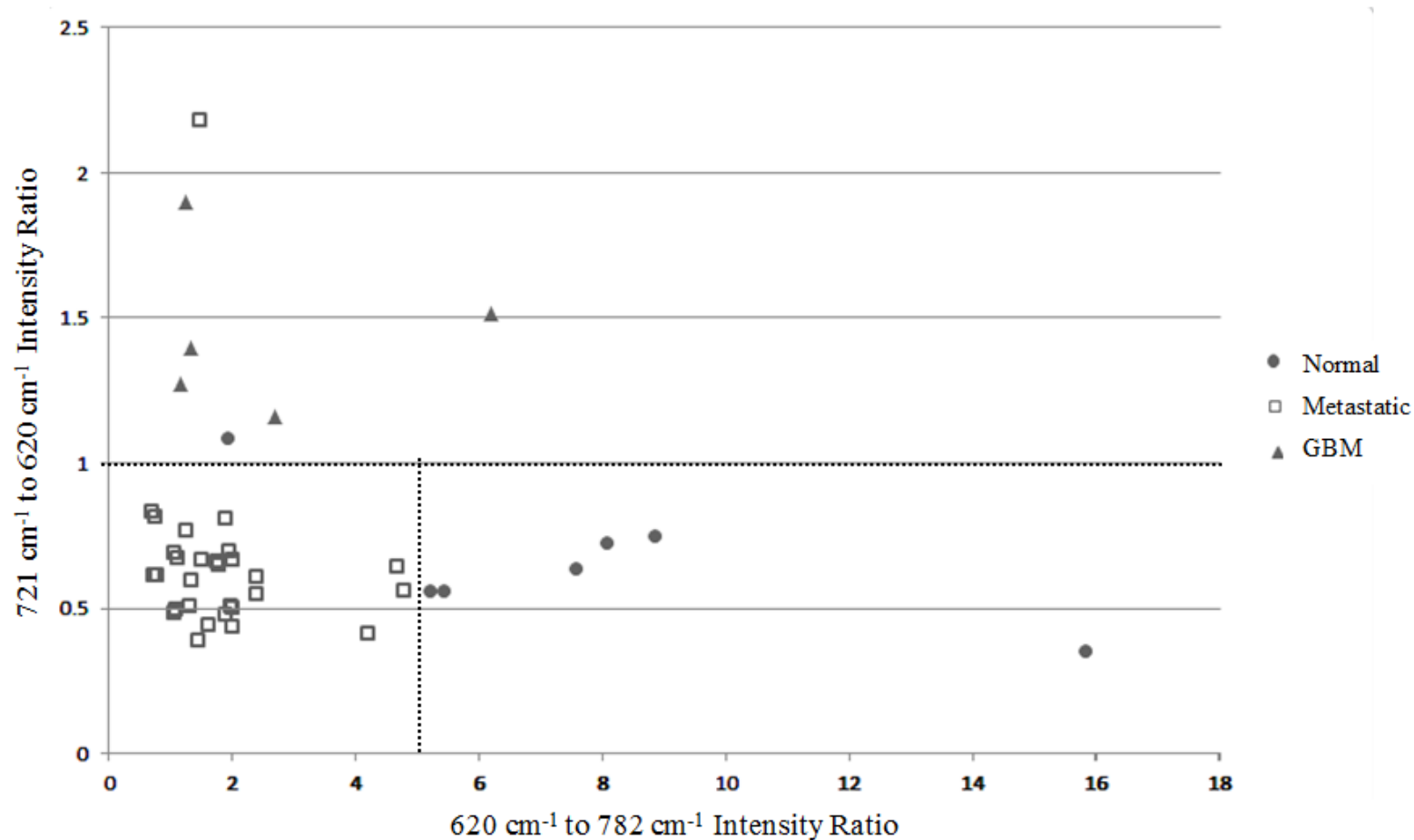


Figure 24: 2D score plot of the 620 cm⁻¹ to 782 cm⁻¹ peak ratio versus the 721 cm⁻¹ to 620 cm⁻¹ peak ratio. Each data point is the patient average (n≥20 spectra per specimen) from normal (n=7 patients), metastatic (n=29 patients) and GBM (n=5 patients) spectra that have been vector normalised and 5th order polynomial subtracted.

It can also be observed from Figure 20 (page 59), that the averaged spectrum of normal tissue that the paraffin peaks (asterisked peaks) present are of a much lower intensity than those in the spectra acquired from metastatic and GBM tissue. This could be attributed to either structural or compositional differences between the tissue types showing a tissue effect on the dewaxing efficacy as well as a substrate effect.

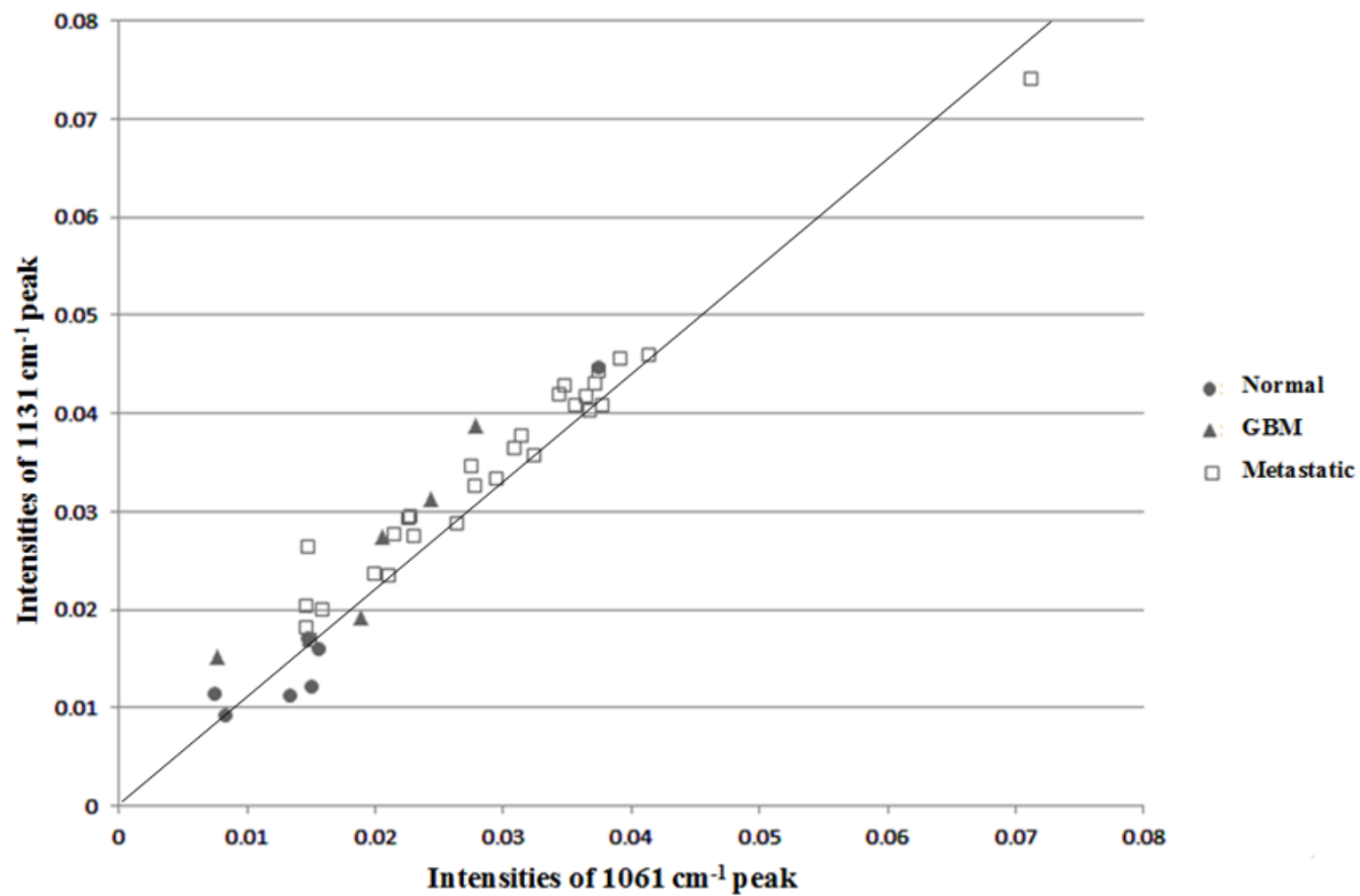


Figure 25: Score plot of intensity measurements from the 1061 cm⁻¹ peak and the 1131 cm⁻¹ peak of patient averaged normal, GBM and metastatic spectra.

Figure 25 shows the score plot of the intensities of the paraffin peaks: 1061 cm^{-1} against 1131 cm^{-1} , from patient averaged spectra. It can be seen that the paraffin peaks from normal brain tissue spectra generally exhibit lower intensities than the cancerous tissue spectra. As a result the normal brain tissue data group together at the lower intensity range of the score plot and the cancerous brain tissue data group together at the higher intensity range on the score plot. The disparity of wax retention between these different histological tissues could perhaps be used to tentatively highlight cancerous areas in the tissue and differentiate between cancerous and normal tissue. The spectra within the GBM group appear to be less uniform and displays paraffin peaks of both high and low intensities which can overlap with those from the metastatic spectra. As a result, it would be more challenging to differentiate between GBM and metastatic tissue to a reliable level and combining the two groups together, as cancerous tissue, gives a better indication of the disparity of dewaxing efficacy between normal and cancerous specimens.

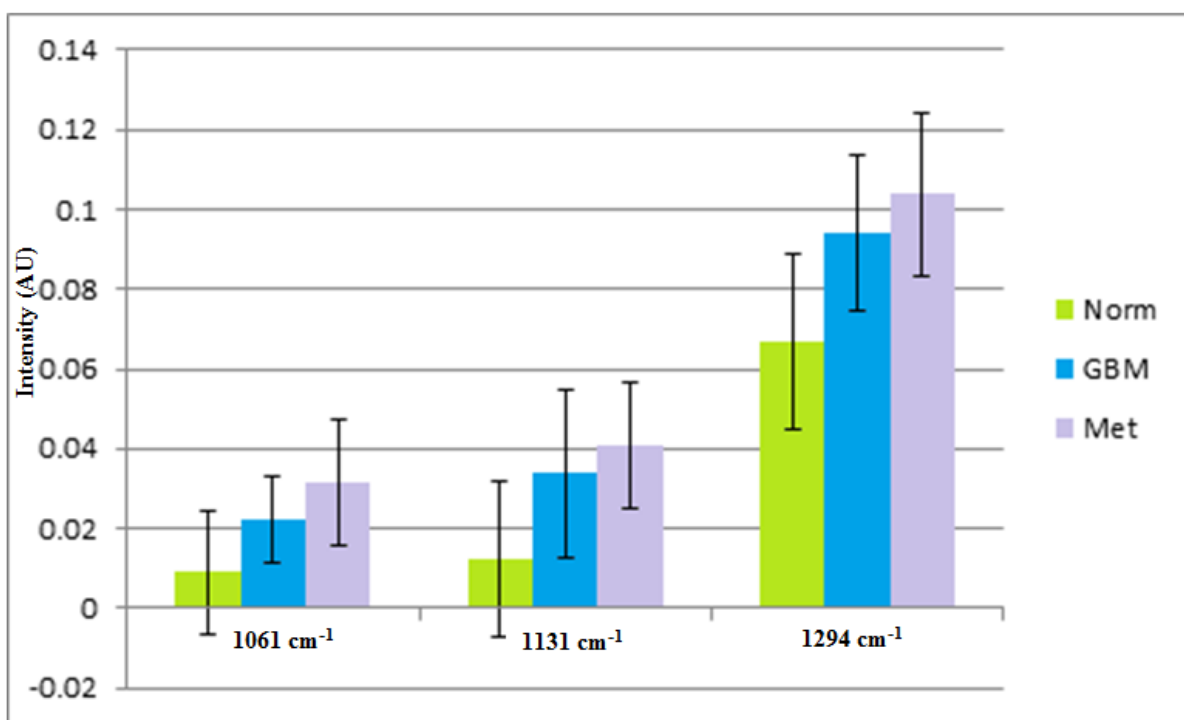


Figure 26: Bar chart of three paraffin peak intensities with standard deviation from 127 GBM acquisitions (n=5 patients), 668 metastatic acquisitions (n=29 patients) and 157 normal brain acquisitions (n=7 patients) on CaF_2 substrates.

Figure 26 shows the standard deviations of intensity across the spectra from paraffin peaks 1061 cm^{-1} , 1131 cm^{-1} and 1294 cm^{-1} . It can be observed from the graph that there is a general trend for higher paraffin peak intensities in the spectra of metastatic and GBM tissue than in the spectra of normal tissue specimens.

Li *et al.* [99] state that the amount of fibro-glandular and adipose tissue is strongly related to the risk of developing breast cancer. They explain that although no direct evidence has been found to link dense mammographic tissue with the increased chance of developing breast cancer, the obvious correlations observed have encouraged the use of tissue density for breast cancer monitoring. They go on to support the observations of this correlation through their findings that the mammograms of cancerous breast tissue are far denser than those of normal breast tissue [99]. The modification in tissue density observed between normal and cancerous tissue could provide an explanation for the efficiency inconsistency of the dewaxing procedure, and thus the variation of paraffin peak intensity between the normal brain and cancerous brain tissue spectra. It would appear that the denser, cancerous tissue retains paraffin wax better than the less dense, normal tissue.

Figure 27 shows the averaged spectra of GBM and normal brain tissues, and metastatic: breast, lung, colon/rectum, melanoma and oesophagus and stomach brain tissues. No visible differences between the spectra of the metastases based on their origins are apparent.

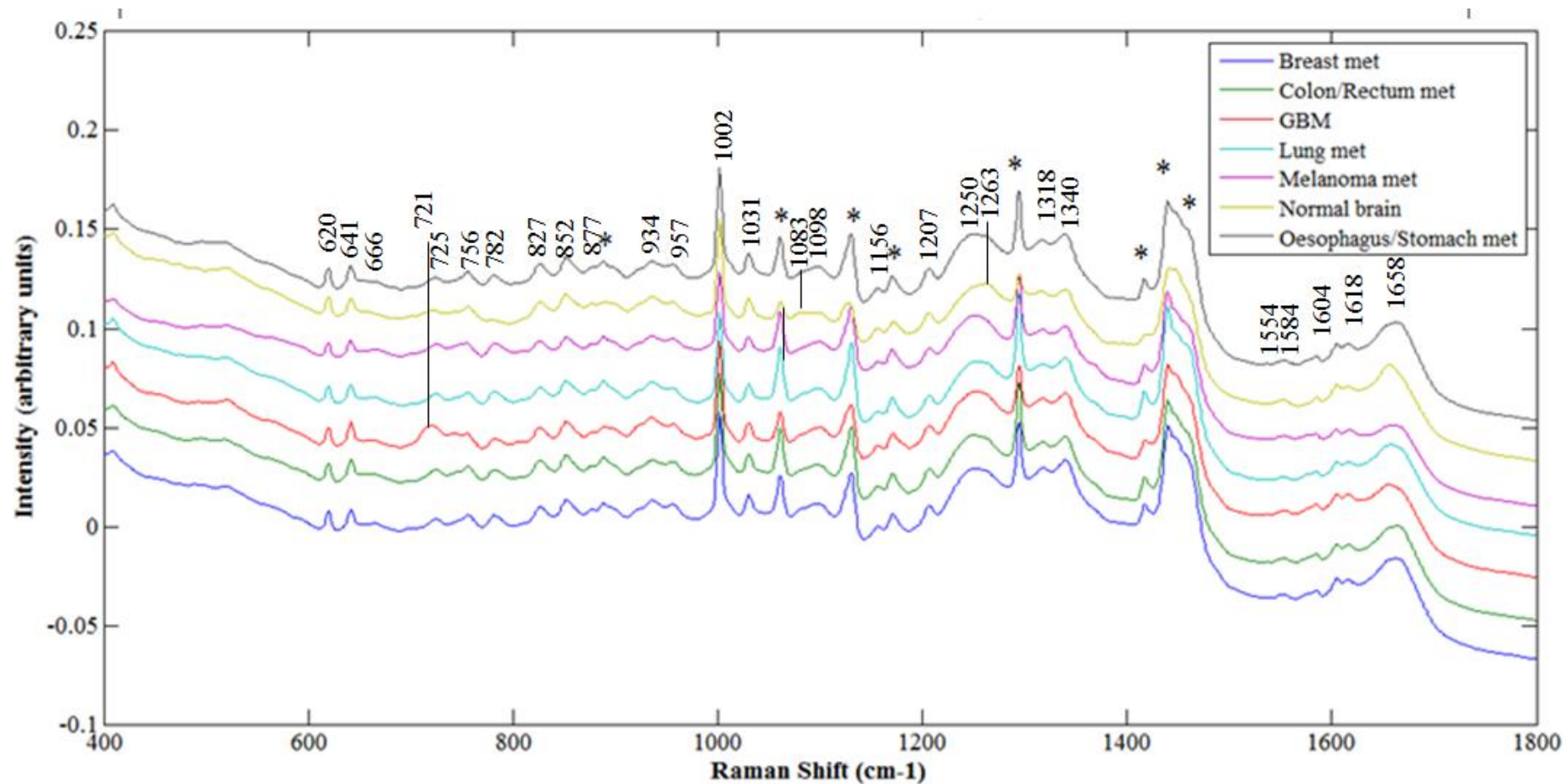


Figure 27: Original spectral plot of averaged immersion spectra: 141 breast met acquisitions (n=6), 138 colon/rectum met acquisitions (n=6), 127 GBM acquisitions (n=5), 194 lung met acquisitions (n=8), 102 melanoma met acquisitions (n=5), 157 normal brain acquisitions (n=7) and 93 oesophagus and stomach met acquisitions (n=4). Spectra have been vector normalised and offset for visual clarity. The asterisks represent the paraffin contributed peaks.

Figure 28 shows the PC-DFA was performed on the metastatic tissues data. It can be seen that, although there is a large amount of overlap between the classes, the tissue types generally group together showing the potential for primary cancer site identification from analysis of the metastatic brain tissue. Details of the PC-DFA can be found in Table 5. In particular, the melanoma metastases and breast metastases show the clearest separation from each other and the others groupings. At a 95% confidence limit breast met classification has a sensitivity of 95.74% and a specificity of 44.00%. Colon/rectum met classification has a sensitivity of 76.08% and a specificity of 50.00%. Lung met classification has a sensitivity of 93.75% and a specificity of 30.38%. Melanoma met classification has a sensitivity of 97.06% and a specificity of 20.21%. Oesophagus and stomach met classification has a sensitivity of 96.67% and a specificity of 47.64%.

Although their classification sensitivities are considerably high, the low classification specificities would result in a high number of false positives based on this PC-DFA model.

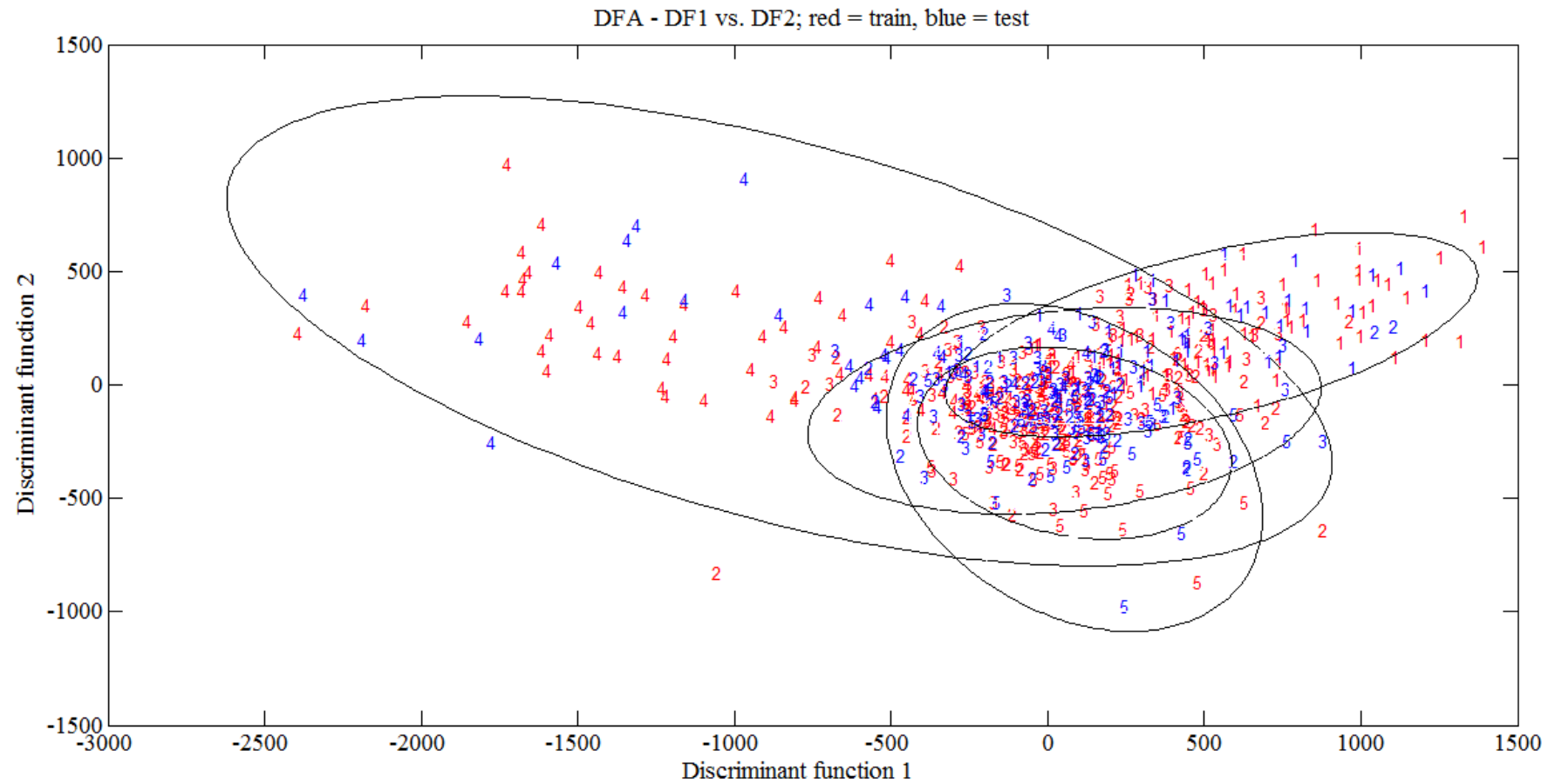


Figure 28: Original discriminant function plot displaying the separation of breast met (n=6 patients) (1), colon/rectum met (n=6 patients) (2), lung met (n=8 patients) (3) melanoma met (n=5 patients) (4) and oesophagus & stomach met (n=4 patients) (5) based on the train set (red) and test set (blue) with a 95% confidence limit represented by ellipse.

PC-DFA was performed on the primary cancers spectral dataset: breast, melanoma, oesophagus and stomach and colon/rectum. Primary lung tissue specimens were not available in the biobank. Details of the PC-DFA model are displayed in Table 5. The primary cancer tissue samples are linked samples, from the same patient as the corresponding metastatic tissue samples used in the metastatic tumour model. As can be seen in Figure 29, the tissue types separate well and crossover is only observed between the breast and melanoma cancers. At a 95% confidence limit breast cancer classification has a sensitivity of 77.42% and a specificity of 89.66%. Colon/rectum cancer classification has a sensitivity of 57.14% and a specificity of 100%. Melanoma cancer classification has a sensitivity of 100% and a specificity of 55.56%. Oesophagus and stomach cancer classification has a sensitivity of 14.29% and a specificity of 100%. At a 99% confidence limit breast cancer classification has a sensitivity of 87.10% and a specificity of 86.36%. Colon/rectum cancer classification has a sensitivity of 71.43% and a specificity of 100%. Melanoma cancer classification has a sensitivity of 100% and a specificity of 42.22%. Oesophagus and stomach cancer classification has a sensitivity of 42.86% and a specificity of 100%. The primary cancer tissues show much better separation than the metastatic tissues in their PC-DFA models. Hence, the spectra produced from the brain metastases in this study must be comparatively different from those produced from their primary site cancers. Metastatic types are more spectrally alike than primary cancers are to each other. This may suggest a change in the biochemistry of the cancer cells depending on organ location and not cancer type. However, due to only a small number of primary tissue specimens investigated in this study no accurate conclusions can be made, as variations may arise from molecular differences between patients rather than disease.

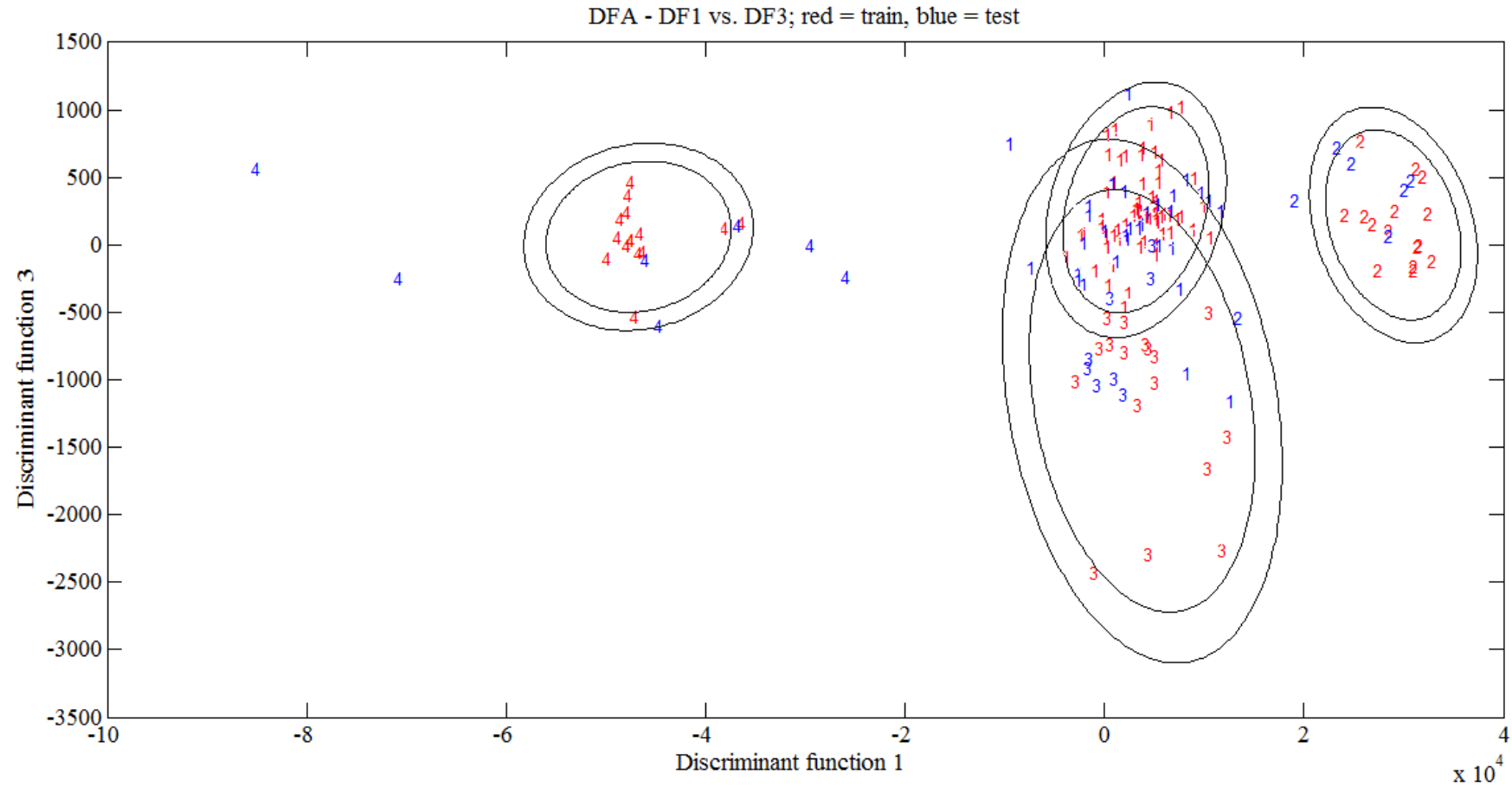


Figure 29 Original discriminant function plot displaying the separation of primary breast (n=5 patients) (1), primary colon/rectum (n=1 patients) (2), primary melanoma (25 spectra from n=1 patients) (3) and primary oesophagus & stomach (n=1 patients) (4) cancers based on the train set (red) and test set (blue) with 99% (outer ellipse) and 95% (inner ellipse) confidence limits.

Figure 30 displays the baseline-subtracted and vector normalised, averaged spectra of both metastatic brain and their corresponding primary sites. From the results, it is observable that they spectrally vary from one another in their peak intensities. This supports the difference in grouping between their PC-DFA models and further suggests that the biomolecular composition of tissue differs between the primary sites and the corresponding brain metastases.

A uniform difference that appears between all the metastatic brain tissue spectra and the primary site tissue spectra is seen in the amide I peak. In metastatic brain tissue spectra it peaks as high as 1667 cm^{-1} , in stomach/oesophagus metastases, a higher Raman shift than the primary sites which peak at around 1658 cm^{-1} .

The averaged spectra of breast cancer tissue and the corresponding metastatic brain tissue appear relatively similar to one another. The main difference between these two groups is a peak at 700 cm^{-1} present in the metastatic brain tissue spectrum but not visually present in the primary site tissue spectrum.

Colon cancer tissues and the metastatic brain tissues are also spectrally similar to each other and vary mainly through the difference in peak intensities. The primary site tissue spectrum exhibits much higher intensity peaks than the spectrum of metastatic brain tissue. The primary site tissue spectrum also displays a much more visually obvious peak at 666 cm^{-1} than the metastatic brain tissue spectra.

The spectral difference between oesophagus and stomach cancer tissues and metastatic brain tissues are far more obvious than between the spectra of the other cancers. The most noticeable disparity between the two averaged spectra is due to the

peak at 1621 cm^{-1} which is much more intense in the primary site spectrum than the metastatic brain spectrum. Furthermore, the amide I peak, at 1658 cm^{-1} is much less intense in the primary site spectrum than the metastatic brain spectrum which produces an unusual ratio between the two peaks. This unusual ratio is only exhibited in the oesophagus and stomach cancer spectrum. However, the spectra of both the primary and metastatic site, for the other cancers exhibit similar ratios for these peaks where the Amide I is much more intense than the 1621 cm^{-1} peak. A peak at 796 cm^{-1} is displayed in the primary site spectrum of the oesophagus and stomach but is not present in the spectrum of metastatic brain.

The spectral differences between melanoma primary site and metastatic tissue are between the peak intensities. The amide III peak at 1250 cm^{-1} is at a similar intensity to the 1340 cm^{-1} peak in the metastatic tissue spectrum. In the primary site spectrum there is a disparity between these two peaks with the 1340 cm^{-1} peak having a much higher intensity than the amide III peak.

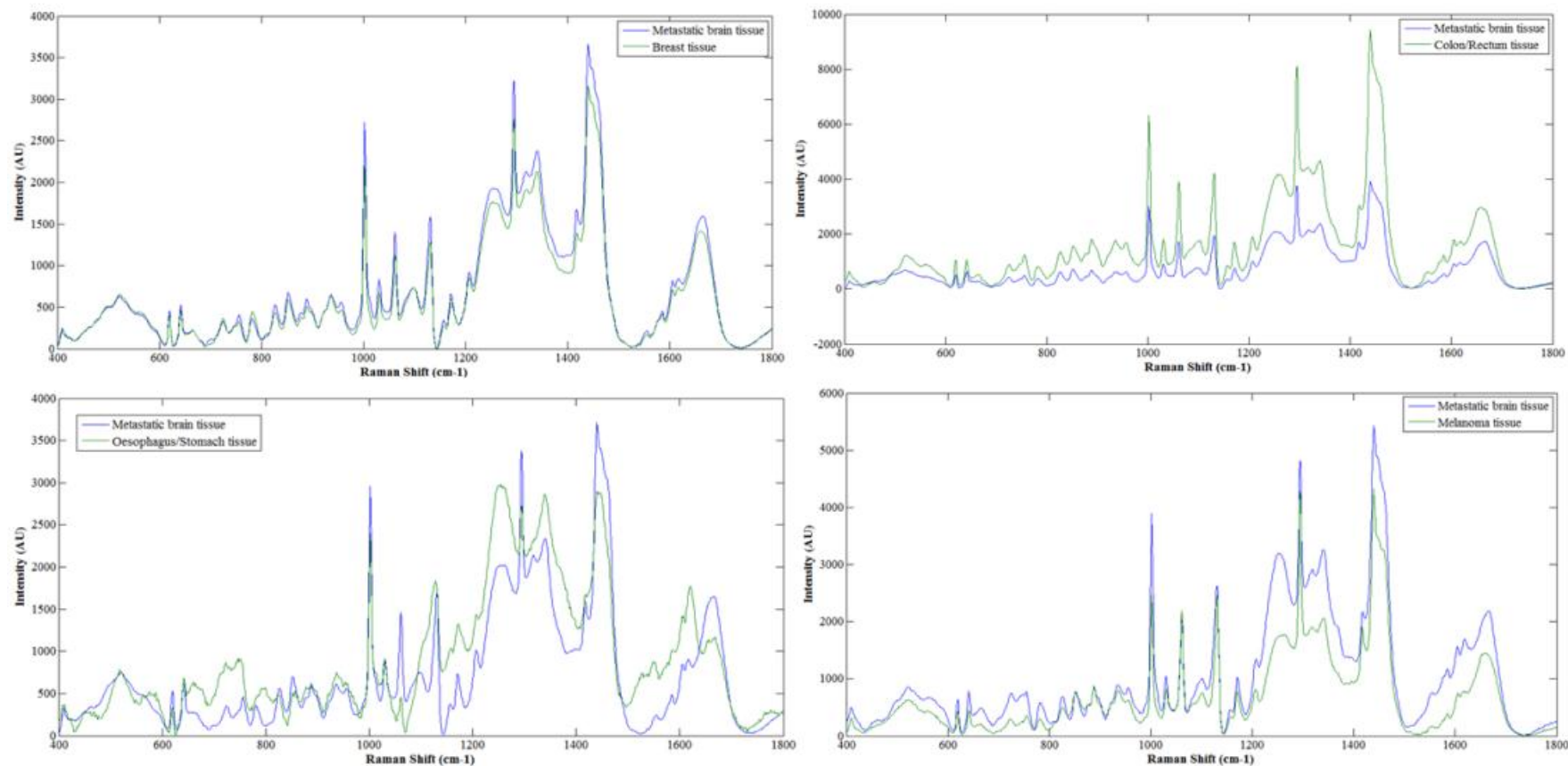


Figure 30 Original spectral plot of averaged 95 primary breast acquisitions ($n=5$) and 96 breast met acquisitions ($n=5$) (top left), 22 primary colon acquisitions ($n=1$) and 22 metastatic colon/rectum acquisitions ($n=1$) (top right), 22 primary oesophagus & stomach acquisitions ($n=1$) and 22 oesophagus & stomach met acquisitions ($n=1$) (bottom left) and 25 primary melanoma acquisitions ($n=1$) and 20 melanoma met acquisitions ($n=1$) (bottom right). The spectra have been vector normalised, baseline corrected by 5th order polynomial fit and subtraction, and 7 points of smoothing.

Chapter 4

Conclusions

Through assessments, comparing the 785 nm laser line to the 532 nm laser line and Raman spectroscopy to immersion Raman spectroscopy, the techniques and settings used for spectral histopathological analysis were tailored to optimise the quality of the results generated in the study. It is observed in this study that immersion Raman spectroscopy employing a 785 nm laser generated spectra of better overall quality, with higher signal-to-noise ratios. Hence, these methods and settings were used for further investigation into the diagnostic capabilities of Raman spectroscopy.

In this study, the use of immersion Raman spectroscopy to differentiate between GBM, metastatic and normal brain tissue has been demonstrated using peak ratios, with sensitivities and specificities of 100% and 94.44%, respectively for GBM, 96.55% and 100%, respectively for metastatic brain, and 85.71% and 100%, respectively for normal brain tissue. The potential of immersion Raman spectroscopy to identify the origin site of the primary cancer from the analysis of brain metastases has also been observed through the PC-DFA model which shows separation of different metastatic brain tissue spectra based on their location for breast, lung, melanoma, colon/rectum and oesophagus and stomach. From analysis this study has identified spectral differences between GBM, metastatic and normal brain tissues and highlighted the main alterations to be attributed to the choline peak at 721 cm^{-1} , present in GBM and absent in both metastatic and normal brain, and the nucleotide peak at 782 cm^{-1} present in metastatic and GBM and absent in normal brain. The ratios of these peaks were significantly different between the spectra of the different histopathological groups enabling segregation of the various tissue types. PC-DFA on the data produced sensitivities and

specificities for GBM classification of up to 95.24% and 72.63%, respectively. For metastatic classification of up to 95.47% and 90.43% were calculated, respectively. For normal brain classification of up to 90.38% and 78.41% were calculated, respectively. This analysis used the spectra across the full wavelength range that was analysed. This further shows that the spectra, from 400 cm^{-1} to 1800 cm^{-1} , of metastatic, GBM and normal brain tissue are distinguishable from each other and can potentially be used to diagnose cancerous tissue.

However, this study is based on the assumption that histopathology, employed in this study to diagnose the tissue specimens, has identified all the samples and their primary sites of origin correctly.

This study also shows the influence that Raman substrates have on sample preparation and the resulting spectra. Spectral backgrounds of the substrates show that the baseline of low-E is the highest and CaF_2 the lowest of the three substrates. It has been observed that the tissue specimens on the CaF_2 and Spectrosil substrates exhibit paraffin peaks in their spectra whereas the tissue specimens on the low-E substrates do not. Throughout this investigation it has been established that CaF_2 and Spectrosil substrates retain paraffin wax residuals after the dewaxing procedure was carried out, whereas low-E did not. This was attributed to the difference in surface morphology of the substrates causing a variation in the retention of paraffin wax. AFM of the three substrate types shows that low-E is smoother than either CaF_2 or Spectrosil and thus must dispel wax more easily.

It was also noted that the spectra of metastatic tissue had much larger paraffin peaks present than the spectra of GBM tissue and that normal tissue spectra had an even

smaller paraffin contribution than that of GBM. This has been attributed to the change of tissue density between normal tissue and cancerous tissue. The denser cancerous tissue seems to have an increased ability to retain paraffin wax than the less dense, normal tissue.

Overall, this study has shown the successful use of immersion Raman spectroscopy as a diagnostic clinical tool for cancer and its potential for primary cancer origin site identification. This study has also presented the substantial influence substrate material has on tissue preparation methods and the outcome of spectra.

Chapter 5

Future Work

There are many future studies that could be of interest and benefit to the advancement of this area of cancer research and other related areas. The spectral differences between normal brain, metastatic brain and GBM tissues need to be further investigated to ascertain the relevance of immersion Raman spectroscopy as a diagnostic technique and assess its potential use in clinical settings. The analysis of a larger sample size and wider variety of metastatic cancer types from different primary locations would be of benefit and improve the reliability of the results. Other primary tumours of the brain could also be studied to analyse the spectral differences between these tumours and metastatic lesions, and the ability to stage tumours based on their spectral signatures. Such studies could lead to the identification of particular characteristic peaks or spectral patterns capable of acting as biomarkers for metastatic brain cancer.

A study more closely designed for *in vivo* use of the technique is essential to assess the clinical relevance of Raman spectroscopy. Such studies could utilise deep Raman techniques and fibre optics.

A study could also be carried out to further identify the spectral differences between metastatic brain cancer and their corresponding primary cancers to ascertain a greater understanding of the biomolecular changes that incur between primary cancers and resulting metastases in the brain and possibly other organs where metastases frequently form.

A further investigation into the identification of primary sites from metastases is needed. This should be carried out on a variety of metastatic tissue, not just brain, in order to analyse significant spectral trends that could accurately diagnose the primary cancers from metastatic tissues.

A study is required to further ascertain the effects spectroscopic substrates and tissues of different histology have on the dewaxing process of tissue samples and the outcome of Raman spectra. This should be carried out in order to optimise Raman spectroscopy and tissue preparation techniques for future work in the field of bio-spectroscopy.

Bibliography

1. Cancer Research UK. *All cancers combined key facts*. (2012) [15/04/2013]; Available from: <http://www.cancerresearchuk.org/cancer-info/cancerstats/keyfacts/Allcancerscombined/>.
2. Louis, D.N., H. Ohgaki, O. D. Wiestler and W. K. Cavenee, (2007) *World Health Organisation Classification of Tumours : WHO Classification of Tumours of the Central Nervous System* 4th ed. Geneva, CHE: World Health Organisation: p. 248-251.
3. Richards, G.M., D. Khuntia, and M.P. Mehta, (2007) Therapeutic management of metastatic brain tumors. *Critical Reviews in Oncology/Hematology*. **61**(1): p. 70-78.
4. Brain Research Trust. *About Brain Tumours*. [cited 08/10/2012]; Available from: <http://www.brt.org.uk/brain-tumours>.
5. Soffieti, R., P. Cornu, J. Y. Delattre, R. Grant, F. Graus, W. Grisold, J. Heimans, J. Hildebrand, P. Hoskin, M. Kallijo, P. Krauseneck, C. Marosi, T. Siegal and C. Vecht, (2011) Brain Metastases. *European Handbook of Neurological Managments, 2nd ed. (eds: N. E. Gilhus, M. P. Barnes and M. Brainin)*. **1**: p. 437-445.
6. Bergner, N., B. F. M. Romeike, R. Reichart, R. Kalff, C. Krafft and J. Popp, (2011) *Raman and FTIR Microspectroscopy for Detection of Brain Metastasis*. Optical Society of America.
7. Hengel, K., G. Sidhu, J. Choi, J. Weedon, E. Nwokedi, C. Axiotis, X. Song, and A. Braverman (2013), Attributes of brain metastases from breast and lung cancer. *International Journal of Clinical Oncology*, **18** (3): p. 396-401.
8. Peacock, K. and G. Lesser, (2006) Current therapeutic approaches in patients with brain metastases. *Current Treatment Options in Oncology*. **7**(6): p. 479-489.
9. Wen, P. and J. Loeffler, Brain metastases. *Current Treatment Options in Oncology*, 2000. **1**(5): p. 447-457.
10. Vincent, T.L. and R.A. Gatenby, (2008) An evolutionary model for initiation, promotion, and progression in carcinogenesis. *International Journal of Oncology*. **32**(4): p. 729-37.
11. Tannock, I.F., R.P. Hill, R.G. Bristow, and L. Harrington, *The Basic Science of Oncology*. 4th ed. 2005, USA: The McGraw-Hill Companies, Inc.
12. Weston, A., C. Curtis and M.D. Harris, (2000) *Chapter 12: Chemical Carcinogenesis. In: Bast, R.C. Jr., D.W. Kufe and R.E. Pollock, et al., editors. Holland-Frei Cancer Medicine*. Hamilton (ON): BC Decker.
13. Moon, Y.J., X. Wang, and M.E. Morris, (2006) Dietary flavonoids: Effects on xenobiotic and carcinogen metabolism. *Toxicology in Vitro*. **20**(2): p. 187-210.
14. Andreeff, M., D.W. Goodrich, and A.B. Pardee, (2000) *Chapter 2: Cell proliferation, differentiation, and apoptosis*. 5th ed. Holland-Frei Cancer Medicine, ed. R.C.J. Bast, D.W. Kufe, and R.E. Pollock. Hamilton (ON): BC Decker.
15. Weinberg, R.A., (2007) *The biology of Cancer*. USA: Garland Science, Taylor and Francis Group, LLC.
16. Mahadevan-Jansen, A. and R.R. Richards-Kortum, (1996) Raman spectroscopy for the detection of cancers and precancers. *Journal of Biomedical Optics*. **1**(1): p. 31-70.
17. Bower, M. and J. Waxman, (20011) *Lecture Notes: Oncology*. 2nd ed. USA: Wiley-Blackwell.
18. Polyzoidis, K.S., G. Miliaras, and N. Pavlidis, (2005) Brain metastasis of unknown primary: A diagnostic and therapeutic dilemma. *Cancer Treatment Reviews*. **31**(4): p. 247-255.
19. Fidler, I.J., (2003) The pathogenesis of cancer metastasis: the 'seed and soil' hypothesis revisited. *Nature Reviews Cancer*. **3**(6): p. 453-458.
20. Nowell, P.C., (1976) The clonal evolution of tumour cell populations. *Science*. **194**: p. 23-28.

21. Mueller, W.C., Y. Spector, T.B. Edmonston, B. St Cyr, D. Jaeger, U. Lass, R. Aharonov, S. Rosenwald, and A. Chajut, (2011) Accurate classification of metastatic brain tumors using a novel microRNA-based test. *Oncologist*. **16**(2): p. 165-74.
22. Kim, D.G. and L.D. Lunsford, (2012) *Current and Future Management of Brain Metastasis*. Progress in Neurological Surgery. Vol. 25, Basel: Karger.
23. Ellis, D.I., and R. Goodacre, (2006) Metabolic fingerprinting in disease diagnosis: biomedical applications of infrared and Raman spectroscopy. *Analyst*. **131**: p. 875-885.
24. Zarandi, M.H.F., M. Zarinbal, and M. Izadi, (2011) Systematic image processing for diagnosing brain tumors: A Type-II fuzzy expert system approach. *Applied Soft Computing*. **11**(1): p. 285-294.
25. Santra, A.R.K., P. Sharma, C. Bal, A. Kumar, P. K. Julka and A. Malhotra, (2012) F-18 FDG PET-CT in patients with recurrent glioma: Comparison with contrast enhanced MRI. *European Journal of Radiology*. **81**(3): p. 508-513.
26. Campos, S., P. Davey, A. Hird, B. Pressnail, J. Bilbao, R.I. Aviv, S. Symons, F. Pirouzmand, E. Sinclair, S. Culleton, E. Desa, P. Goh, and E. Chow, (2009) Brain metastasis from an unknown primary, or primary brain tumour? A diagnostic dilemma. *Current Oncology*. **16**(1): p. 62-6.
27. Diamandis, E.P., (2004) Mass spectrometry as a diagnostic and a cancer biomarker discovery tool: opportunities and potential limitations. *Molecular and Cellular Proteomics*. **3**(4): p. 367-78.
28. Gurcan, M.N., L.E. Boucheron, A. Can, A. Madabhushi, N.M. Rajpoot, and B. Yener, (2009) Histopathological image analysis: a review. *IEEE Reviews in Biomedical Engineering*. **2**: p. 147-71.
29. Krafft, C., S.B. Sobottka, G. Schackert, and R. Salzer, (2004) Analysis of human brain tissue, brain tumors and tumor cells by infrared spectroscopic mapping. *Analyst*. **129**(10): p. 921-925.
30. Zhou, Y., C.H. Liu, Y. Sun, Y. Pu, S. Boydston-White, Y. Liu, and R.R. Alfano, (2012) Human brain cancer studied by resonance Raman spectroscopy. *Journal of Biomedical Optics*. **17**(11): p. 116021.
31. Raab, S.S., R.E. Nakhleh, and S.G. Ruby, (2005) Patient Safety in Anatomic Pathology: Measuring Discrepancy Frequencies and Causes. *Archives of Pathology & Laboratory Medicine*. **129**(4): p. 459-466.
32. Raab, S.S., D.M. Grzybicki, J.E. Janosky, R.J. Zarbo, F.A. Meier, C. Jensen, and S.J. Geyer, (2005) Clinical impact and frequency of anatomic pathology errors in cancer diagnoses. *Cancer*. **104**(10): p. 2205-13.
33. Stone, N., C. Kendall, J. Smith, P. Crow, and H. Barr, (2004) Raman Spectroscopy for identification of epithelial cancers. *Faraday Discussions*. **126**: p. 141-157.
34. Krafft, C., L. Shapoval, S.B. Sobottka, K.D. Geiger, G. Schackert, and R. Salzer, (2006) Identification of primary tumors of brain metastases by SIMCA classification of IR spectroscopic images. *Biochimica et Biophysica Acta (BBA) - Biomembranes*. **1758**(7): p. 883-891.
35. Banwell, C.N. and E.M. McCash, (1994) *Fundamentals of Molecular Spectroscopy* 4th ed., UK: McGraw-Hill International Limited.
36. Skoog, D.A., F.J. Holler and S.R. Crouch, (2007) *Principles of Instrumental Analysis*. 6th ed., USA: Thompson Brooks/Cole.
37. Tu, Q. and C. Chang, (2012) Diagnostic applications of Raman spectroscopy. *Nanomedicine*. **8**(5): p. 545-58.
38. Wagner, M., (2009) Single-cell ecophysiology of microbes as revealed by Raman microspectroscopy or secondary ion mass spectrometry imaging. *Annual Reviews of Microbiology*. **63**: p. 411-29.
39. Das, R.S. and Y.K. Agrawal, (2011) Raman spectroscopy: Recent advancements, techniques and applications. *Vibrational Spectroscopy*. **57**(2): p. 163-176.

40. Auner, A.W., R.E. Kast, R. Rabah, J.M. Poulik, and M.D. Klein (2013), Conclusions and data analysis: a 6-year study of Raman spectroscopy of solid tumors at a major pediatric institute. *Pediatric Surgery International*, **29**(2): p. 129-140.
41. Devpura, S., J.S. Thakur, F.H. Sarkar, W.A. Sakr, V.M. Naik and R. Naik, (2010) Detection of benign epithelia, prostatic intraepithelial neoplasia, and cancer regions in radical prostatectomy tissues using Raman spectroscopy. *Vibrational Spectroscopy*. **53**(2): p. 227-232.
42. Kawabata, T., H. Kikuchi, S. Okazaki, M. Yamamoto, Y. Hiramatsu, J. Yang, M. Baba, M. Ohta, K. Kamiya, T. Tanaka, and H. Konno, (2011) Near-Infrared Multichannel Raman Spectroscopy with a 1064 nm Excitation Wavelength for Ex Vivo Diagnosis of Gastric Cancer. *Journal of Surgical Research*. **169**(2): p. e137-e143.
43. Wartewig, S. and R.H.H. Neubert, (2005) Pharmaceutical applications of Mid-IR and Raman spectroscopy. *Advanced Drug Delivery Reviews*. **57**(8): p. 1144-1170.
44. Moros, J., S. Garrigues, and M. de la Guardia, (2010) Vibrational spectroscopy provides a green tool for multi-component analysis. *TrAC Trends in Analytical Chemistry*. **29**(7): p. 578-591.
45. Krishna, C.M., G.D. Sockalingum, G. Kegelaer, S. Rubin, V.B. Kartha, and M. Manfait, (2005) Micro-Raman spectroscopy of mixed cancer cell populations. *Vibrational Spectroscopy*. **38**(1-2): p. 95-100.
46. Krafft, C., M. Kirsch, C. Beleites, G. Schackert and R. Salzer, (2007) Methodology for fiber-optic Raman mapping and FTIR imaging of metastases in mouse brains. *Analytical and Bioanalytical Chemistry*. **389**(4): p. 1133-1142.
47. Brożek-Pluska, B., I. Placek, K. Kurczewski, Z. Morawiec, M. Tazbir, and H. Abramczyk, (2008) Breast cancer diagnostics by Raman spectroscopy. *Journal of Molecular Liquids*. **141**(3): p. 145-148.
48. Matousek, P., E.R.C. Draper, A.E. Goodship, I.P. Clark, K.L. Ronayne, and A.W. Parker, (2006) Noninvasive Raman Spectroscopy of Human Tissue In Vivo. *Applied spectroscopy*. **60**(7): p. 758-763.
49. Patel, I.I., J. Trevisan, G. Evans, V. Llabjani, P.L. Martin-Hirsch, H.F. Stringfellow, and F.L. Martin, (2011) High contrast images of uterine tissue derived using Raman microspectroscopy with the empty modelling approach of multivariate curve resolution-alternating least squares. *Analyst*. **136**(23): p. 4950-4959.
50. Nijssen, A., T.C. Bakker Schut, F. Heule, P.J. Caspers, D.P. Hayes, M.H. Neumann, and G.J. Puppels, (2002) Discriminating basal cell carcinoma from its surrounding tissue by Raman spectroscopy. *J Invest Dermatol*. **119**(1): p. 64-69.
51. Kirsch, M., G. Schackert, R. Salzer, and C. Krafft, (2010) Raman spectroscopic imaging for in vivo detection of cerebral brain metastases. *Analytical and Bioanalytical Chemistry*. **398**(4): p. 1707-1713.
52. Choo-Smith, L.P., H.G.M. Edwards, H.P. Endtz, J.M. Kros, F. Heule, H. Barr, J.S. Robinson, H.A. Bruining, and G.J. Puppels, (2002) Medical applications of Raman spectroscopy: From proof of principle to clinical implementation. *Biopolymers*. **67**(1): p. 1-9.
53. Krafft, C., S.B. Sobottka, G. Schackert, and R. Salzer, (2005) Near infrared Raman spectroscopic mapping of native brain tissue and intracranial tumors. *Analyst*. **130**(7): p. 1070-1077.
54. Stone, N., P. Stavroulaki, C. Kendall, M. Birchall, and H. Barr, (2000) Raman spectroscopy for early detection of laryngeal malignancy: preliminary results. *Laryngoscope*. **110**(10 Pt 1): p. 1756-1763.
55. Bonnier, F., A. Mehmood, P. Knief, A.D. Meade, W. Hornebeck, H. Lambkin, K. Flynn, V. McDonagh, C. Healy, T.C. Lee, F.M. Lyng, and H.J. Byrne, (2011) In vitro analysis of immersed human tissues by Raman microspectroscopy. *Journal of Raman Spectroscopy*. **42**(5): p. 888-896.

56. Bonnier, F., S.M. Ali, P. Knief, H. Lambkin, K. Flynn, V. McDonagh, C. Healy, T.C. Lee, F.M. Lyng, and H.J. Byrne, (2012) Analysis of human skin tissue by Raman microspectroscopy: Dealing with the background. *Vibrational Spectroscopy*. **61**(0): p. 124-132.
57. Bonnier, F., A.D. Meade, S. Merzha, P. Knief, K. Bhattacharya, F.M. Lyng, and H.J. Byrne, (2010) Three dimensional collagen gels as a cell culture matrix for the study of live cells by Raman spectroscopy. *Analyst*. **135**(7): p. 1697-703.
58. Gajjar, K., L. D. Heppenstall, W. Pang, K. M. Ashton, J. Trevisan, I. I. Patel, V. Llabjani, H. F. Stringfellow, P. L. Martin-Hirsch, T. Dawson and F. L. Martin, (2013) Diagnostic segregation of human brain tumours using Fourier-transform infrared and/or Raman spectroscopy coupled with discriminant analysis. *Analytical Methods*. **5**: p. 89-102.
59. Krafft, C., S.B. Sobottka, G. Schackert, and R. Salzer, (2006) Raman and infrared spectroscopic mapping of human primary intracranial tumors: a comparative study. *Journal of Raman Spectroscopy*. **37**(1-3): p. 367-375.
60. Huang, Z., A. McWilliams, H. Lui, D. I. McLean, S. Lam and H. Zeng, (2013) Near-infrared Raman spectroscopy for optical diagnosis of lung cancer. *International Journal of Cancer*. **107**(6): p. 1047-1052.
61. Teh, S.K., W. Zheng, K.Y. Ho, M. Teh, K.G. Yeoh, and Z. Huang, (2010) Near-infrared Raman spectroscopy for early diagnosis and typing of adenocarcinoma in the stomach. *British Journal of Surgery*. **97**(4): p. 550-557.
62. Bergholt, M.S., W. Zheng, K. Lin, K.Y. Ho, M. Teh, K.G. Yeoh, J.B. Yan So, and Z. Huang, (2011) In vivo diagnosis of gastric cancer using Raman endoscopy and ant colony optimization techniques. *International Journal of Cancer*. **128**(11): p. 2673-2680.
63. Lieber, C.A., S.K. Majumder, D.L. Ellis, D.D. Billheimer, and A. Mahadevan-Jansen, (2008) In vivo nonmelanoma skin cancer diagnosis using Raman microspectroscopy. *Lasers in Surgery and Medicine*. **40**(7): p. 461-467.
64. Lin, K., D.L.P. Cheng, and Z. Huang, (2012) Optical diagnosis of laryngeal cancer using high wavenumber Raman spectroscopy. *Biosensors and Bioelectronics*. **35**(1): p. 213-217.
65. Abramczyk, H., J. Surmacki, B. Brożek-Płuska, Z. Morawiec, and M. Tazbir, (2009) The hallmarks of breast cancer by Raman spectroscopy. *Journal of Molecular Structure*. **924–926**: p. 175-182.
66. Moreno, M., L. Raniero, E.A.L. Arisawa, A.M. do Espirito Santo, E.A.P. dos Santos, R.A. Bitar, and A.A. Martin, (2010) Raman spectroscopy study of breast disease. *Theoretical Chemistry Accounts*. **125**: p. 329-334.
67. Kanter, E.M., E. Vargis, S. Majumder, M.D. Keller, E. Woeste, G.G. Rao, and A. Mahadevan-Jansen, (2009) Application of Raman spectroscopy for cervical dysplasia diagnosis. *Journal of Biophotonics*. **2**(1-2): p. 81-90.
68. Crow, P., A. Molckovsky, N. Stone, J. Uff, B. Wilson, and L.M. WongKeeSong, (2005) Assessment of fiberoptic near-infrared raman spectroscopy for diagnosis of bladder and prostate cancer. *Urology*. **65**(6): p. 1126-1130.
69. Tollefson, M., J. Magera, T. Sebo, J. Cohen, A. Drauch, J. Maier, and I. Frank, (2010) Raman spectral imaging of prostate cancer: can Raman molecular imaging be used to augment standard histopathology? *British Journal of Urology International*. **106**(4): p. 484-488.
70. Manoharan, R., Y. Wang, and M.S. Feld, (1996) Histochemical analysis of biological tissues using Raman spectroscopy. *Spectrochimica Acta Part A: Molecular and Biomolecular Spectroscopy*. **52**(2): p. 215-249.
71. Shetty, G., C. Kendall, N. Shepherd, N. Stone, and H. Barr, (2006) Raman spectroscopy: elucidation of biochemical changes in carcinogenesis of oesophagus. *British Journal of Cancer*. **94**(10): p. 1460-1464.

72. Bocklitz, T., A. Walter, K. Hartmann, P. Rosch, and J. Popp, (2011) How to pre-process Raman spectra for reliable and stable models? *Analytica Chimica Acta*. **704**(1-2): p. 47-56.
73. Bassan, P., A. Sachdeva, J. Lee, and P. Gardner, (2013) Substrate contributions in micro-ATR of thin samples: implications for analysis of cells, tissue and biological fluids. *Analyst*. **138**(14): p. 4139-4146.
74. Draux, F., P. Jeannesson, A. Beljebbar, A. Tfayli, N. Fourre, M. Manfait, J. Sule-Suso, and G.D. Sockalingum, (2009) Raman spectral imaging of single living cancer cells: a preliminary study. *Analyst*. **134**(3): p. 542-548.
75. Ali, S.M., F. Bonnier, A. Tfayli, H. Lambkin, K. Flynn, V. McDonagh, C. Healy, T. Clive Lee, F.M. Lyng, and H.J. Byrne, (2013) Raman spectroscopic analysis of human skin tissue sections ex-vivo: evaluation of the effects of tissue processing and dewaxing. *J Biomed Opt*. **18**(6): p. 061202.
76. Ó Faoláin, E., M. Hunter, J. Byrne, P. Kelehan, M. McNamara, H. Byrne and F. Lyng, (2005) A study examining the effects of tissue processing on human tissue sections using vibrational spectroscopy. *Materials Synthesis and Applications, Dublin Institute of Technology*. **38**: p. 121-127.
77. Trunova, V., A. Sidorina, V. Zvereva, and B. Churin, (2013) Changes in the elemental content of rat heart as a result of the fixation in formalin analyzed by synchrotron radiation X-ray fluorescent analysis. *Journal of Trace Elements and Medicine and Biology*. **27**(1): p. 76-77.
78. Huang, Z., A. McWilliams, S. Lam, J. English, D.I. McLean, H. Lui, and H. Zeng, (2003) Effect of formalin fixation on the near-infrared Raman spectroscopy of normal and cancerous human bronchial tissues. *International Journal of Oncology*. **23**(3): p. 649-655.
79. Ó Faoláin, E., M.B. Hunter, J.M. Byrne, P. Kelehan, H.A. Lambkin, H.J. Byrne, and F.M. Lyng, (2005) Raman spectroscopic evaluation of efficacy of current paraffin wax section dewaxing agents. *Journal of Histochemistry and Cytochemistry*. **53**(1): p. 121-129.
80. Gobinet, C., D. Seiskveradze, V. Vrabie, A. Tfayli, O. Piot and M. Manfait, (2008) Digital dewaxing of Raman spectral images of paraffin-embedded human skin biopsies based in ICA and NCLS. *16th European Signal Processing Conference (EUSIPCO)*.
81. Egerton, R.F., (2010) *Physical Principles of Electron Microscopy, An introduction to TEM, SEM and AEM*. US: Springer Science+Business Media, Inc.
82. Museum of Science: Boston. *How the SEM Works*. (1996) [03/09/2013]; Available from: <http://legacy.mos.org/sln/sem/tour01.html>.
83. The Field Museum. *SEM/EDS*. (2013) [03/09/2013]; Available from: <http://fieldmuseum.org/explore/departments/conserving-collections/examination-documentation/sem-eds>.
84. University of California. *Introduction to Energy Dispersive X-ray Spectrometry (EDS)*. [06/09/2013]; Available from: <http://micron.ucr.edu/public/manuals/EDS-intro.pdf>.
85. Fenn, M.B., P. Xanthopoulos, G. Pyrgiotakis, S.R. Grobmyer, P.M. Pardalos, and L.L. Hench, (2011) Raman Spectroscopy for Clinical Oncology. *Advances in Optical Technologies*. **2011**: p. 1-20.
86. Randolph, T.W., (2006) Scale-based normalization of spectral data. *Cancer Biomark*. **2**(3-4): p. 135-144.
87. Baker, M.J., E. Gazi, M.D. Brown, J.H. Shanks, P. Gardner, and N.W. Clarke, (2008) FTIR-based spectroscopic analysis in the identification of clinically aggressive prostate cancer. *British Journal of Cancer*. **99**(11): p. 1859-1866.
88. Akobeng, A.K., (2007) Understanding diagnostic tests 1: sensitivity, specificity and predictive values. *Acta Paediatrica*. **96**(3): p. 338-341.
89. Hands, J.R., P. Abel, K. Ashton, T. Dawson, C. Davis, R. Lea, A. McIntosh, and M. Baker, (2013) Investigating the rapid diagnosis of gliomas from serum samples using infrared

- spectroscopy and cytokine and angiogenesis factors. *Analytical and Bioanalytical Chemistry*, **405**(23): p. 7347-7355.
90. Huang, Z., X. Chen, Y. Chen, J. Chen, M. Dou, S. Feng, H. Zeng, and R. Chen, (2011) Raman spectroscopic characterization and differentiation of seminal plasma. *Journal of Biomedical Optics*. **16**(11): p. 110501-110501.
 91. Sikirzhyski, V., K. Virkler, and I.K. Lednev, Discriminant analysis of Raman spectra for body fluid identification for forensic purposes. *Sensors (Basel)*, 2010. **10**(4): p. 2869-84.
 92. Chan, J.W., D.S. Taylor, T. Zwerdling, S.M. Lane, K. Ihara, and T. Huser, (2006) Micro-Raman spectroscopy detects individual neoplastic and normal hematopoietic cells. *Biophysical Journal*. **90**(2): p. 648-656.
 93. Feng, S., R. Chen, J. Lin, J. Pan, G. Chen, Y. Li, M. Cheng, Z. Huang, J. Chen, and H. Zeng, (2010) Nasopharyngeal cancer detection based on blood plasma surface-enhanced Raman spectroscopy and multivariate analysis. *Biosensors and Bioelectronics*. **25**(11): p. 2414-2419.
 94. Tan, C.H. and E.H. Tan, (2012) Post-treatment Assessment of Glioblastoma Multiforme: Imaging with Fluorodeoxyglucose, Sestamibi, and Choline. *World Journal of Nuclear Medicine*. **11**(1): p. 30-32.
 95. Al-Okaili, R.N., J. Krejza, S. Wang, J.H. Woo, and E.R. Melhem, (2006) Advanced MR imaging techniques in the diagnosis of intraaxial brain tumors in adults. *Radiographics*. **26 Suppl 1**: p. S173-189.
 96. Haka, A.S., K. E. Shafer-Peltier, M. Fitzmaurice, J. Crowe, R. R. Dasari and M. S. Feld, (2005) Diagnosing breast cancer by using Raman spectroscopy. *Proceedings of the National Academy of Sciences*. **102**(35): p. 12371-12376.
 97. Boyd, N.F., G.A. Lockwood, J.W. Byng, D.L. Tritchler, and M.J. Yaffe, (1998) Mammographic densities and breast cancer risk. *Cancer Epidemiology, Biomarkers and Prevention*. **7**: p. 1133-1144.
 98. Gniadecka, M., P.A. Philipsen, S. Sigurdsson, S. Wessel, O.F. Nielsen, D.H. Christensen, J. Hercogova, K. Rossen, H.K. Thomsen, R. Gniadecki, L.K. Hansen, and H.C. Wulf, (2004) Melanoma Diagnosis by Raman Spectroscopy and Neural Networks: Structure Alterations in Proteins and Lipids in Intact Cancer Tissue. *Journal of Investigative Dermatology*. **122**(2): p. 443-449.
 99. Li, L., Z. Wu, L. Chen, F. George, Z. Chen, A. Salem, M. Kallergi, and C. Berman, (2005) Breast Tissue Density and CAD Cancer Detection in Digital Mammography. *Conference Proceedings IEEE Engineering in Medicine and Biology Society*. **3**: p. 3253-3256.

Appendices

Appendix 1 – Poster submitted to the 7th International Conference on Advanced Vibrational Spectroscopy held in Kobe, Japan.

P-142

Investigating Immersion and Non-Immersion Raman Spectroscopy to Identify Primary Sites of Origin in Metastatic Brain Cancer

Leanne M. Fullwood¹, Dave Griffiths², Katherine Ashton³, Timothy Dawson³, Robert W. Lea², Charles Davis³, Franck Bonnier⁴, Hugh Byrne⁴, and Matthew J. Baker^{1*}

¹Centre for Materials Science, Division of Chemistry, University of Central Lancashire, Preston, PR1 2HE, UK

²School of Pharmacy and Biomedical Sciences, University of Central Lancashire, Preston, PR1 2HE, UK

³Royal Preston Hospital, Sharoe Green Lane, Fulwood, Preston PR2 9HT, UK

⁴FOCAS research Institute, Dublin Institute of Technology, Kevin Street, Dublin 8, Ireland

*email: MJBaker@uclan.ac.uk

Aim: To evaluate the use of Raman spectroscopy as a diagnostic tool for metastatic brain cancer and assess its ability to identify primary sites of origin.

Materials and methods

Tissue samples

> Tissue samples (Table 1) were obtained from the Brain Tumour North West bio bank from a total of 48 patients (Ethical Approval: BTNW/WRIB 13_01)

> Each tissue sample was sectioned at 10 µm onto three different Raman substrates: low-E MiriR (Kevley Technologies, Chesterland, OH, 44026, USA), Spectrosil quartz (Starna Scientific) and calcium fluoride (CaF₂) (Crystan).

Table 1. Tissue sample collection.

Sample type	No. of Samples
Normal	7
GBM	5
Metastatic brain (n=29)	
Lung	8
Breast	6
Melanoma	5
Colon/Rectal	6
Oesophagus/Stomach	4
Primary (n=7)	
Breast	4
Melanoma	1
Colon/Rectal	1
Oesophagus/Stomach	1

Tissue Dewaxing

> The tissue blocks used were formalin fixed-paraffin embedded for preservation. Thus, dewaxing was carried out prior to spectroscopic analysis to reduce spectral contributions from the paraffin wax.

> Dewaxing Procedure: 3, 5 minute baths of HistoClear followed by 3, 5 minute baths of ethanol. The tissue sections were then left to air-dry and stored in a desiccator until Raman analysis took place.

Raman Spectroscopy

> Spectroscopic measurements were carried out on a Horiba Jobin-Yvon LabRAM HR800 spectrometer using a 785 nm laser source.

> Spectra were acquired for 30 s and accumulated twice. At least 20 spectra were taken per sample.

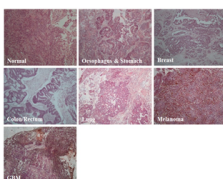


Figure 1 Microscopic images of H&E stained tissue samples of normal, metastatic (from oesophagus and stomach, breast, colon/rectum, lung and melanoma as labelled above) and GBM brain WHO grade IV (n=100).

Substrate Study

> Raman spectra were generated of the substrate backgrounds which showed that CaF₂ produces a lower intensity background than Spectrosil and low-E substrates (Figure 2).

> Paraffin peaks were present, in the tissue spectra on Spectrosil and CaF₂, shown by the asterisks above the corresponding peaks in Figure 2, yet absent in the spectra produced from the low-E substrate.

> Paraffin sections were mounted onto the three substrates and dewaxed using the same method as the tissue sections. Figure 3 shows microscopic images of residual wax present on CaF₂ and Spectrosil but not on low-E. Spectra taken from the substrates further confirm paraffin's presence on CaF₂ and Spectrosil and absence on low-E.

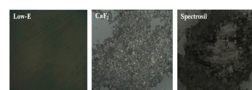


Figure 3 Microscopic images of the three substrates (Low-E, CaF₂, Spectrosil) after dewaxing. Wax residues can be observed on the CaF₂ and Spectrosil substrates.

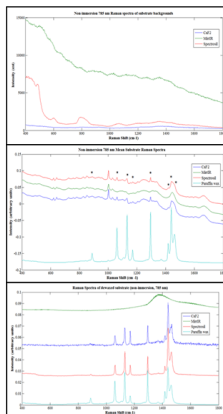


Figure 2 Raman spectra of the three substrates (Low-E, CaF₂, Spectrosil) showing the effect of dewaxing. The spectra show peaks at 1450 and 1470 cm⁻¹, which are significantly reduced in intensity after dewaxing.

Results

Spectral differences are observable between metastatic, GBM and normal brain tissue spectra (Figure 4).

> The intensity of the 782 cm⁻¹ peak is dramatically lower in normal brain tissue spectra than in GBM and metastatic.

> GBM spectra exhibit a 721 cm⁻¹ peak yet normal and metastatic do not, but exhibit a 725 cm⁻¹ instead.

> PC-DFA shows discrimination between GBM, normal and metastatic spectra. Table 2 displays the resulting sensitivities and specificities.

> A ratio score plot (Figure 5) was produced based on discriminatory spectral peaks and used as a model to produce sensitivities and specificities (Table 3).

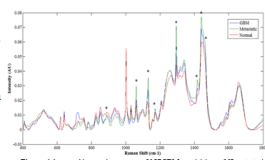


Figure 4 Averaged Raman spectra of 127 GBM acquisitions, 688 metastatic acquisitions and 157 normal brain acquisitions. Spectra have been vector normalised, the backgrounds have been corrected using a 5th order polynomial fit and subtracted and 7 points of smoothing. The asterisks correspond to paraffin peaks from residual wax in the tissue.

Table 2 PC-DFA model details, including spectral member and the sensitivities and specificities.

	Train spectra	Test spectra	Confidence level	Histopathological type	Sensitivity (%)	Specificity (%)
GBM	659	316	90%	GBM	92.86	72.63
vs. norm				Normal	88.46	78.41
				Metastatic	91.82	90.43
vs. met			95%	GBM	91.24	36.13
				Normal	90.38	56.82
				Metastatic	95.47	81.05

Table 3 Sensitivities and specificities of GBM classification based on the 721 cm⁻¹ to 620 cm⁻¹ ratio data above 1, metastatic classification based on the 721 cm⁻¹ to 620 cm⁻¹ ratio data below 1 and 620 cm⁻¹ to 782 cm⁻¹ ratio data below 1 and normal brain based on the 721 cm⁻¹ to 620 cm⁻¹ ratio data below 1 and 620 cm⁻¹ to 782 cm⁻¹ ratio data above 5.

Histopathological type	Sensitivity (%)	Specificity (%)
GBM	100	94.44
Normal	85.71	100
Metastatic	96.55	100

> PC-DFA of the metastatic tissue and the primary sites show that spectra generally group together in their histopathological type (Figure 6 and 7). However, primary tissue specimens have a much better level of classification accuracy than metastatic tissue specimens.

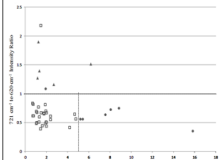


Figure 5 2D score plot of the 620 cm⁻¹ to 782 cm⁻¹ peak ratio versus the 721 cm⁻¹ to 620 cm⁻¹ peak ratio. Each data point is the patient average from spectra that have been vector normalised and 5th polynomial subtracted.

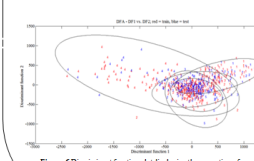


Figure 6 Discriminant function plot displaying the separation of breast met (1), colon/rectum met (2), lung met (3), melanoma met (4) and oesophagus & stomach met (5) based on the train set (red) and test set (blue) with a 95% confidence limit represented by ellipse.

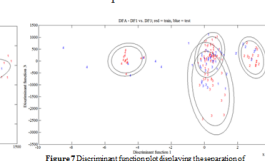


Figure 7 Discriminant function plot displaying the separation of primary breast (1), primary colon/rectum (2), primary melanoma (3) and primary oesophagus & stomach (4) cancer based on the train set (red) and test set (blue) with 99% (outer ellipse) and 95% (inner ellipse) confidence limits.

Conclusions and Future Work

> The ratios of small wavenumber regions allow rapid directed analysis to discriminate GBM, metastatic and normal brain tissue. Raman spectroscopy can be used as a diagnostic tool for metastatic brain cancer.

> Raman spectroscopy substrates have a significant influence on the outcome of resulting spectra and the dewaxing procedure.

> The ability of Raman spectroscopy to discriminate between primary cancer sites of origin from metastatic brain tissue needs to be further investigated.

Acknowledgements

The authors would like to acknowledge the support of the Sydney Detsell Neuroscience Foundation, Brain Tumour North West, the Centre for Materials and Science at the University of Central Lancashire, the FOCUS Institute at Dublin Institute of Technology, the European Community Action Scheme for the Mobility of University Students and the Association of British Spectroscopists.



uranium 92 U 238.03	carbon 6 C 12.011	lanthanum 57 La 138.91	nitrogen 7 N 14.007
------------------------------	----------------------------	---------------------------------	------------------------------

Investigating Immersion and Non-Immersion Raman Spectroscopy to Identify Primary Sites of Origin in Metastatic Brain Cancer

Leanne M. Fullwood¹, Dave Griffiths², Katherine Ashton³, Timothy Dawson³, Robert W. Lea², Charles Davis³, Franck Bonnier⁴, Hugh Byrne⁴, and Matthew J. Baker^{1*}

¹Centre for Materials Science, Division of Chemistry, University of Central Lancashire, Preston, PR1 2HE, UK

²School of Pharmacy and Biomedical Sciences, University of Central Lancashire, Preston, PR1 2HE, UK

³Royal Preston Hospital, Sharoe Green Lane, Fulwood, Preston PR2 9HT, UK

⁴FOCAS research Institute, Dublin Institute of Technology, Kevin Street, Dublin 8, Ireland

*email: mjbaker@uclan.ac.uk

Aim: To evaluate the use of Raman spectroscopy as a diagnostic tool for metastatic brain cancer and assess its ability to identify primary sites of origin.

Materials and methods

Tissue samples

> Tissue samples (Table 1) were obtained from the Brain Tumour North West bio bank from a total of 41 patients (Ethical Approval: BTNW/VRTB 13_01)

> Each tissue sample was sectioned at 10 µm onto three different Raman substrates: CaF₂, Spectroil and MiriR.



Figure 1: Tissue dewaxing process.

Table 1: Tissue sample collection.

Sample type	No. of Samples
Normal	7
GBM	5
Lung	5
Breast	6
Metastatic brain (n=20)	
Melanoma	5
Colon Rectal	6
Oesophageal Stomach	4
Breast	4
Melanoma	1
Colon Rectal	1
Oesophageal Stomach	1
Primary (n=7)	

Tissue dewaxing

> The tissue blocks used were formalin fixed-paraffin embedded for preservation. Thus, dewaxing needed to be carried out prior to Raman spectroscopic analysis to reduce spectral contributions from the paraffin wax.

> This was carried out by 3, 5 minute baths of Histoclear followed by 3, 5 minute baths of ethanol. The tissue sections were then left to air-dry and stored in a desiccator until Raman analysis took place.

Raman Spectroscopy

> Raman spectroscopy is an analytical technique based on the interaction of monochromatic light and matter. This interaction causes molecules within a sample to vibrate, a change in polarisability results in light scatter which can be detected to produce a characteristic spectrum.

Immersion Raman operates a water/tissue interface, which decreases the level of stray light. Photo-damage is reduced enabling stronger and shorter wavelength lasers to be used and longer acquisition times to be employed, thus improves spectral quality [1, 2].

> As a tissue becomes diseased, molecular changes occur which should be reflected in its spectrum. Raman spectroscopy is a non-destructive, non-subjective, economic and rapid technique to use. In vivo applications can reduce and aid biopsy [3].

> Approximately 20 spectra were collected per sample, using laser lines 785 nm and 532 nm, in the wavenumber region of 400-1800 cm⁻¹. Each spectrum was accumulated twice for 30 seconds.



Figure 2: Raman spectroscopy setup.

Results

> Raman spectra were generated of the substrate backgrounds which showed that CaF₂ produces a lower intensity background than Spectroil and MiriR, and thus, interacts with Raman spectroscopy the least.

> Paraffin peaks were present in the tissue spectra on Spectroil and CaF₂, shown by the asterisks above the corresponding peaks in figure 3, yet absent in the spectra from the MiriR substrates.

> Spectra were produced from dewaxed paraffin covered substrates without tissue present. This further confirmed that paraffin wax was not present on the MiriR substrate yet remained on the Spectroil and CaF₂.

> Spectra were produced from normal, metastatic and GBM brain tissue (figure 4) and analysed. Spectral differences were observed between the tissue types enabling differentiation between their spectra.

> The intensity of the 782 cm⁻¹ peak is dramatically lower in normal brain tissue spectra than in GBM and metastatic brain tissue spectra.

> In GBM spectra a 718 cm⁻¹ peak is observed, yet is absent from normal and metastatic brain spectra.

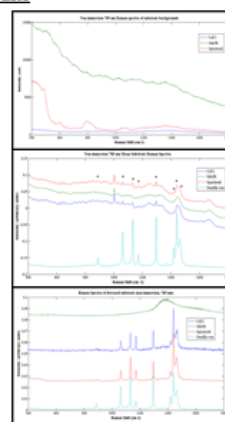


Figure 3: Top set of spectra. Substrate peaks visible on all spectra. These measured substrates after the waxing process on all spectra. Substrate measured with paraffin wax after dewaxing.

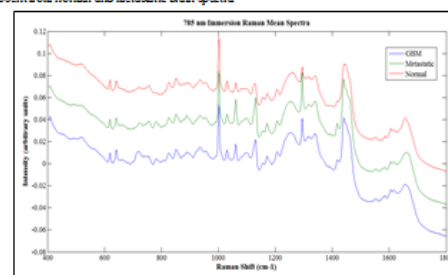


Figure 4: Bottom set of spectra. GBM, Metastatic, and Normal brain tissue spectra on CaF₂.

Conclusions and Future Work

> Raman spectroscopy can be used to identify cancer due to the spectral differences between normal, metastatic and GBM brain tissue.

> Raman spectroscopy substrates have a significant influence on the outcome of resulting spectra. Thus, further investigation needs to be carried out in order to optimise Raman spectroscopy and improve spectral quality.

> Raman spectra from metastases will be analysed to look at the ability of Raman spectroscopy to differentiate between different primary cancer sites of origin.

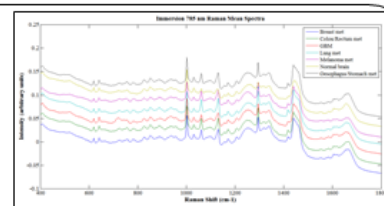


Figure 5: Spectra from normal, GBM, and Metastatic brain tissue, grouped by their primary site of origin.

Acknowledgements

The authors would like to acknowledge the support of the Sydney Dorell Neuroscience Foundation, Brain Tumour North West, the Centre for Materials Science at the University of Central Lancashire, the FOCUS Institute at Dublin Institute of Technology, the European Community Action Scheme for the Mobility of University Students and the Association of British Spectroscopists.



uranium 92 U 238.03	carbon 6 C 12.011	lanthanum 57 La 138.91	nitrogen 7 N 14.007
------------------------------	----------------------------	---------------------------------	------------------------------

Appendix 3 - A report entitled ‘Investigating the use of Raman and Immersion Raman Spectroscopy for Spectral Histopathology of Metastatic Brain Cancer and Primary Sites of Origin’, written based on the findings from this MSc (by research) currently under review by the authors for submission to ‘Analytical Methods’.

Investigating the use of Raman and Immersion Raman Spectroscopy for Spectral Histopathology of Metastatic Brain Cancer and Primary Sites of Origin

Leanne M. Fullwood¹, Graeme Clemens¹, Dave Griffiths², Katherine Ashton³, Timothy Dawson³, Robert W. Lea², Charles Davis³, Franck Bonnier⁴, Hugh J. Byrne⁴, and Matthew J. Baker^{1*}

¹ Centre for Materials Science, Division of Chemistry, University of Central Lancashire, Preston, PR1 2HE, UK

² School of Pharmacy and Biomedical Sciences, University of Central Lancashire, Preston, PR1 2HE, UK

³ Lancashire Teaching Hospital NHS Trust Royal Preston Hospital, Sharoe Green Lane, Fulwood, Preston PR2 9HT, UK

⁴ FOCAS Research Institute, Dublin Institute of Technology, Kevin Street, Dublin 8, Ireland

*Corresponding Author: MJBaker@UCLan.ac.uk

Abstract

It is estimated that approximately 13,000 people in the UK are diagnosed with brain cancer every year; of which 60% are metastatic. Current methods of diagnosis can be subjective, invasive and have long diagnostic windows. Raman spectroscopy provides a non-destructive, non-invasive, rapid and economical method for diagnosing diseases. The aim of this study was to investigate the use of Raman and immersion Raman spectroscopy for diagnosing metastatic brain cancer and identifying primary sites of origin using brain tissue. Through spectral examination, the Raman peaks at 721 cm^{-1} and 782 cm^{-1} were identified as being the most distinct for discriminating between the glioblastoma multiforme (GBM), metastatic and normal brain tissue spectra. A ratio score plot of these peaks calculated the classification sensitivities and specificities as 100% and 94.44% for GBM, 96.55% and 100% for metastatic brain, and 85.71% and 100% for normal brain tissue. Principal Component-Linear Discriminant Analysis (PC-LDA) also showed discrimination between normal, GBM and metastatic brain tissue spectra. We also present, for the first time, the use of Raman spectroscopy to investigate primary site of origin for metastatic brain cancer and any biochemical differences between different primary and metastatic cancer using linked samples. This study

revealed interesting spectral differences in the amide regions showing changes in the biochemistry of the metastatic brain cancer from the primary cancer

Keywords: Immersion Raman, Vibrational Spectroscopy, Diagnosis, Brain Cancer, Metastatic

Introduction

It is estimated that a third of people in the UK will develop cancer at some point during their lifetimes; and approximately 50% of these will die as a result of the disease within five years after diagnosis [1]. Brain metastases are the most common form of intracranial neoplasms in adults and are predicted to develop in 20-40% of cancer patients [2]. It is reported that around 13,000 people in the UK are diagnosed with brain cancer every year, of which, 60% are metastatic tumours that have originated from primary cancers located outside the central nervous system [3]. All cancers have the potential to metastasise and their probability of doing so is influenced by their location; lung cancer is the most common cancer to metastasise and is responsible for 50% of all brain metastases, breast cancer is the second most common and accounts for 15-25%, melanoma accounts for 5-20%, and the remaining 5-30% are as a result of other cancers [4]. Identifying the site of origin of the primary tumour increases the efficiency of treatment and thus patient survival; however, in 15% of metastatic cases, the location of the primary cancer is unknown [5].

The current method of diagnosis for brain metastases and their primary sites is histopathological analysis. The cancer type and the origin of the primary cancer can be identified based on the tissue architecture observed [6]. This method requires a trained neuropathologist, has a long diagnostic window, and can be subjective [7]. As well as these issues, disagreement amongst pathologists is reported to occur in up to 43% of

specimens [8]. The accurate and rapid diagnosis of disease allows early intervention of appropriate treatment, thus increasing life expectancy and reducing healthcare costs [9]. Therefore, there is a requirement for non-subjective techniques that can rapidly and accurately identify disease.

Raman spectroscopy is an analytical technique that utilises the phenomenon of inelastic light scattering to produce characteristic spectra unique to specific samples. When a tissue becomes diseased, molecular changes occur, which should be reflected in its spectrum. The identification of spectral differences between healthy and diseased tissue should enable objective diagnosis of specific diseases. Raman spectroscopy is not significantly affected by water and thus can be used *in vivo* to reduce and aid biopsy [10]. Raman spectroscopy is also a non-destructive, rapid and economical technique, making it an attractive method for diagnosis [11].

The potential of Raman spectroscopy as a diagnostic technique for diseases has been demonstrated by a variety of studies. Many papers have shown the ability of Raman spectroscopy to diagnose cancers, such as: brain cancers using tissue on low-E microscope slides and CaF₂ slides respectively [12, 13], lung tumours through the analysis of bronchial tissue sections [14], gastric adenocarcinomas using tissue samples [15, 16], non-melanoma skin cancers from the analysis of tissue *in vivo* [17], laryngeal cancers from tissue at endoscopy [18], breast cancers using fresh and frozen tissue specimens respectively [19, 20], cervical cancers from tissue *in vivo* and *ex vivo* [21, 22], bladder and prostate cancers from tissue sections [23, 24] and oesophagus and colon cancers through the analysis of snap frozen tissue on CaF₂ [25].

Gajjar *et al.* reported the ability of Raman spectroscopy to differentiate between brain tumour and healthy brain tissue [12]. They observed successful discrimination between different brain tumour types in their study. They reported that metastatic brain tissue could be recognised from healthy brain tissue on low-E substrates based on

spectral peaks at: 997 cm^{-1} (phospholipids and glucose-I-phosphate), 1077 cm^{-1} and 1446 cm^{-1} (lipids and proteins), 1241 cm^{-1} (Amide III), $\approx 1460\text{ cm}^{-1}$ (cytosine) and 1654 cm^{-1} (Amide I) [12].

Tissue samples are usually fixed using formalin and impregnated with paraffin wax to preserve the tissue for future analysis. The addition of paraffin also provides support for the microtomy process, enabling the sectioning of the tissue block for microscopic examination. However, prior to histological and Raman analysis, tissue sections must undergo a dewaxing process to remove the added paraffin. This then allows histological staining of the tissue for pathological examination, and reduces the paraffin contributions in Raman spectra. Ó Faoláin *et al.* investigated the efficacy of dewaxing procedures on formalin fixed, paraffin preserved (FFPP) cervical tissue on glass slides [26]. They reported that dewaxing procedures employing the commonly used, xylene and histoclear solvents, do not completely remove all of the paraffin wax; they found hexane to be a much more efficient dewaxing agent [26]. However it requires 18 hours of tissue submersion and is not clinically used for dewaxing procedures, conventional clinical dewaxing procedures were employed here [27].

Immersion Raman spectroscopy utilises an immersion lens which is in direct contact with an appropriate liquid, such as deionised water covering a sample under investigation. Bonnier *et al.* describe and successfully demonstrate the use of immersion Raman spectroscopy for both live cell and the first example of *in vitro* tissue specimens on CaF_2 , and observed an improvement in spectral quality, sample stability and the reduction of spectral background [28, 29]. Bonnier *et al.* [28, 29] demonstrated that fluorescence, contributing to spectral background, is only significant from sources producing short wavelengths of light, as proteins typically only fluoresce when sources producing wavelengths below 500nm are used and therefore, the background contribution seen from spectra acquired when using 785 nm lasers should not be

attributed to fluorescence, but to morphology dependant scattering of the incident light, and Raman lines that cause non-collimated entry into the spectrometer as stray light. The exchange of a tissue/air interface with a tissue/liquid interface results in more uniform refractive indices, thus reducing this level of stray light, and in turn, the intensity of the spectral background. Submerging the sample in liquid also protects the tissue specimen from photo-damage; enabling more powerful lasers of shorter wavelengths to be used, longer acquisition times and higher numbers of accumulations to be employed hence, improving spectral quality.

We present a comparison of Raman and immersion Raman recorded spectra, with a study highlighting the use of immersion Raman spectroscopy for the rapid diagnosis of site of origin of metastatic brain tumours. Vibrational spectroscopy has the ability to revolutionise the clinical environment allowing for increased efficiency within the diagnostic regime with corresponding decreases in mortality, morbidity and economic impact upon the health services [30].

Experimental

Study participants

Tissue sections were cut using a microtome. Parallel tissue sections of 4 μm in thickness were cut for glass microscope slides and 10 μm for CaF_2 (Crystran, UK) substrates. Tissue was obtained from formalin fixed paraffin preserved (FFPP) tissue blocks from the Brain Tumour North West (BTNW) bio-bank under ethical approval (BTNW/WRTB 13_01). Patient data consisted of histological information, patient gender, and date of birth and origin of metastasis/histological subtype. A total of 48 tissue specimens were obtained from 41 different patients. Tissue consisted of normal brain samples (n=7), glioblastoma multiforme (GBM) brain samples WHO (World Health Organisation) grade IV (n=5), metastatic brain samples (n=29) and primary

cancer tissue samples (n=7). Table 1 displays further information about the tissue specimens.

Table 1 Patient details with histological subtype and metastatic origin.

BTNW no.	Gender	DOB	Origin of Metastasis/histological subtype
119	F	26/06/1963	Breast (met and primary site)
707	F	07/08/1945	Breast (met and primary site)
756	F	15/03/1957	Breast (met and primary site)
888	M	25/11/1948	Colon/rectum (met and primary site)
985	M	05/02/1933	Melanoma (met and primary site)
988	M	30/12/1949	Oesophagus & stomach (met and primary site)
1001	F	20/12/1944	Lung (met only)
690 / 1012	F	25/10/1960	Breast (met and primary site)
1004	F	03/09/1956	Breast (met only)
998 / 1010	M	25/07/1946	Colon (met only)
1020	F	05/06/1948	Breast (met only)
2	F	28/10/1937	GBM
3	F	22/09/1981	GBM
4	M	08/12/1942	GBM
5	F	29/10/1958	GBM
7	M	14/04/1939	Normal Brain
10	F	13/06/1929	GBM
78	F	24/09/1955	Lung (met only)
106	F	14/02/1965	Normal Brain
132	F	24/06/1943	Normal Brain
136	F	25/09/1956	Normal Brain
137	M	26/04/1944	Colon/rectum (met only)
164	M	10/04/1954	Oesophagus & stomach (met only)
184	F	21/11/1948	Lung (met only)
215	M	21/01/1973	Lung (met only)
274	M	12/07/1940	Colon/rectum (met only)
295	F	12/06/1936	Lung (met only)
358	M	08/05/1935	Melanoma (met only)
409	F	08/08/1925	Colon/rectum (met only)
444	M	30/01/1978	Normal Brain
509	M	11/02/1930	Melanoma (met only)
517	F	05/06/1955	Lung (met only)
521	M	18/01/1949	Oesophagus & stomach (met only)
562	F	12/03/1953	Lung (met only)
567	F	09/04/1947	Melanoma (met only)
668	F	30/08/1943	Colon/rectum (met only)
678	F	13/11/1961	Normal Brain
688	F	15/06/1965	Melanoma (met only)
694	M	18/09/1951	Lung (met only)
721	F	04/01/1976	Oesophagus & stomach (met only)
772	M	21/09/1972	Normal Brain

Dewaxing and Haematoxylin and Eosin staining of tissue

Tissue sections on the microscope slides were stained with Haematoxylin and Eosin (H&E) for histological examination So as to remove the paraffin, tissue sections

were de-waxed through 2 x 5 minute baths of HistoClear followed by 2 x 5 minute baths of ethanol. Prior to H&E staining, tissue sections were washed in distilled water for 5 minutes after de-waxing. Sections were then bathed in haematoxylin for 5 minutes and washed in warm tap water to allow the nuclei to turn blue. The sections were then covered in eosin for 4 minutes and washed off with distilled water. Finally, the tissue sections were dehydrated in 2 x 5 minute baths of ethanol and cleared in 2 x 5 minute baths of HistoClear tissue sections were protected and preserved through the application of Histomount and a coverslip. The sections were then microscopically examined in order to identify the metastatic sites present in the tissue.

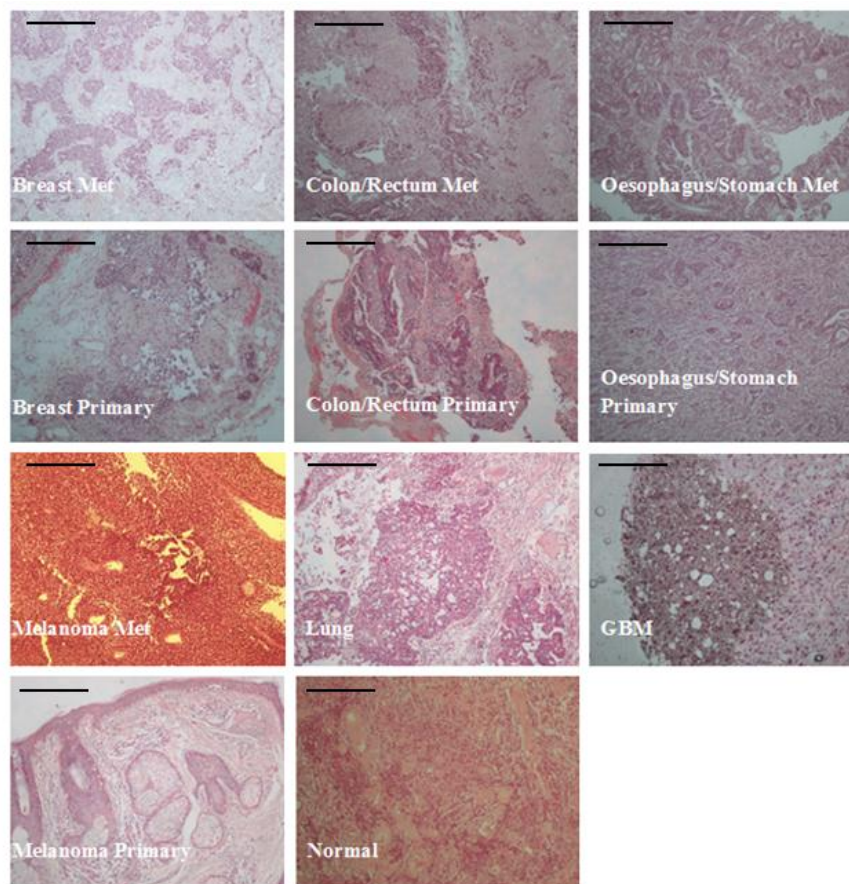


Figure 1 Microscopic images of H&E stained tissue sections of normal brain, metastatic brain, primary sites and GBM brain WHO grade IV (x 100). Scale bar represents 50 microns.

Figure 1 shows the microscopic images of the H & E stained tissue samples at x 100 magnification. It can be observed that normal, metastatic and GBM brain tissue

architecturally differ from one another, with differences also being observed between the differing metastatic types.

Tissue section preparation for Raman spectroscopic analysis

The tissue sections on the CaF₂ substrates also needed to be de-waxed prior to Raman analysis, in order to reduce the paraffin peak contributions in the spectra. The de-waxing procedure consisted of 3 x 5 minute baths of HistoClear followed by 3 x 5 minute baths of ethanol. The sections were left to air dry for 30 minutes, placed in a Petri dish and stored in a desiccator until spectroscopic analysis.

Raman spectroscopy instrumentation and analysis

Spectroscopic measurements were carried out on a Horiba Jobin-Yvon LabRAM HR800 spectrometer. An air cooled CLDS point mode diode 785 nm laser with a single edge filter (cut off to 100 cm⁻¹) and an output power of 300mW was used to acquire spectra; which was used with a grating of 300 gr/mm and blazed at 1000 nm. Non-immersion point spectra were acquired using a 0.9 numerical aperture (x 100) (MPlanN) objective and immersion point spectra were acquired using a 0.75 numerical aperture (x 60) objective (LUMPlanFLN, Olympus). The confocal hole was set at 100 µm for 785 nm spectral collections. The detector used was an Andor electromagnetic (EM) charged coupled device (CCD). A video camera within the Raman system was used to take images of the specimens.

The instrumentation was calibrated before operation to silicon at the spectral line of 520.8 cm⁻¹. Spectra were acquired using the 785 nm laser at 100% exposure for 30 s and accumulated twice, with both the immersion and non-immersion objectives. A total of 1574 spectra were generated through the production of 20 spectra from three to five areas on each tissue sample, ensuring a representative area was used to gather data.

Immersion Raman spectroscopy was carried out by submerging the tissue sample in deionised water for spectral collection.

Data pre-processing and multivariate analysis

Pre-processing and multivariate analysis was carried out on the raw data using LabSpec 6 spectroscopy software suite (HORIBA Scientific) and MATLAB version 7.11.0 (R2010b) (The MathWorks, Inc., USA) using in-house written software. Pre-processing methods were kept to a minimum to enable better reproducibility; data were background subtracted through the application of a fifth order polynomial and smoothed using 7 point smoothing (Labspec 6) and vector normalised. Paraffin peaks were removed from the spectra for multivariate analysis at the following wavenumbers: 882 cm^{-1} - 912 cm^{-1} , 1051 cm^{-1} - 1071 cm^{-1} , 1115 cm^{-1} - 1143 cm^{-1} , 1163 cm^{-1} – 1187 cm^{-1} , 1284 cm^{-1} – 1305 cm^{-1} and 1407 cm^{-1} – 1501 cm^{-1} . Multivariate analysis was then carried out on the data set using PC-DFA.

Principal component analysis (PCA) is an unsupervised multivariate algorithm used to find spectral differences between recorded spectra. Being unsupervised means that the algorithm has no priori information on the grouping of the recorded spectra, PCA can only find orthogonal dimensions of spectral variance. One advantage to PCA is that can be used to reduce the dimensionality of the dataset prior to discriminate classification algorithms, such as Linear Discriminant Analysis (LDA). Without dimension reduction, LDA can overfit, producing over generous classification results based on random errors or noise, and not on the relationships between the recorded spectra. LDA is a supervised technique requiring prior knowledge of the group classes beforehand. LDA then finds the best linear hyperplane between the class groups at each variable dimension, maximising the intergroup variance and minimising the intragroup variance. The PC-LDA models created were tested using cross-validation, partitioning

the data matrix into two sets (training set and test set). One third of the original data set was randomly removed while the remaining training set data is used to build the classification model. The classification model is then tested using the removed (blind) test set spectra [31, 32]. The performance of the model is judged on how well the model, built using the training set, predicts the new and previously unseen test set data. PC-LDA model performance was judged through the percentage of test set spectra correctly classified (%CC) and spectra classification sensitivities and specificities based on the confidence ellipses plotted (95% (outer ellipse) and 90% (inner ellipse)). This study investigates three different PC-LDA models.

Results and Discussion

Raman and Immersion Raman spectroscopy comparison

The averaged raw spectra of all tissue samples on CaF₂ using immersion and non-immersion Raman spectroscopy are shown in Figure 2. It is clear that the averaged immersion Raman spectrum has an initial lower spectral background than the averaged non-immersion spectrum in the 600 cm⁻¹ to 930 cm⁻¹ spectral range, which remains at a relatively stable intensity throughout. Immersion Raman also produces better delineated peaks with larger areas than spectra acquired by non-immersion Raman. Therefore, due to the advantage of better spectral quality, immersion Raman spectroscopy was chosen over standard techniques to analyse its potential as a diagnostic tool for metastatic brain cancer and its ability to identify primary cancer sites of origin.

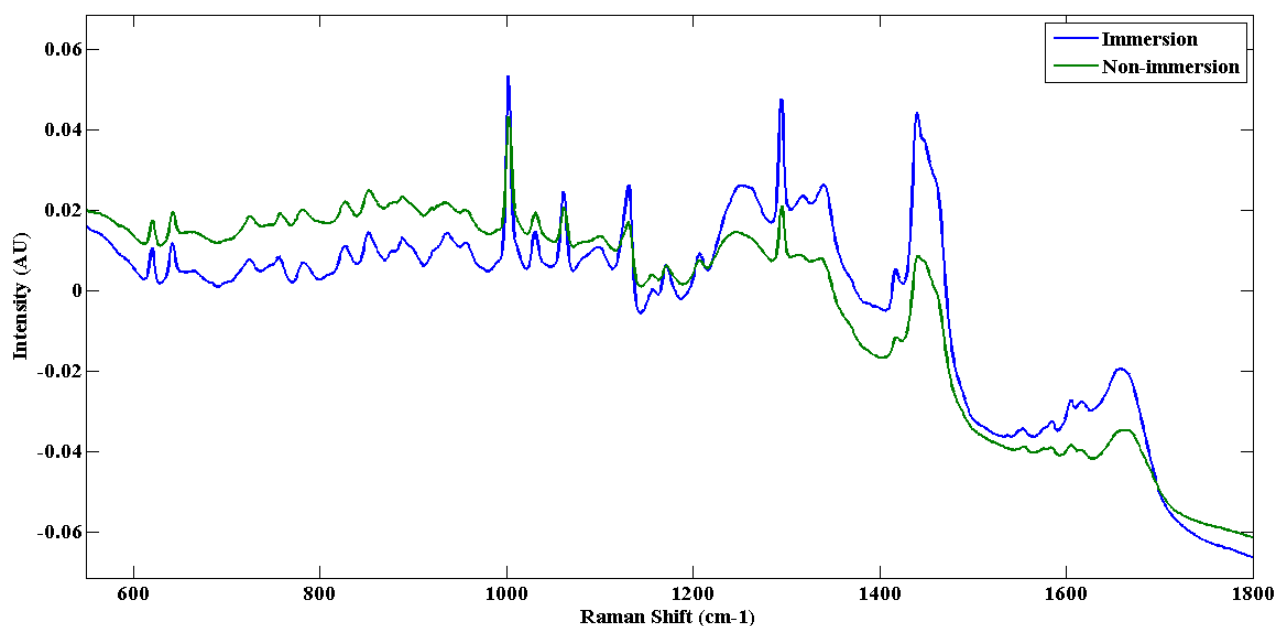


Figure 2 Immersion Raman average spectrum produced through averaging 1116 immersion acquisitions using a x 50 objective. Non-immersion averages spectrum was produced using 458 non-immersion acquisitions using a x 60 objective.

Spectral Histopathology:

Cancer vs. Metastatic Tumours vs. Non-Cancer

The averaged, vector normalised and background-subtracted immersion Raman spectra of normal (157 spectra from 7 patients), metastatic (668 spectra from 31 patients) and GBM (127 spectra from 5 patients) brain tissue on CaF₂ substrates are displayed in Figure 3. Table 2 lists the assignments of the major peaks present in recorded spectra, based on literature [14, 25, 33-35]. Spectral differences between these tissue types are observed at the various peaks throughout the averaged spectra. The peak at 721cm⁻¹, assigned as the C-N symmetric stretch of choline [33, 34], is prominently observed in GBM tissue. In normal and metastatic tissue this peak is not present, although a 725 cm⁻¹ peak, assigned to adenine is present [36] (Figure 3). Choline content has been observed to increase in GBM tissue and all primary tumours through magnetic resonance spectroscopy; thought to be caused by increased cell proliferation

and cell membrane turnover, resulting in an increased production of choline transporters and kinase enzymes [37].

GBM and metastatic tissue both exhibit 782 cm^{-1} peaks of a considerable intensity in their spectra, assigned to nucleotide ring breathing [25], whereas the peak in the normal tissue spectrum is much weaker and is not easily identifiable in the spectra. A peak at $\sim 1081\text{ cm}^{-1}$, assigned to PO_2^- symmetric stretching (nucleic acids) [38], is observable in the averaged spectrum of normal brain tissue yet appears absent from the spectra of cancerous tissue (Figure 3).

An amide III peak is present at 1263 cm^{-1} [35] in the normal tissue spectrum but for GBM and metastatic brain tissue spectra, the peak has been shifted to 1250 cm^{-1} , possibly as a result of peak broadening, or changes in hydrogen bonding. As well as the shift, there is a noticeable increase in amide III peak intensity from the GBM and metastatic brain average spectra, when compared to normal tissue spectrum. As the 782 cm^{-1} has previously associated with ring breathing vibrations of nucleic acids [39] the increase in intensity from the 782 cm^{-1} and may suggest an increase in cellular density from the cancerous tissue. The increase in intensity from the amide III band may well be in agreement with this, showing an increase in cellular proteins as a result of increased cell mass in the tissue.

The peak present at approximately 1658 cm^{-1} , attributed to the C=O stretch of amide I [25] appears to be shifted in the average spectrum of metastatic to a higher Raman shift of 1661 cm^{-1} . The intensity of this 1658 cm^{-1} peak is also decreased in both the cancerous spectra. This is consistent with the report of Gniadecka *et al.*, who found reduced intensities of the amide I band of proteins in the spectra of melanoma. The

changes in the amide bands between the normal and melanoma specimens are attributed to conformational changes to the protein structures [40].

It can also be observed from the averaged spectrum of normal tissue that the paraffin peaks (asterisked peaks) present are of a much lower intensity than those in the spectra of metastatic and GBM tissue. This could be attributed to either structural or compositional differences between the tissue types showing a tissue effect on the dewaxing efficacy [27].

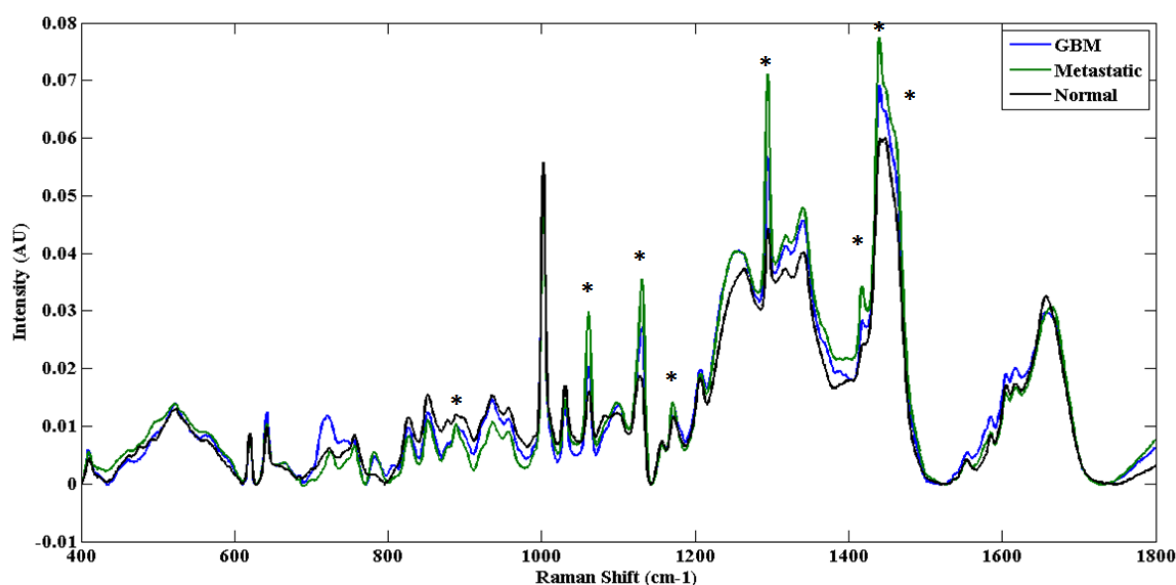


Figure 3 GBM, Metastatic and normal brain tissue average spectra, recorded using immersion Raman spectroscopy. The GBM spectrum was created from averaging 127 GBM acquisitions, the Metastatic from 668 metastatic acquisitions and the normal brain spectrum from 157 normal brain acquisitions. Spectra have been vector normalised, the backgrounds have been corrected using a 5th order polynomial fit and 7 points of smoothing. The asterisks correspond to paraffin peaks from residual wax in the tissue.

Table 2 Bio-molecular assignments of main spectral peaks.

Raman Shift (cm ⁻¹) of peak	Tentative assignment [14, 25, 33-35, 38]
524	S-S stretch in proteins
550	Tryptophan/cytosine, guanine
620	C-C twisting mode of phenylalanine
641	C-C twisting mode of tyrosine
666	C-S stretching mode of cystine
721 (only GBM)	Symmetric choline C-N stretch (membrane phospholipid head)/adenine
725	Adenine/C-S (protein)/C-H ₂
756	Symmetric breathing of tryptophan

782	Cytosine/uracil ring breathing of nucleotide
805	A-DNA [38]
827	DNA O-P-O, cytosine, uracil, thymine
852	(CCH) ring breathing mode of tyrosine and C-C stretch of proline ring
870	Proline
888	Paraffin wax
925	C-C stretching mode of proline [38]
934	C-C stretching mode of proline and valine and α -helix protein backbone/glycogen
957	Hydroxyapatite (PO_4^{3-} symmetric stretching) /carotenoid/cholesterol
1002	Symmetric ring breathing mode of phenylalanine
1031	C-H in-plane bending mode phenylalanine
1061	Paraffin wax
1081 (only normal)	PO_2^- symmetric stretching (nucleic acids) [38]
1098	C-C/C-O phospholipids
1131	Paraffin wax
1156	C-C carotenoids, C-N stretching of proteins
1171	Paraffin wax
1207	Hydroxyproline, tyrosine/tryptophan, phenylalanine ($\text{C}-\text{C}_6\text{H}_5$)
1234	Antisymmetric phosphate stretching [38]
1250	Amide III: (β -sheet, protein) [38]
1263 (only normal)	Amide III: (α -helix, protein) [38]
1294	Paraffin wax
1318	CH_3 CH_2 twisting mode of collagen/lipids
1340	CH_3 CH_2 wagging mode of collagen, nucleic acids
1389	CH_3 bend
1397	CH_3 bending due to methyl bond in the membrane [38]
1417	Paraffin wax
1440	Paraffin wax
1449	CH_2 bending mode of proteins/((CH_3) (CH_2) collagen
1462	Paraffin wax
1554	C=C Tryptophan, porphyrin
1578	Guanadine, adenine, TRP (protein)
1584	Pyrimidine ring (nucleic acids) and heme protein/C=C phenylalanine
1604	C=C in-plane bending mode of phenylalanine and tyrosine, C=C porphyrin
1618	C=C stretching mode of tyrosine and tryptophan
1658	Amide I (C=O stretching mode of proteins, α -helix conformation)/C=C lipid stretch
1670	Amide I (Proteins with β -sheet conformational structures)

The mean spectral intensity changes between spectral peaks of normal, GBM and metastatic brain tissue (Figure 3) indicate alterations in specific biomolecule

concentrations when the tissue is in different states of health. These observable spectral differences demonstrate the ability of Raman spectroscopy as a potential diagnostic tool for brain cancer.

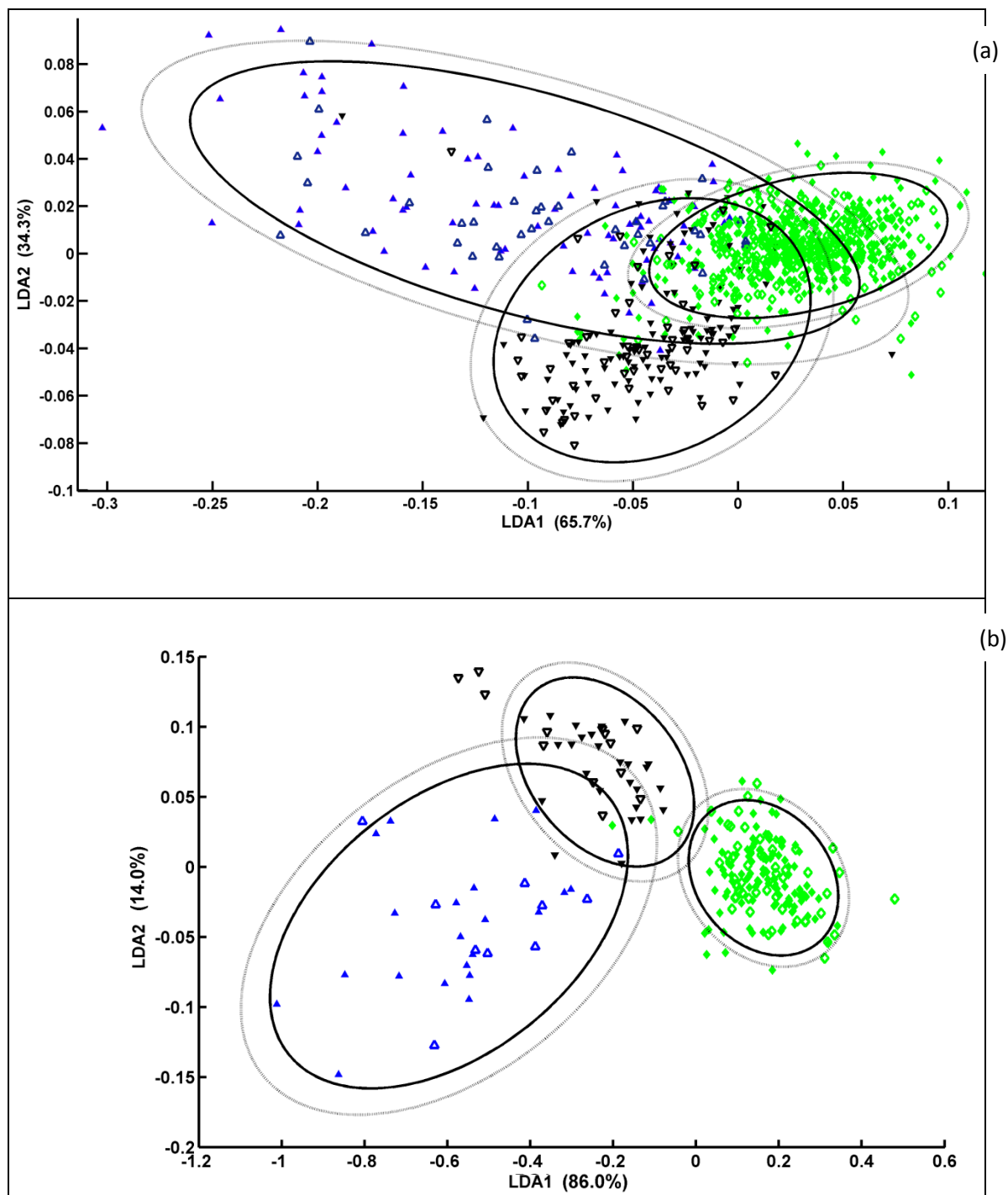


Figure 4 (a) LDA scores plot showing the separation of GBM (blue), metastatic (green) and normal brain tissue (black) spectra. Training spectra displayed with symbols filled and test spectra unfilled, 95% (outer ellipse) and 90% (inner ellipse) confidence limits are also shown; PC-LDA training model created using the first 12 PCs, which achieved a %CC score of 72% (b) LDA scores plot of the same data used in (a) but with the spectra averaged. The 20 spectra recorded from each patient tissue sample were split into 4 and averaged. The training model was created using the first 8 PCs and achieved a % CC score of 97%.

As a result of there being spectral differences between GBM, Metastatic and normal brain tissue mean spectra (Figure 3), the recorded spectra were investigated using PC-LDA to see if linear separation boundaries could be found between the spectra recorded from the different tissue types in multidimensional space (Figure 4). Figure 4 shows a LDA scores plot (LDA1 vs. LDA2) of spectra recorded from GBM, Metastatic and normal brain tissue using immersion Raman spectroscopy. Although complete separation of the different tissue type spectra is not seen in the LDA scores plot (a degree of overlap seen between the different groups), there is some separation between spectra recorded from all three tissue types. The majority of GBM and normal brain tissue spectra are separated from Metastatic tissue spectra along the LDA 1 axis, and the majority of normal brain tissue spectra can be discriminated from GBM spectra along the LDA 2 axis. However, it can be seen in Figure 1 that all tissue types have some degree of tissue heterogeneity, with some Metastatic tissue types and GBM tissue being very heterogeneous. The heterogeneous nature of GBM tissue is said to be due to areas of necrosis found in the tissue surrounded by pseudopalisades and microvascular hyperplasia, believed to be instrumental in the accelerated growth of GBM [41]. By investigating different areas on each tissue sample with Raman spectroscopy there is the possibility that non-cancerous tissue chemistry will be captured when investigating very heterogeneous cancerous tissue. This is possible reflected in Figure 4 (a), which shows that both Metastatic and GBM tissue spectra have some overlap with normal tissue spectra. Therefore, the spectra used for Figure 4 (a) was split into smaller groups and averaged (The 20 spectra recorded from each patient tissue sample were split into 4 and averaged). This produced the LDA model displayed in Figure 4 (b), which now shows good separation between all three classes of tissue spectra; producing a classification

model performance score of 97%CC. Details of both PC-LDA models created in Figure 4 can be found in Table 3.

Figure 5 displays the LDA loadings plots relating to the LDA scores plot in Figure 4 (b). Table 4 identifies the Raman shifts from the LDA 1 and 2 loading plots which are responsible for distinguishing normal, Metastatic and GBM tissue spectra. The LDA 1 axis separates the Metastatic tissue spectra from the rest. The main peaks in the LDA 1 loading plot included the 718, 925, 1250, 1400 and 1670 cm^{-1} Raman bands associated with symmetric choline C-N stretch (membrane phospholipid head)/adenine, C-C stretching mode of proline, Amide III band, CH_3 bending mode due to methyl bond in the membrane and the Amide I C=O stretching mode of β -sheet structural proteins respectively. These spectral differences are in agreement with the mean spectra and show the Metastatic tissue spectra to have reduced intensities from the 718 and 925 cm^{-1} peak's, and increased intensities from the 1250 1400, and 1670 cm^{-1} peaks when compared to the tissue spectra recorded from the GBM and normal tissue. The LDA 2 axis in Figure 4 (b) separates the majority of GBM and Metastatic spectra from normal tissue spectra. The main peaks in the LDA 2 loading plot included the 719, 780/805, 1078, 1234, 1268, 1653, 1672 cm^{-1} Raman bands associated with symmetric choline C-N stretch, cytosine/uracil ring breathing of nucleotide/A-DNA, PO_2 symmetric stretching (nucleic acids), antisymmetric phosphate stretching, Amide III: (α -helix, protein), Amide I (C=O stretching mode of proteins, α -helix conformation) and the Amide I C=O stretching mode of β -sheet structural proteins respectively. The loading peaks at 1235 and 1268 are in agreement with the mean spectral differences, which show the Amide III peak in the cancerous spectra to shift from 1268 cm^{-1} , associated with α -helix protein, to a lower frequency associated with β -sheet protein. The LDA 2 loading plot and mean spectral comparisons also show the cancerous spectra to have

reduced intensity from the Amide I α -helix peak when compared to the normal tissue spectra, while the cancerous spectra also show increased intensity at $\sim 1670\text{ cm}^{-1}$, associated with Amide I proteins with β -sheet structural conformations. This may suggest a link between protein secondary structure content and cancerous tissue. Yamada *et al.* also showed β -sheet protein levels to increase significantly when investigating necrotic areas of murine carcinoma using FT-IR microspectroscopy. The increase in β -sheet protein levels coincided with a sharp decrease in α -helix protein levels, in agreement with our results [42]. It can also be seen from the Figure 5 (b) that the cancerous tissue spectra have increased intensity from peaks associated with nucleic acids and DNA structures. As previously described, the increase intensity from nucleic acid structures may suggest an increase in cellular density from the cancerous tissue, in agreement with increased cell proliferation.

Table 3 PC-LDA model details, including spectral numbers and the resulting sensitivities and specificities.

	Train spectr a	Test spectr a	Confidence level	Histopathological type	Sensitivit y (%)	Specificit y (%)
GBM vs. norm vs. met	639	316	90%	GBM	90.48	22.26
				Normal	91.89	88.30
				Metastatic	98.08	59.09
			95%	GBM		
				Normal		
				Metastatic		

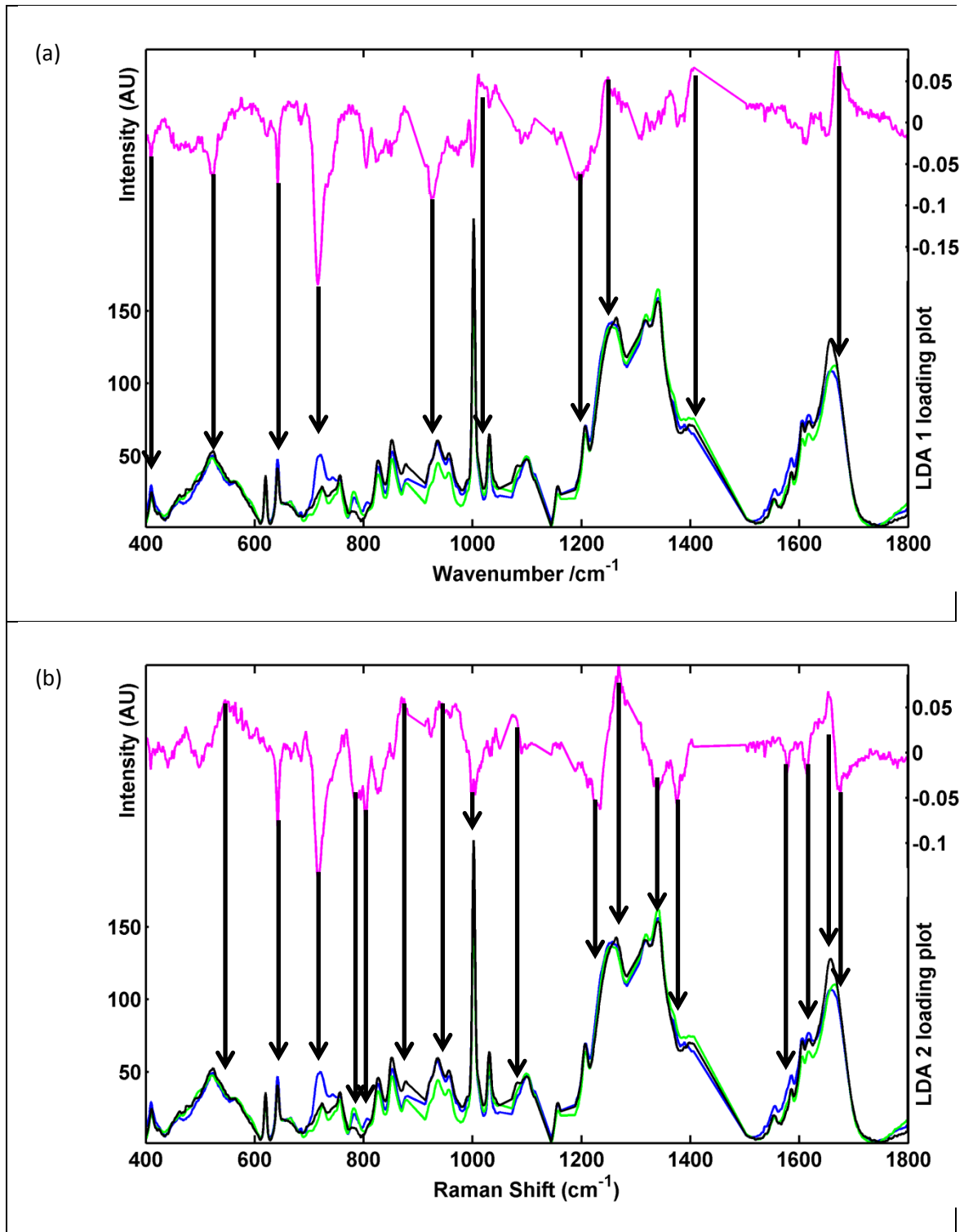


Figure 5 (a) PC-LDA loading plot of the LDA 1 separation boundary produced in Figure 4 (b) (pink) (upper curves) and mean spectra (lower curves), GBM (blue), metastatic (green) and normal tissue spectra (black) (b) PC-LDA loading plot of the LDA 2 separation boundary produced in Figure 4 (b).

LDA1 loading bands		LDA2 loading bands	
~Negative Loading	~Positive Loading	~Negative Loading	~Positive Loading
Band Position (cm ⁻¹)	Band Position (cm ⁻¹)	Band Position (cm ⁻¹)	Band Position (cm ⁻¹)
524	1010	642	550
642	1250	719	869
718	1402	780	1078
925	1670	805	1268
1200		998	1653
		1234	
		1338	
		1375	
		1578	
		1613	
		1673	

Table 4 Spectral differences causing the separations seen in Figure 4 (b).

From the mean spectral differences (Figures 3 and 5) it can be visibly seen that the average normal brain tissue spectrum has a low intensity from the 782 cm⁻¹ peak, when compared to the average GBM and Metastatic spectra. It can also be seen that the average GBM mean spectrum has a much greater intensity in the 721 cm⁻¹ peak than the average normal tissue and metastatic spectrums. As a result, a 2D scores plot was produced based on the intensity ratios between the 721/782 cm⁻¹ peaks and the 620 cm⁻¹ peak (620 cm⁻¹ peak intensity was relatively uniform in all the recorded spectra) (Figure 6). Figure 6 shows the 721 and 782 cm⁻¹ peaks to be significant discrimination markers for GBM, Metastatic and normal tissue spectra, with average GBM, Metastatic and normal tissue spectra clearly grouped in the 2D scores plot. This shows that the 721 and 782 cm⁻¹ peaks could potentially be markers for diseased tissue therefore, the monitoring of these peak intensities through Raman spectroscopy may aid the early diagnosis of disease. However, Figure 6 does show two spectra which cannot be grouped with their representative class, identified as patient 007 and 509, belonging to the normal and metastatic group respectively. Upon visual inspection of the spectra, it was observed that they notably differed from the total averaged spectra for their tissue types. This could potentially be a result of tissue misclassification.

Primary site analysis

Raman spectra were also recorded from tissue representative of primary cancers (breast, melanoma, oesophagus and stomach and colon/rectum) and patient averaged. The primary cancer tissue samples are linked samples (from the same patient) of corresponding metastatic tissue samples in the metastatic tumour model. As before, PC-LDA was performed on the spectra recorded from the tissue samples using immersion Raman spectroscopy. The LDA scores plot (Figure 7) shows that spectra recorded from the colon/rectum (blue) and oesophagus & stomach cancerous tissue (green) have some good separation from the remaining spectra. Less clear is the separation of the primary breast and melanoma tissue spectra which are shown to be spectrally similar. This may suggest that the tissue architecture of both primary breast and melanoma tissue is similar.

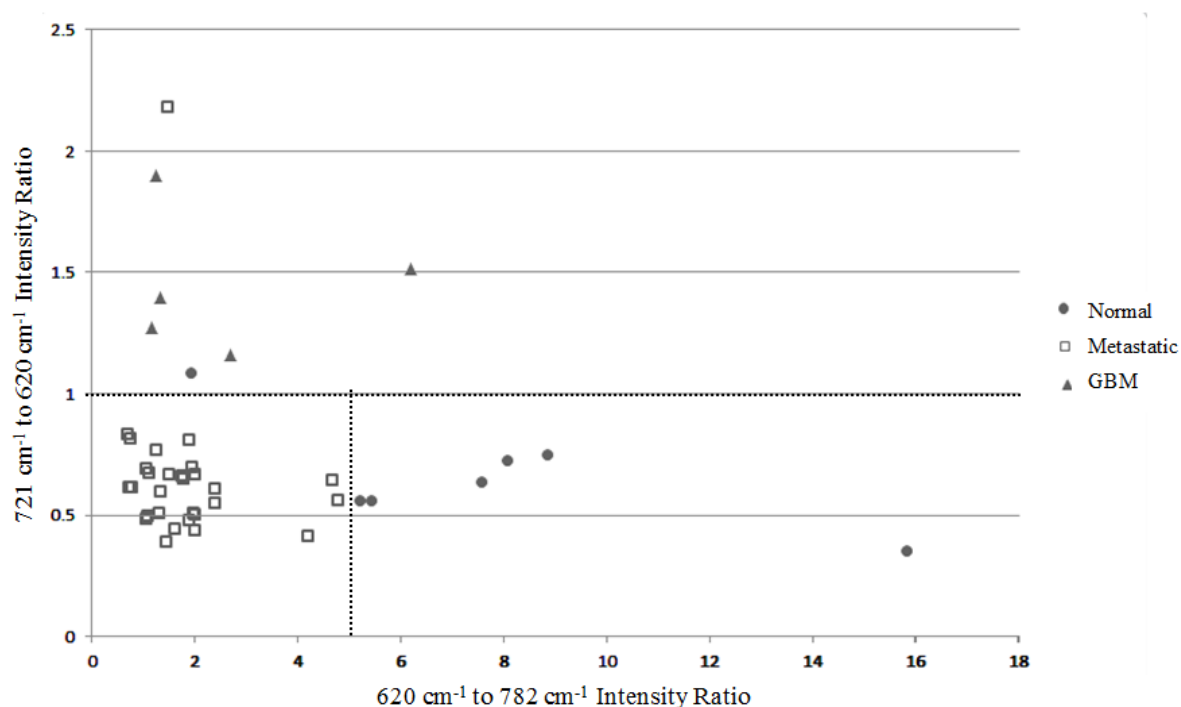


Figure 6 2D score plot of the 620 cm⁻¹ to 782 cm⁻¹ peak ratio versus the 721 cm⁻¹ to 620 cm⁻¹ peak ratio.

Each data point is the spectral patient average.

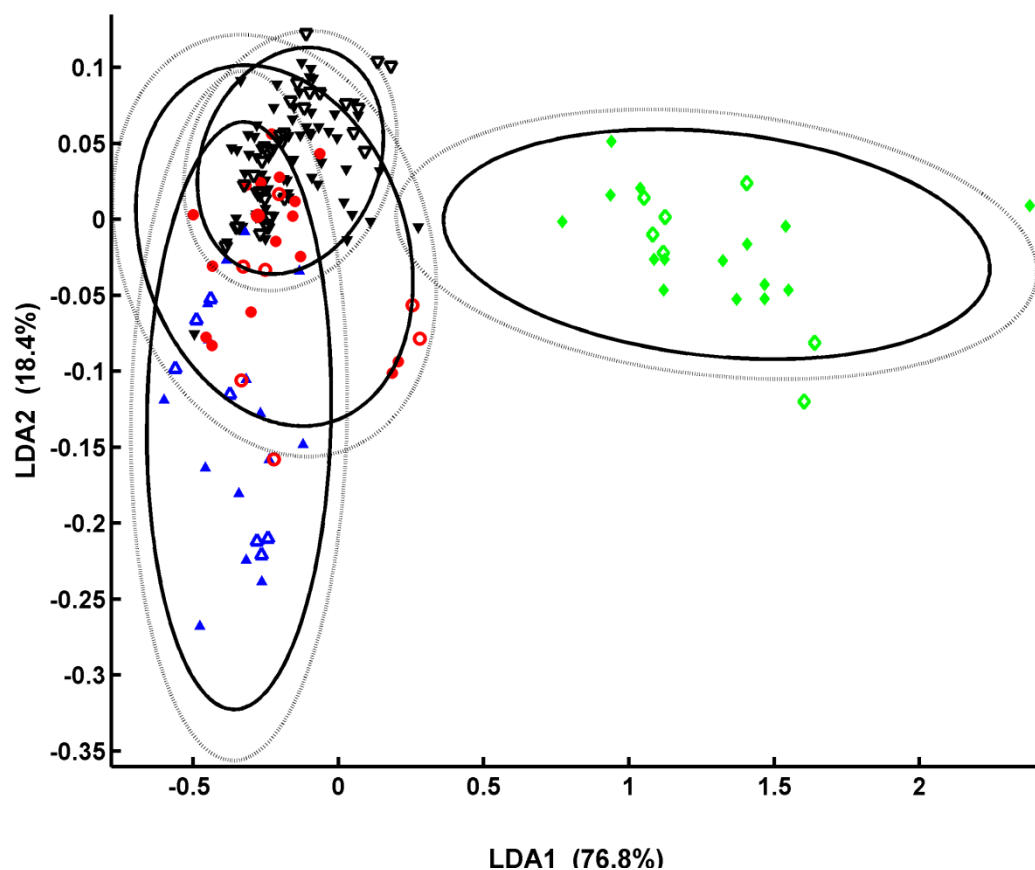


Figure 7 LDA scores plot of average spectra recorded from primary breast (**black**), primary colon/rectum (**blue**), primary melanoma (**red**) and primary oesophagus & stomach (**green**) cancerous tissue. Training spectra displayed with symbols filled and test spectra un-filled, 95% (outer ellipse) and 90% (inner ellipse) confidence limits are also shown; training model created using the first 12 PCs and achieved a % CC score of 72%.

	Train spectr a	Test spectr a	Confidence level	Histopathological type	Sensitiv y (%)	Specificit y (%)
Metastatic comparison			90%	Breast	89.29	85.71
				Lung	60.00	72.22
				Colon/Rectum	92.31	60.78
				Melanoma	80.00	83.33
				Oesophagus & stomach	87.50	54.17
Primary comparison	111	53	90%	Breast	89.29	85.71
				Colon/Rectum	100	54.76
				Melanoma	71.43	38.90
				Oesophagus & stomach	85.71	100

Table 5 PC-LDA model details, including spectral numbers and the resulting sensitivities and specificities.

Analysis of site of origin

Figure 7 shows that the identification of spectra recorded from some primary cancers is possible using multivariate classification algorithms. As the origins of metastatic brain tissue are determined from the tissue architecture observed, it should also be possible to determine metastatic brain tissue origins from the spectra recorded. Therefore, PC-LDA was also performed on the metastatic tissue data with the LDA scores plot displayed in Figure 8. As with the data used in Figure 4 (b), the 20 spectra recorded from each patient tissue sample were split into 4 and averaged. The LDA scores plot in Figure 8 shows that although there is some overlap between the spectra recorded from each type of brain metastases, there is some separation between metastatic breast (**blue**), melanoma (**red**), oesophagus & stomach (**black**) and colon/rectum (**green**)/lung (**cyan**) spectra. As spectra recorded from both metastatic colon/rectum and lung tissue almost overlap in LDA scores space, this may suggest that the different tissue types have similar tissue architecture. The spectral similarities may also be due to not enough spectra being recorded from the different tissue types, and as a result, spectra recorded from the three different sites of each patient sample have not been able to capture the differing tissue architecture which would discriminate between the two. However, it may also be possible that the movement of metastatic cancer from primary sites to the brain effects the biochemistry of the cancers, with all metastatic cancer found in the brain becoming biochemically similar due to their new environment. One of the reasons for this could be that the movement of metastatic cancer from primary sites to the brain effects the biochemistry of the cancers, with all metastatic cancer found in the brain becoming biochemically similar due to their new environment. This would suggest that biochemical differences between primary cancers are generally a result of the organ location and not the cancer type.

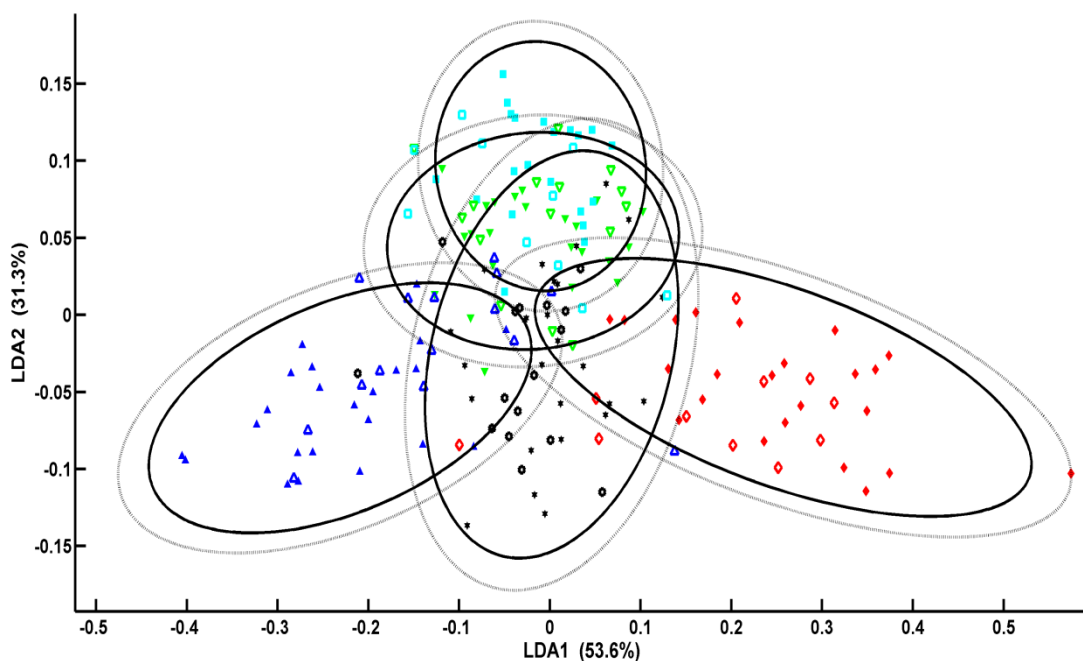
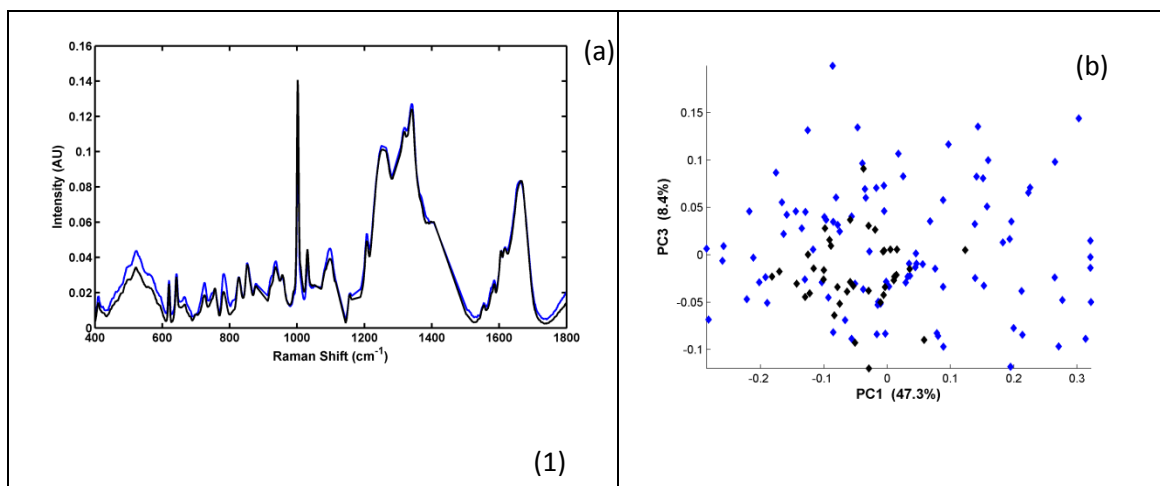


Figure 8 LDA scores plot of average spectra recorded from metastatic breast (blue), colon/rectum met (green), lung met (cyan) melanoma met (red) and oesophagus & stomach met (black). Training spectra displayed with symbols filled and test spectra un-filled, 95% (outer ellipse) and 90% (inner ellipse) confidence limits are also shown; training model created using the first 9 PCs and achieved a % CC score of 63%.



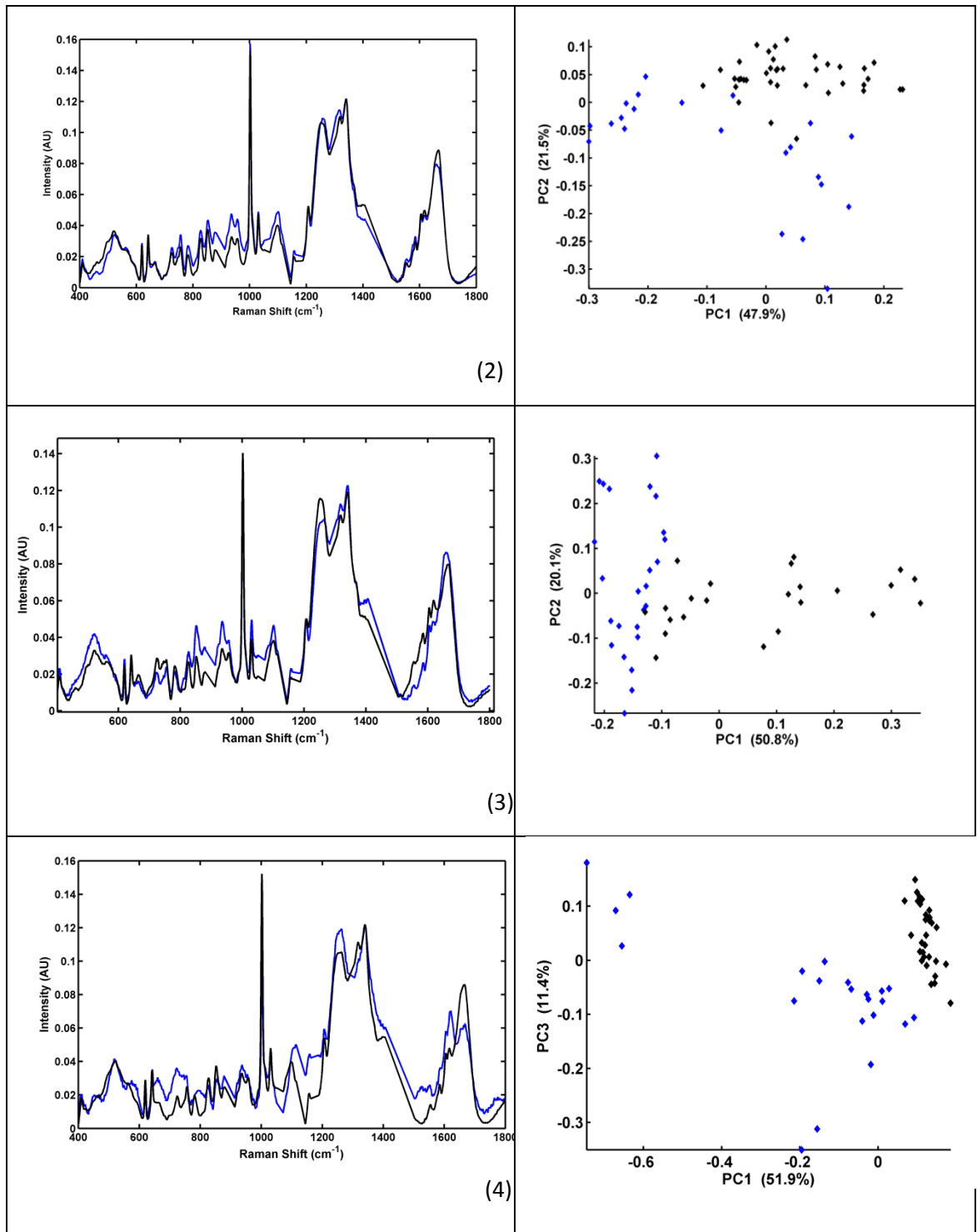


Figure 9 (a) Mean spectral comparisons of primary (blue) and Metastatic brain tissue (black) (b) PCA comparisons of primary and Metastatic brain tissue recorded spectra (2d PCA scores plot displaying the best separation between Primary and Metastatic tissue). The spectra have been vector normalised, baseline corrected by 5th order polynomial fit and subtraction, and 7 points of smoothing (1) Primary Breast spectra vs. Met Breast tissue spectra (2) Primary Colon/Rectum spectra vs. Met Colon/Rectum tissue spectra (3) Primary Melanoma vs. Met Melanoma tissue spectra (4) Primary Oesophagus and Stomach spectra vs. Met Oesophagus and Stomach tissue spectra.

Spectral analysis of primary site and corresponding brain metastasis

Figure 9 (a) displays the baseline-subtracted averaged spectra of both Metastatic brain and their corresponding primary sites. It is observable from Figure 9 (a) that the Metastatic spectra (**black**) from the different sites of primary origin all look similar, whereas the same cannot be said from the primary cancer spectra (**blue**), with primary Colon/Rectum, Melanoma and Oesophagus and Stomach tissue spectra all showing mean spectral differences when compared against their corresponding primary sites. This supports the theory that the movement of metastatic cancer from primary sites to the brain affects the biochemistry of the cancers, with all metastatic brain tissue spectra having similar chemistry when in the brain. However, the mean breast cancer tissue spectrum and the corresponding metastatic brain tissue spectrum appear relatively similar to one another. The PCA scores plot also shows no separation between the primary and Metastatic breast spectra therefore, suggesting that there is no real change from primary and Metastatic breast tissue. The spectral differences between Colon/Rectum cancer tissue and the metastatic brain tissue are not large and vary mainly through differences in peak intensities. The primary site tissue spectrum exhibits much higher intensity peaks than the spectrum of metastatic brain tissue. The spectral differences between oesophagus and stomach tissue and metastatic brain tissue are far more obvious than between the spectra of the other cancers. The most noticeable disparity between the two average spectra is due to the peak at 1621 cm^{-1} , which is much more intense in the primary site spectrum than the metastatic brain spectrum. Furthermore, the amide I peak, at 1658 cm^{-1} , is much less intense in the primary site spectrum than the metastatic brain spectrum which produces an unusual ratio between the two peaks. Also, a peak at $\sim 796\text{ cm}^{-1}$ is displayed in the primary site spectrum but is not present in the spectrum of metastatic brain. For melanoma tissue, the spectral differences between melanoma primary site and metastatic tissue are primarily due

spectral differences seen from the amide I peak, the amide III and peaks present between 850 - 950 cm^{-1} .

Conclusion

In this study, we have demonstrated the use of immersion Raman spectroscopy to differentiate between GBM, metastatic and normal brain tissue with sensitivities and specificities of 100% and 94.44% respectively for GBM, 96.55% and 100% respectively for metastatic brain, and 85.71% and 100% respectively for normal brain tissue, based on the intensity ratios between the 721/782 cm^{-1} peaks. This shows that the Raman spectral peaks at 721 and 782 cm^{-1} , primarily associated with the symmetric C-N stretch of choline and the cytosol/uracil ring breathing of nucleotides respectively, may be possible spectral biomarkers for the discrimination of normal, GBM and Metastatic tissue. As well as this, PC-LDA was performed on the tissue spectra producing good separation of GBM, Metastatic and normal tissue spectra, again highlighting the potential of the analytical technique for the classification of cancerous tissue. As well as investigating GBM, Metastatic and normal tissue spectra, this study has also been able to distinguish some of the different primary site cancerous tissue and the different Metastatic brain cancerous tissue, based on the Raman spectra recorded. Being able to distinguish Metastatic brain tissue origins based on recorded Raman spectra, coupled with supervised multivariate analysis, would be non-subjective, therefore, the analytical technique could be used as a qualitative tool alongside neuropathology for disease diagnosis. For the first time the chemistry of Metastatic brain and their corresponding primary site tissue have also been investigated in this study by Raman spectroscopy, with primary Colon/Rectum, primary Melanoma and primary Oesophagus and Stomach tissue all being separated from their representative Metastatic brain tissue in PCA scores space, plus, significant mean spectral differences

were observed. Interestingly, this suggests that in some cases, that the movement of metastatic cancer from primary sites to the brain effects the biochemistry of the cancers, with metastatic cancerous tissue found in the brain becoming biochemically similar due to the new environment.

Acknowledgements

The authors would like to acknowledge the support of the Sydney Driscoll Neuroscience Foundation, Rosemere Cancer Foundation, Brain Tumour North West, the Centre for Materials and Science at the University of Central Lancashire, the Focas Institute at Dublin Institute of Technology, the European Community Action Scheme for the Mobility of University Students and the Association of British Spectroscopists. The Focas Research Institute is supported through the National Biophotonics and Imaging Platform (NBIP) Ireland funded under the Higher Education Authority PRTLII (Programme for Research in Third Level Institutions) Cycle 4, co-funded by the Irish Government and the European Union.

References

1. Cancer Research UK. *All cancers combined key facts*. 2012 [15/04/2013]; Available from: <http://www.cancerresearchuk.org/cancer-info/cancerstats/keyfacts/Allcancerscombined/>.
2. Richards, G.M., D. Khuntia, and M.P. Mehta, Therapeutic management of metastatic brain tumors. *Critical Reviews in Oncology/Hematology*, 2007. **61**(1): p. 70-78.
3. Brain Research Trust. *About Brain Tumours*. [cited 2012 08/10]; Available from: <http://www.brt.org.uk/brain-tumours>.
4. Soffieti, R., P. Cornu, J. Y. Delattre, R. Grant, F. Graus, W. Grisold, J. Heimans, J. Hildebrand, P. Hoskin, M. Kallijo, P. Krauseneck, C. Marosi, T. Siegal and C. Vecht, Brain Metastases. *European Handbook of Neurological Managments*, 2nd ed. (eds: N. E. Gilhus, M. P. Barnes and M. Brainin), 2011. **1**: p. 437-445.
5. Bergner, N., B.F.M. Romeike, R. Reichart, R. Kalff, C. Krafft, and J. Popp, Raman and FTIR microspectroscopy for detection of brain metastasis. *Clinical and Biomedical Spectroscopy and Imaging II*, 2011: p. 80870X-80870X.
6. Mahadevan-Jansen, A. and R.R. Richards-Kortum, Raman spectroscopy for the detection of cancers and precancers. *Journal of Biomedical Optics*, 1996. **1**(1): p. 31-70.
7. Krafft, C., S.B. Sobottka, G. Schackert, and R. Salzer, Analysis of human brain tissue, brain tumors and tumor cells by infrared spectroscopic mapping. *Analyst*, 2004. **129**(10): p. 921-925.
8. Raab, S.S., D.M. Grzybicki, J.E. Janosky, R.J. Zarbo, F.A. Meier, C. Jensen, and S.J. Geyer, Clinical impact and frequency of anatomic pathology errors in cancer diagnoses. *Cancer*, 2005. **104**(10): p. 2205-13.
9. Ellis, D.I., and R. Goodacre, Metabolic fingerprinting in disease diagnosis: biomedical applications of infrared and Raman spectroscopy. *Analyst*, 2006. **131**: p. 875-885.
10. Choo-Smith, L.P., H.G.M. Edwards, H.P. Endtz, J.M. Kros, F. Heule, H. Barr, J.S. Robinson, H.A. Bruining, and G.J. Puppels, Medical applications of Raman spectroscopy: From proof of principle to clinical implementation. *Biopolymers*, 2002. **67**(1): p. 1-9.
11. Moros, J., S. Garrigues, and M. de la Guardia, Vibrational spectroscopy provides a green tool for multi-component analysis. *TrAC Trends in Analytical Chemistry*, 2010. **29**(7): p. 578-591.
12. Gajjar, K., L. D. Heppenstall, W. Pang, K. M. Ashton, J. Trevisan, I. I. Patel, V. Llabjani, H. F. Stringfellow, P. L. Martin-Hirsch, T. Dawson and F. L. Martin, Diagnostic segregation of human brain tumours using Fourier-transform infrared and/or Raman spectroscopy coupled with discriminant analysis. *Analytical Methods*, 2012.
13. Krafft, C., S.B. Sobottka, G. Schackert, and R. Salzer, Raman and infrared spectroscopic mapping of human primary intracranial tumors: a comparative study. *Journal of Raman Spectroscopy*, 2006. **37**(1-3): p. 367-375.
14. Huang, Z., A. McWilliams, H. Lui, D. I. McLean, S. Lam and H. Zeng,, Near-infrared Raman spectroscopy for optical diagnosis of lung cancer. *International Journal of Cancer*, 2003. **107**(6): p. 1047-1052.
15. Teh, S.K., W. Zheng, K.Y. Ho, M. Teh, K.G. Yeoh, and Z. Huang, Near-infrared Raman spectroscopy for early diagnosis and typing of adenocarcinoma in the stomach. *British Journal of Surgery*, 2010. **97**(4): p. 550-557.
16. Bergholt, M.S., W. Zheng, K. Lin, K.Y. Ho, M. Teh, K.G. Yeoh, J.B. Yan So, and Z. Huang, In vivo diagnosis of gastric cancer using Raman endoscopy and ant colony optimization techniques. *International Journal of Cancer*, 2011. **128**(11): p. 2673-80.
17. Lieber, C.A., S.K. Majumder, D.L. Ellis, D.D. Billheimer, and A. Mahadevan-Jansen, In vivo nonmelanoma skin cancer diagnosis using Raman microspectroscopy. *Lasers in Surgery and Medicine*, 2008. **40**(7): p. 461-467.

18. Lin, K., D.L.P. Cheng, and Z. Huang, Optical diagnosis of laryngeal cancer using high wavenumber Raman spectroscopy. *Biosensors and Bioelectronics*, 2012. **35**(1): p. 213-217.
19. Abramczyk, H., J. Surmacki, B. Brożek-Płuska, Z. Morawiec, and M. Tazbir, The hallmarks of breast cancer by Raman spectroscopy. *Journal of Molecular Structure*, 2009. **924–926**(0): p. 175-182.
20. Moreno, M., L. Raniero, E.A.L. Arisawa, A.M. do Espirito Santo, E.A.P. dos Santos, R.A. Bitar, and A.A. Martin, Raman spectroscopy study of breast disease. *Theoretical Chemistry Accounts*, 2009.
21. Kanter, E.M., E. Vargis, S. Majumder, M.D. Keller, E. Woeste, G.G. Rao, and A. Mahadevan-Jansen, Application of Raman spectroscopy for cervical dysplasia diagnosis. *Journal of Biophotonics*, 2009. **2**(1-2): p. 81-90.
22. Lyng, F.M., E.Ó. Faoláin, J. Conroy, A.D. Meade, P. Knief, B. Duffy, M.B. Hunter, J.M. Byrne, P. Kelehan, and H.J. Byrne, Vibrational spectroscopy for cervical cancer pathology, from biochemical analysis to diagnostic tool. *Experimental and Molecular Pathology*, 2007. **82**(2): p. 121-129.
23. Crow, P., A. Molckovsky, N. Stone, J. Uff, B. Wilson, and L.M. WongKeeSong, Assessment of fiberoptic near-infrared raman spectroscopy for diagnosis of bladder and prostate cancer. *Urology*, 2005. **65**(6): p. 1126-1130.
24. Tollefson, M., J. Magera, T. Sebo, J. Cohen, A. Drauch, J. Maier, and I. Frank, Raman spectral imaging of prostate cancer: can Raman molecular imaging be used to augment standard histopathology? *British Journal of Urology International*, 2010. **106**(4): p. 484-488.
25. Stone, N., C. Kendall, J. Smith, P. Crow, and H. Barr, Raman Spectroscopy for identification of epithelial cancers. *Faraday Discussions*, 2004. **126**: p. 141-157.
26. Ó Faoláin, E., M.B. Hunter, J.M. Byrne, P. Kelehan, H.A. Lambkin, H.J. Byrne, and F.M. Lyng, Raman spectroscopic evaluation of efficacy of current paraffin wax section dewaxing agents. *Journal of Histochemistry and Cytochemistry*, 2005. **53**(1): p. 121-9.
27. Fullwood, L.M., D. Griffiths, K. Ashton, T. Dawson, R.W. Lea, C. Davis, F. Bonnier, H.J. Byrne, and M.J. Baker, Effect of substrate choice and tissue type on tissue preparation for spectral histopathology by Raman microspectroscopy. *Analyst*.
28. Bonnier, F., S.M. Ali, P. Knief, H. Lambkin, K. Flynn, V. McDonagh, C. Healy, T.C. Lee, F.M. Lyng, and H.J. Byrne, Analysis of human skin tissue by Raman microspectroscopy: Dealing with the background. *Vibrational Spectroscopy*, 2012. **61**(0): p. 124-132.
29. Bonnier, F., A. Mehmood, P. Knief, A.D. Meade, W. Hornebeck, H. Lambkin, K. Flynn, V. McDonagh, C. Healy, T.C. Lee, F.M. Lyng, and H.J. Byrne, In vitro analysis of immersed human tissues by Raman microspectroscopy. *Journal of Raman Spectroscopy*, 2011. **42**(5): p. 888-896.
30. Hands, J.R., P. Abel, K. Ashton, T. Dawson, C. Davis, R. Lea, A. McIntosh, and M. Baker, Investigating the rapid diagnosis of gliomas from serum samples using infrared spectroscopy and cytokine and angiogenesis factors. *Analytical and Bioanalytical Chemistry*, 2013: p. 1-9.
31. Baker, M.J., E. Gazi, M.D. Brown, J.H. Shanks, P. Gardner, and N.W. Clarke, FTIR-based spectroscopic analysis in the identification of clinically aggressive prostate cancer. *British Journal of Cancer*, 2008. **99**(11): p. 1859-1866.
32. Baker, M.J., E. Gazi, M.D. Brown, N.W. Clarke, J.C. Vickerman, and N.P. Lockyer, ToF-SIMS PC-DFA analysis of prostate cancer cell lines. *Applied Surface Science*, 2008. **255**(4): p. 1084-1087.
33. Huang, Z., X. Chen, Y. Chen, J. Chen, M. Dou, S. Feng, H. Zeng, and R. Chen, Raman spectroscopic characterization and differentiation of seminal plasma. *Journal of Biomedical Optics*, 2011. **16**(11): p. 110501-110501.
34. Sikirzhyski, V., K. Virkler, and I.K. Lednev, Discriminant analysis of Raman spectra for body fluid identification for forensic purposes. *Sensors (Basel)*, 2010. **10**(4): p. 2869-84.

35. Chan, J.W., D.S. Taylor, T. Zwerdling, S.M. Lane, K. Ihara, and T. Huser, Micro-Raman spectroscopy detects individual neoplastic and normal hematopoietic cells. *Biophysical Journal*, 2006. **90**(2): p. 648-56.
36. Feng, S., R. Chen, J. Lin, J. Pan, G. Chen, Y. Li, M. Cheng, Z. Huang, J. Chen, and H. Zeng, Nasopharyngeal cancer detection based on blood plasma surface-enhanced Raman spectroscopy and multivariate analysis. *Biosensors and Bioelectronics*, 2010. **25**(11): p. 2414-2419.
37. Tan, C.H. and E.H. Tan, Post-treatment Assessment of Glioblastoma Multiforme: Imaging with Fluorodeoxyglucose, Sestamibi, and Choline. *World J Nucl Med*, 2012. **11**(1): p. 30-2.
38. Aksoy, C. and F. Severcan, Role of Vibrational Spectroscopy in Stem Cell Research. *Spectroscopy: An International Journal*, 2012. **27**(3).
39. Notingher, I., Raman Spectroscopy Cell-based Biosensors. *Sensors (Basel)*, 2007. **7**(8): p. 1343-1358.
40. Gniadecka, M., P.A. Philipsen, S. Sigurdsson, S. Wessel, O.F. Nielsen, D.H. Christensen, J. Hercogova, K. Rossen, H.K. Thomsen, R. Gniadecki, L.K. Hansen, and H.C. Wulf, Melanoma Diagnosis by Raman Spectroscopy and Neural Networks: Structure Alterations in Proteins and Lipids in Intact Cancer Tissue. *Journal of Investigative Dermatology*, 2004. **122**(2): p. 443-449.
41. Zhang, X., W. Zhang, W.D. Cao, G. Cheng, and Y.Q. Zhang, Glioblastoma multiforme: Molecular characterization and current treatment strategy (Review). *Exp Ther Med*, 2012. **3**(1): p. 9-14.
42. Yamada, T., N. Miyoshi, T. Ogawa, K. Akao, M. Fukuda, T. Ogasawara, Y. Kitagawa, and K. Sano, Observation of molecular changes of a necrotic tissue from a murine carcinoma by Fourier-transform infrared microspectroscopy. *Clin Cancer Res*, 2002. **8**(6): p. 2010-4.

Figure and Table Legends

Appendix 4 - A manuscript submitted to 'Analyst' entitled 'Effect of Substrate Choice and Tissue Type on Tissue Preparation for Spectral Histopathology' written based on findings during this MSc (by research).



Effect of Substrate Choice and Tissue Type on Tissue Preparation for Spectral Histopathology by Raman Microspectroscopy

Journal:	<i>Analyst</i>
Manuscript ID:	AN-ART-09-2013-001832.R1
Article Type:	Paper
Date Submitted by the Author:	n/a
Complete List of Authors:	<p>Fullwood, Leanne; University of Central Lancashire, Division of Chemistry Griffiths, David; University of Central Lancashire, School of Pharmacy and Biomedical Sciences Ashton, Katherine; Royal Preston Hospital, Pathology Dawson, Timothy; Royal Preston Hospital, Pathology Lea, Robert; University of Central Lancashire, School of Pharmacy and Biomedical Sciences Davis, Charles; Royal Preston Hospital, Pathology Bonnier, Franck; Dublin Institute of Technology, Focas Research Institute Byrne, Hugh; Focas Institute, Dublin Institute of Technology Baker, Matthew J; University of Central Lancashire, Division of Chemistry</p>



INVESTOR IN PEOPLE



University of Central Lancashire

Dr Matthew J Baker

Senior Lecturer in Toxicology and Analytical Chemistry

School of Forensic & Investigative Sciences

University of Central Lancashire

Preston PR1 2HE

Tel: (Office) 01772 893209

email: mjbaker@uclan.ac.ukwww.uclan.ac.uk

Dear Sir or Madam

Please accept this as a cover letter for my submission of a research paper entitled “**Effect of Substrate Choice and Tissue Type on Tissue Preparation for Spectral Histopathology**”

This paper reports, for the first time, the influence of substrate choice and tissue type on the sample preparation of tissue for the dynamic field of spectral histopathology. This is truly a timely manuscript as there is much debate within the field concerning substrate choice. We show results describing a novel phenomenon of substrate interaction with paraffin that has previously not been reported elsewhere and show a disparity between the paraffin retention of tissue based upon histological types.

I feel your audience will be interested and enlightened by these findings and the methodological approach taken. I hope that this paper will communicate this interesting research area directly to the biomedical Spectroscopists and wider audience that your journal has. I expect that this paper will be a driver for further research into sample preparation for spectral histopathology

Please do not hesitate to get in touch if you have any questions or queries as I would relish any opportunity to discuss this research with you or your editorial board.

Yours faithfully

Dr Matthew J Baker





INVESTOR IN PEOPLE



University of Central Lancashire

Dr Matthew J Baker

Senior Lecturer in Toxicology and Analytical Chemistry

School of Forensic & Investigative Sciences

University of Central Lancashire

Preston PR1 2HE

Tel: (Office) 01772 893209

email: mjbaker@uclan.ac.ukwww.uclan.ac.uk

Dear Editorial Team,

We would like to thank the reviewers for their time taken in reviewing the article. Please find my answers to specific points raised by each reviewer below, all changes are highlighted in the paper in red.

Referee: 1

Comments to the Author

The authors use Raman microspectroscopy in order to detect the level of paraffin retained in thin sections from different types of cancerous tissues (mainly brain) after dewaxing. They compare the level of paraffin retained by tissues on 3 different substrates (CaF₂, quartz, low-e glass) and by 4 different tissue types (normal brain, metastatic, primary brain tumour and glioblastoma). They make several claims: paraffin retention depends on the type of substrate and is lower on low-e slides; paraffin retention is higher in cancerous tissue than in normal tissue. They tentatively link this higher paraffin retention to cancerous tissue density. Some of these findings are new. Although not of primary importance, they can be useful to the bio-analytical community.

Some results presented in this paper – the composition of the substrates – are clearly not new and could be removed.

As advised, the section on composition of the substrates has been removed.

Some results are not accurately reported – the level of paraffin retention in tissues – and should be significantly extended, and some data are lacking. More importantly, some findings cannot be substantiated by the provided data.

We have attempted to address this general comment under the more specific points below.

The paper is clearly written but a few points need to be clarified:

- There is a discrepancy in the number of samples in the Experimental and results sections (29 vs 31 metastatic patients)

This has been changed in the text. The number of metastatic patients is 29

- In Table 1, one of the patients is supposedly born in 2025; this is clearly an achievement in early





diagnosis ;-)

Apologies, Table 1 has been revised

Dewaxing Efficiency by Substrate Type

Please note that a title for the first section of the results is lacking.

The title “Dewaxing Efficiency by Substrate Type” has been added to the manuscript

The findings that low-e slides retain less paraffin than CaF₂ and quartz is new and may be of interest for the wider biospectroscopist community. However, the authors state that “the adherence to current clinical process will be advantageous”. It could be suggested that adherence to clinical practice requires the use of glass slides (that can not be used for infrared but can be used for Raman. The authors should describe why normal glass was not included in their study. Is it due to the incompatibility between glass and their laser frequency? If so this laser choice should be explained.

When Raman spectroscopy is performed on Glass, there is a large fluorescent background within the region where the peaks of interest are contained. Low e slides, the same size as glass slides, were used due to their similarity, low cost and the ease with which they could be substituted for glass in clinical processes. The following has been added to the introduction:

“Commercial glass microscope slides exhibit a very large fluorescent background under excitation in the near infra red, and are thus not suitable. Therefore, common spectroscopy substrates currently used include quartz, CaF₂ and low-E microscope slides, the latter being relatively low cost.^{28,,}”

Although paraffin adhered more to CaF₂ and quartz than to low-e slides with the dewaxing protocol used in this study, it would be of great interest if the authors would discuss or investigate whether longer/more stringent dewaxing procedures would result in better dewaxing on these substrates. Especially since authors stated in the introduction that alternative dewaxing protocols (hexane) can be more efficient.

The text has been modified to include “An important advantage in using spectroscopy for diagnosis is the short diagnostic window; therefore, a dewaxing solvent that requires a long processing time period is not an attractive option for this field of study”

....

The SEM/EDX results obtained on quartz, low-e slides and CaF₂ are clearly not new and should be removed. There is no knowledge gained in showing that quartz and glass are made of Si and O, and that CaF₂ is made of Ca and F. The AFM experiments are relevant to the problem.

The SEM/EDX results have been removed from the manuscript

Spectral Histopathology: Dewaxing Efficiency by Tissue Types

First, the reporting of this finding is clearly lacking as there is no numerical data, only 3 averaged spectra are provided, and readers are given no mean to estimate the variability of the paraffin signal



within each group. Quantitative data should be reported with standard deviations or other means to judge the variability of the data.

A further Figure (Figure 8) has been added to the manuscript.

The legend below has been added to the figure and manuscript

“Figure 8. The average intensity and standard deviation of three intense paraffin peaks at 1061, 1131 and 1294 cm^{-1} for the three tissue types; Normal tissue (blue), Glioblastoma multiforme (red) and Metastatic brain cancer (green)”

The manuscript has been changed to read

“Figure 8 shows the average intensity and standard deviation of the intense paraffin peaks at 1061, 1131 and 1294 cm^{-1} . As can be seen, there is a trend to greater paraffin retention in normal to the cancerous states, metastatic tissue retaining the most paraffin, after the same processing procedures. Further imaging studies are planned to examine the impact of the substrate upon paraffin retention, as there seems to be an interplay of tissue dependence and substrate dependence where the paraffin clumps upon the substrate surface, as can be seen in Figure 5.”

Second, only 2 types of brain cancer are compared with normal tissue in Figure 10 while 3 types of tumours (GBM, metastatic and primary) are described in the Experimental section. The results from primary brain tumours must be given.

The reference to primary tumours has been removed from the experimental section for ease of understanding. The primary brain tumours (GBM) are already shown in the results. The primary tumours previously referred to in the experimental section are the original tumour sites of the metastatic brain tumours and hence were different tissue (i.e. breast) and were not suitable for the comparison of paraffin retention.

Third, the protocol is not adapted to show a correlation between paraffin signal and pathological status because it doesn't measure the paraffin signal accurately and because the spectra were recorded on CaF2 windows which – as shown by the authors – are a cause of paraffin retention. The study should be made on low-e slides to minimise retention from the slide. The authors used either 100X or 60X immersion objectives and a 785nm laser, the laser spot size at sample must be in the micron range although no information is given in experimental section.

The text has been modified in the section, Experimental: Raman spectroscopy instrumentation and analysis

“Point spectra were acquired using a x 100 (Olympus MPlanN, NA = 0.9, spotsize ~1 μm) objective and immersion point spectra were taken using a x 60 (Olympus LUMPlanFLN, NA = 1.0, spotsize ~ 1.5 μm) objective.”

They report recording around 22 spectra per sample. This low sampling can not accurately measure the quantity of paraffin in sections of several square millimeters, even less so since some sample are highly

heterogeneous (Figure 1) and may accumulate different paraffin levels in different regions. To substantiate the claim of higher retention by cancerous tissues, it would require measuring the amount of paraffin retained in representative area of the sections maybe using an infrared imager to quickly collect images on several square millimeters.

The aim was not to quantify the paraffin within several square millimetres of section, as the reviewer correctly states, and this would most likely require an FTIR equipped with an FPA. Rather, this study targeted cancerous areas of tissue and examined non-cancerous tissue from multiple patients and it was discovered that the paraffin retention is different between cancerous and non-cancerous tissue.

In addition, the results presented by the authors in the first part of the paper suggest that the level of paraffin retention is a feature of the slide surface roughness that may vary locally on a window, may also vary on different CaF₂ windows, and from batch to batch.

The manuscript has been changed to read “The substrates had not been used for prior investigations and were fresh for this study. The measurements were taken from multiple slides and multiple places on each slide so batch to batch variability should not affect the trends in the data shown.”

The level of paraffin may be higher in the metastatic tumor sample due to the simple fact that their architecture is different and that the dewaxing procedure is less efficient than in the other samples. This is not discussed.

The reviewer is correct and indeed we had attempted to make this point in the discussion. For clarity, the text has been amended to read:

“Abnormal tissue can be of very different morphology than normal tissue. A difference in tissue density could provide an explanation for the inconsistency of the dewaxing efficiency, and thus the variation of paraffin peak intensity between the normal brain and cancerous brain tissue spectra.”

The tentative explanation given in the Discussion section fails to convince as extending findings on breast tumour to brain tumours appears arbitrary, and data linking brain tissue density to tumorous status are not provided. These results are thus clearly not substantiated and should be removed from the paper.

We accept the reviewers point and as such the manuscript has been changed to provide a more relevant argument.

“Berrtholdo *et al.* correlate increased choline signals from Magnetic Resonance Spectroscopy as a measure of malignancy in brain tumours due to increased glial cell density as choline is a marker of cellular membrane turnover reflecting cellular proliferation³⁸. Therefore, the disparity of wax retention between normal and cancerous tissue evident in figure 7 can be proposed to be due to local differences in tissue density.

In the discussion it is stated that for breast tissue “state that the amount of fibro-glandular and adipose tissue is strongly related to the risk of developing cancer”. The proposed method for dewaxing eliminates all fat from tissues including myelin from axons and probably modifies protein through precipitation and hydrolysis, potentially destroying useful information for spectroscopic diagnosis. This should be discussed and the advantages of “computationally” dewaxing tissue section spectra as shown by the work of Sockalingum, Gobinet, Manfait and al. should be discussed.

The following text has been added to the discussion

“The results indicate that tissue processing still remains an issue for Spectropathology, particularly using Raman spectroscopy. For clinical relevancy, however, and indeed acceptance of the techniques by the clinical community, it is important that the sample preparation and measurement protocols for Raman spectroscopic analyses are consistent with current clinical practice. Choice of substrate for routine clinical analyses may be dominated by economic considerations, thus favouring low E slides. Paraffin embedding facilitates tissue cutting, but also is commonly employed, worldwide, for archiving tissue samples. The availability of a wide range of pathologically characterized samples for study potentially enables extensive retrospective studies using spectroscopic and other techniques. The embedding process and wax itself can, however, contribute significantly to the spectroscopic signature of the tissue ⁴⁰. An alternate method of “digital dewaxing” biological specimens to remove paraffin contributions of the spectrum has been proposed by Gobinet *et al.*, recognising that chemical dewaxing methods are known to be inefficient for the complete removal of wax in tissue and can cause alterations to the samples. Their method of dewaxing consists of an estimation of the paraffin sources in the spectrum using Independent Component Analysis (ICA), followed by a Non-negatively Constrained Least Squares (NCLS) method to subtract the contributions. This enables removal of the paraffin signals to allow analysis of the underlying tissue spectrum ³³. However, although “digital dewaxing” has been demonstrated⁴¹, it is also often important to compare spectroscopic profiling with parallel histological analyses, requiring chemical dewaxing of sections, a process which adds to the sample variability. The observation of variable dewaxing efficiencies depending on tissue pathology adds complexity to the challenge, perhaps requiring a combination of established clinical dewaxing protocols with computational procedures.”

Referee: 2

Comments to the Author

Dear Authors,

The submission addresses very fundamental issues in vibrational spectroscopy. The work presented is succinct and to the point. Excluding minor typos and omissions, listed below, I recommend the text for publication.

1) Pg. 8 - World Health Organization, name of the organization

This has been changed in the manuscript and W, H and O has been capitalised

2) Pg. 8 - haemotoxylin and eosin, name of chemicals

This has been changed in the manuscript, h and e are now not capitalised

3) Pg. 8 - HistoClear, trade name of chemical

This has been changed in the manuscript H and C are now capitalised

4) Pg. 9 - EM CCD, electron multiplying CCD

This has been changed in the manuscript

5) The formatting of company affiliation is not consistent throughout the text

This has been changed in the manuscript

Referee: 3

Comments to the Author

In the context of spectral histopathology, this article studies by Raman spectroscopy the influence of the substrate choice and of the analyzed tissue type on the efficacy of chemical dewaxing. This work is innovative and addresses a problem that was never pointed out before. However, this article leads to minor and major comments and questions.

1) The title is not enough specific. The authors should precise that the study is realized using Raman spectroscopy.

The title has been changed to read

Effect of Substrate Choice and Tissue Type on Tissue Preparation for Spectral Histopathology by Raman Microspectroscopy

2) The introduction is ambiguous because infrared and Raman spectroscopy are mixed throughout. Thus, I thought that the two techniques would be used in the rest of the paper. The authors thus should justify the construction of their introduction or should change their introduction in order to focus on Raman spectroscopy.

A paragraph has been added to the introduction in answer to this comment. The text now reads

“The contribution of paraffin peaks in vibrational spectra is apparent in both infrared and Raman spectroscopy. However, these peaks appear more prominently in the spectra of the latter technique; thus, Raman spectroscopy was used in this study to analyse the efficacies of current dewaxing techniques.”

3) The ambiguity of the introduction is also illustrated by its first paragraph which focuses on prostate cancer. Thus, I thought that the study would be based on prostate tissues. Why not constructing this paragraph on brain cancer?

A sentence has been added and the manuscript now reads “There have been many studies of different pathologies but the issues are well demonstrated by the example of prostate cancer.”

4) In page 6 of the received manuscript, the sentences "O Faolain et al. suggest that the complete removal of paraffin from the tissue section is not possible to assess accurately with FTIR spectroscopy using the ~1462 cm⁻¹ signal and should be performed using Raman spectroscopy. This was concluded following analysis of Raman and FTIR spectra obtained from identically deparaffinised tissue sections in which spectral peaks characteristic of paraffin wax were more clearly resolved in Raman spectra (strong sharp bands), compared with FTIR spectra" are almost entirely copied/pasted from a sentence of the reference [26] of Lyng et al. Authors should personalize these sentences.

The manuscript has been changed to read

“Ó Faoláin *et al.* indicate that Raman spectroscopy is much more sensitive to assess the incomplete removal of wax than FTIR”

5) Furthermore, the authors refer to reference [26] of Lyng et al. for these sentences. However, these sentences summarize the work of Faolain et al. in the following article, which should be added in the

reference part of the paper:

E.O. Faolain, M.B. Hunter, J.M. Byrne, P. Kelehan, M. McNamara, H.J. Byrne, F.M. Lyng, A study examining the effects of tissue processing on human tissue sections using vibrational spectroscopy, *Vibrational Spectroscopy*, 38, 121-127, 2005.

The reference has been added

6) Page 7, authors write that "CaF₂ has been shown to be better for Raman measurements". Should they provide references proving this claim?

The following reference has been added to support the comparison of substrates:

" Collagen matrices as an improved model for in vitro study of live cells using Raman microspectroscopy", F. Bonnier, P. Knief, A. D. Meade, J. Dorney, K. Bhattacharya, F. M. Lyng and H. J. Byrne, *Clinical and Biomedical Spectroscopy and Imaging II*, edited by Nirmala Ramanujam, Jürgen Popp, *Proc. of SPIE-OSA Biomedical Optics*, SPIE Vol. 8087, 80870F (2011)

7) Are the sections for H&E staining and Raman acquisition directly adjacent?

The manuscript has been changed to read "The tissue sections used from each sample were cut consecutively with one section used for Raman analysis and one for haematoxylin and eosin staining"

8) Why didn't the author consider in their study glass substrate since it is classically used in clinical routine?

When Raman spectroscopy is performed on Glass there is a large fluorescent background within the region where the peaks of interest are contained. Low e slides the same size as glass slides were used due to their similarity and the ease with which they could be substituted for glass in clinical processes. The text has been amended to read:

"Commercial glass microscope slides exhibit a very large fluorescent background under excitation in the near infra red, and are thus not suitable. Therefore, common spectroscopy substrates currently used include quartz, CaF₂ and low-E microscope slides, the latter being relatively low cost."

Note: This question was also raised by reviewer 1 and thus the amended text is highlighted in red

9) In E.O. Faolain et al, *Vibrational Spectroscopy*, 38, 2005, normal parenchymal tissue from the placenta was chosen because it is an homogenous tissue. What are the arguments of the authors to explain their choice to analyze brain tissues?

The authors use brain tissue as this work is part of a larger study on the use of spectral histopathology for the diagnosis and detection of brain tumours.

10) In reference [25], E.O. Faolain et al showed that hexane is a more effective dewaxing agent than HistoClear. Thus, why did the authors prefer to use HistoClear?

HistoClear is the clinical standard and the authors used HistoClear in order to assess the current clinical practices and their use within the developing field of spectral histopathology.

The text has been modified to clarify

“An important advantage in using spectroscopy for diagnosis is the short diagnostic window; therefore, a dewaxing solvent that requires a long processing time period is not an attractive option for this field of study.”

Note: This question was also raised by reviewer 1 and thus the amended text is highlighted in red

11) In page 9, in the "Raman spectroscopy instrumentation and analysis" section, authors write "immersion point spectra". What does it mean and for which acquisitions was it used?

The following text has been added to the manuscript

Immersion spectroscopy was used for measurement of the tissue samples for spectral histopathology. Immersion Raman utilises an immersion lens which is in direct contact with a liquid that the sample under analysis is submerged in, such as deionised water used in this study. Bonnier *et al.* describe the use of immersion Raman spectroscopy and demonstrate its successful use for improving spectral quality^{34,35}.

12) The authors should precise the average number of Raman spectra acquired on each section.

The manuscript has been changed to read

“From each tissue section 20 spectra were acquired from different regions, depending upon the size of the tissue slice.”

13) For normal tissue, on which structures did the authors make the acquisitions: white matter, gray matter, ...? These structures having different densities, have the authors analyzed the influence of the type of analyzed structure for the same section on the dewaxing procedure efficacy? The same questions are asked for the tumoral tissues.

For normal tissue, an approach to the spectral acquisition was taken as it would be in the clinic. i.e all and any normal tissue was analysed. The trends seen therefore are across all the structure of normal brain analysed as no particular area was targeted. As for tumoral sections, these are all cancerous areas and were not analysed according to the origin of the structure, again mimicking clinical practice.

The trends seen are therefore general trends linked to the retention by the vastly different tissue types of normal, high grade cancer and metastatic.

The following text has been added in the experimental section

For all tissue samples, sample analysis by spectral acquisition was carried out as it would be in the clinic. i.e all and any normal tissue was analysed, and no particular area was targeted (eg white/grey matter). Similarly, for tumoral sections, all cancerous areas were analysed irrespective of the origin of the structure, again mimicking clinical practice.

14) In page 10, in the "Data pre-processing" section, the authors should provide a reference or explain the method used to subtract the background.

The manuscript has been changed to read

“background subtraction was performed through the application of a fifth order polynomial and smoothed using 7 point smoothing”

15) In page 10, in the "Data pre-processing" section, I do not understand the sentence "using the cytospec code written by Dr A Henderson" since CytoSpec has been developed by Peter Lasch. Who is A Henderson and what is his link with CytoSpec and this article?

The manuscript has been changed to read “using in-house written code”

16) In page 11, in the "Results and discussion" section, what is the aim of the microscopic observation of the substrate surface? What information is supplied by right panel images of figures 3, 4 and 5? Are these figures necessary since they are not commented in the results?

These figures have been removed on recommendation of Reviewer 1.

17) In page 13, in the "Results and discussion" section, the authors should compare their results (complete dewaxing on low-E MirrIR slide) to those obtained by Faolain et al, Vibrational Spectroscopy, 38, 2005 (incomplete dewaxing on MirrIR slide).

The study by O Faoláin et al., was conducted under somewhat different circumstances (dewaxing protocol, tissue type). Nevertheless a comment has been added to the Results and discussion.

“Indeed, it should be noted that, whereas in this study complete removal of wax was observed for tissue samples on low-E slides, O’ Faoláin et al.³⁹ reported incomplete was removal from normal parenchymal tissue from the placenta, dewaxed using a xylene based protocol also measured in low-E slides.”

18) The subsection title "Spectral histopathology: Dewaxing efficiency by tissue types" is useless since no such subsection title was provided for the first part of the "Results and discussion" section.

A title has been added to the first part of the section

19) Compared to the first part of the "Results and discussion" section, the second part concerning the study of the dewaxing efficiency by tissue types is very light. It mainly consist of the observation that normal tissues are better dewaxed than tumoral ones. Isn't it possible to demonstrate that tissue density is really responsible of this effect? What to conclude from this part of the study?

The discussion has been added to with reference to the previous studies on parenchymal tissue from the placenta as well as further evidence of higher densities in brain tumours, allowing a stronger statement on dependence of dewaxing efficacy on tissue density.

Berrtholdo *et al.* correlate increased choline signals from Magnetic Resonance Spectroscopy as a measure of malignancy in brain tumours due to increased glial cell density as choline is a marker of cellular membrane turnover reflecting cellular proliferation³⁸. Therefore, the disparity of wax retention between normal and cancerous tissue evident in figure 7 can be proposed to be due to local differences in tissue density.

Note: This question was also raised by reviewer 1 and thus the amended text is highlighted in red

20) On the one hand, the low-E MirrIR slide induces a perfect dewaxing of samples. On the other hand, CaF2 leads to incomplete dewaxing. In function of the type of tissue, the paraffin residue is variable, and thus CaF2 induces more discriminative information between different types of tissues thanks to paraffin residue. What is thus the position of the authors concerning the slide to choose for Raman analysis of FFPP samples?

A further paragraph has been added to the Discussion section

“The results indicate that tissue processing still remains an issue for Spectropathology, particularly using Raman spectroscopy. For clinical relevancy, however, and indeed acceptance of the techniques by the clinical community, it is important that the sample preparation and measurement protocols for Raman spectroscopic analyses are consistent with current clinical practice. Choice of substrate for routine clinical analyses may be dominated by economic considerations, thus favouring low E slides. Paraffin embedding facilitates tissue cutting, but also is commonly employed, worldwide, for archiving tissue samples. The availability of a wide range of pathologically characterized samples for study potentially enables extensive retrospective studies using spectroscopic and other techniques. The embedding process and wax itself can, however, contribute significantly to the spectroscopic signature of the tissue⁴⁰. An alternate method of “digital dewaxing” biological specimens to remove paraffin contributions of the spectrum has been proposed by Gobinet *et al.*, recognising that chemical dewaxing methods are known to be inefficient for the complete removal of wax in tissue and can cause alterations to the samples. Their method of dewaxing consists of an estimation of the paraffin sources in the spectrum using Independent Component Analysis (ICA), followed by a Non-negatively Constrained Least Squares (NCLS) method to subtract the contributions. This enables removal of the paraffin signals to allow analysis of the underlying tissue spectrum³³. However, although “digital dewaxing” has been demonstrated⁴¹, it is also often important to compare spectroscopic profiling with parallel histological analyses, requiring chemical dewaxing of sections, a process which adds to the sample variability. The observation of variable dewaxing efficiencies depending on tissue pathology adds complexity to the challenge, perhaps requiring a combination of established clinical dewaxing protocols with computational procedures.”

This section has also been added in response to a comment by Reviewer 1

21) Page 19, the authors should write "Figure 2" instead of "Figure 1"

Figure references have been corrected within the manuscript

22) Figures 3, 4 and 5 should be grouped together.

These figures have been removed from the manuscript

23) For figure 6, the averaged spectrum of low-E Mirr acquisitions is computed from 210 spectra, while around 450 are used for CaF₂ and Spectrosil acquisitions. Why this huge difference?

The spectra acquired are part of a larger study and as such there are different numbers of spectra for each substrate

24) For figure 7, the averaged spectrum acquired on low-E Mirr shows no paraffin spectral contribution. This spectrum is thus characteristic of low-E Mirr. Why is this spectrum different from the reference spectrum of low-E Mirr presented on figure 2?

Upon further inspection, the background has been standardised across the images

25) The authors should provide a scale bar for images provided on figures 1 and 8.

Scale bars have been added to these figures

26) To compare the spectra of figure 10 and to make conclusions, averaged spectra +/- standard deviation should be plotted.

A further Figure (Figure 8) has been added to the manuscript.

The legend below has been added to the figure and manuscript

“Figure 8. The average intensity and standard deviation of three intense paraffin peaks at 1061, 1131 and 1294 cm⁻¹ for the three tissue types; Normal tissue (blue), Glioblastoma multiforme (red) and Metastatic brain cancer (green)”

The manuscript has been changed to read

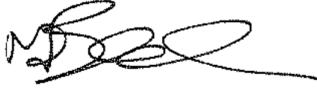
“Figure 8 shows the average intensity and standard deviation of the intense paraffin peaks at 1061, 1131 and 1294 cm⁻¹. As can be seen, there is a trend to greater paraffin retention in normal to the cancerous states, metastatic tissue retaining the most paraffin, after the same processing procedures. Further imaging studies are planned to examine the impact of the substrate upon paraffin retention, as there seems to be an interplay of tissue dependence and substrate dependence where the paraffin clumps upon the substrate surface, as can be seen in Figure 5.”

This section has also been added in response to a comment by Reviewer 1

27) In table 1, one patient was born in 2029 and another one in 2025.

This has been modified in the revised manuscript

Yours faithfully

A handwritten signature in black ink, appearing to read "M J Baker", with a long horizontal flourish extending to the right.

Dr Matthew J Baker

Effect of Substrate Choice and Tissue Type on Tissue Preparation for Spectral Histopathology by Raman Microspectroscopy

Leanne M. Fullwood¹, Dave Griffiths², Katherine Ashton³, Timothy Dawson³, Robert W. Lea², Charles Davis³, Franck Bonnier⁴, Hugh J. Byrne⁴, and Matthew J. Baker^{1*}

¹ Centre for Materials Science, Division of Chemistry, University of Central Lancashire, Preston, PR1 2HE, UK

² School of Pharmacy and Biomedical Sciences, University of Central Lancashire, Preston, PR1 2HE, UK

³ Lancashire Teaching Hospital NHS Trust Royal Preston Hospital, Sharoe Green Lane, Preston PR2 9HT, UK

⁴ FOCAS Research Institute, Dublin Institute of Technology, Kevin Street, Dublin 8, Ireland

*Corresponding Author: mjbaker@uclan.ac.uk

Abstract

Raman spectroscopy is a non-destructive, non-invasive, rapid and economical technique which has the potential to be an excellent method for the diagnosis of cancer and understanding disease progression through retrospective studies of archived tissue samples. Historically, biobanks are generally comprised of formalin fixed paraffin preserved tissue and as a result these specimens are often used in spectroscopic research. Tissue in this state has to be dewaxed prior to Raman analysis to reduce paraffin contributions in the spectra. However, although the procedures are derived from histopathological clinical practice, the efficacy of the dewaxing procedures that are currently employed is questionable. Ineffective removal of paraffin results in corruption of the spectra and previous experiments have shown that the efficacy can depend on the dewaxing medium and processing time. The aim of this study was to investigate the influence of commonly used spectroscopic substrates (CaF₂, Spectrosil quartz and low-E slides) and the influence of different histological tissue types (normal, cancerous and metastatic) on tissue preparation and to assess their use for spectral

histopathology. Results show that CaF_2 followed by Spectrosil contribute the least to the spectral background. However, both substrates retain paraffin after dewaxing. Low-E substrates, which exhibit the most intense spectral background, do not retain wax and resulting spectra are not affected by paraffin peaks. We also show a disparity in paraffin retention depending upon the histological identity of the tissue with abnormal tissue retaining more paraffin than normal.

Keywords Cancer, Diagnosis, Raman, Substrate, Histopathology, Vibrational Spectroscopy

Introduction

The primary requirement for successful treatment of any disease is early detection. Cancer incidence rates have continued to rise ¹, although survival rates for cancer are increased with early diagnosis. Current methods used in cancer diagnosis focus on changes in architecture of tissue, cells or internal constituents and the identification of protein expression. Research performed into identification of protein expression in blood has produced single biomarkers for specific cancers that have become misleading. *There have been many studies of different pathologies but the issues are well demonstrated by the example of prostate cancer.* The Prostate Specific Antigen (PSA) test is used to indicate prostate cancer (CaP). However, approximately 40 % of organ confined CaP show no elevation of PSA ² and many other benign conditions can show increased PSA serum, thus producing false positives in screening. Hoffman *et al.* suggest that CaP screening would benefit from improved biomarkers, which more readily identify clinically important cancers ³. As cancer is a heterogeneous disease, a set of markers or a whole sample profile will provide significantly more diagnostic information than any one marker ⁴. After initial indication of cancer, diagnosis is confirmed by biopsy and assessment of tissue architecture. The biopsy is assessed based upon a subjective measurement. For CaP this is called the Gleason grading system and in a study of 390 patients identical grades were assigned to only 29.2% of the tumours by different histopathologists ⁵. Pathological discrepancies are reported to occur in up to 43% of specimens assessed via histopathology ⁶. The accurate and rapid diagnosis of disease allows early intervention of appropriate treatment, thus increasing life expectancy and reducing healthcare costs ⁷. Therefore, there is a requirement for non-subjective techniques that can rapidly and accurately identify disease.

Spectroscopic techniques, such as Raman and Infrared (IR), are excellent methods for the analysis of a wide range of materials. They are non-destructive, rapid, cost-effective and simple to operate. The inelastic (Raman) scattered light from molecules under irradiation is wavelength-shifted with respect to the incident light by molecular vibrations. The Raman spectrum is complementary to that of IR which represents the absorption of incident light at the resonant frequency of the bond or group, exciting vibrational modes. Different biomolecules exhibit responses to different wavelengths of light; the resultant spectrum can be thought of as a 'fingerprint' of the sample. Spectroscopic analysis allows the objective classification of biological material on a molecular level⁸. Previous studies have demonstrated the use of spectroscopy (imaging and point spectra) to analyse gastrointestinal (GI) tract^{9, 10}, lung^{11, 12}, cervix^{13, 14}, brain^{15, 16}, breast^{17, 18}, prostate¹⁹⁻²¹ and lymph node cancers^{22, 23}. Initial work has focused on differentiating between normal tissue and advanced cancers. Technological development is enabling diagnosis at progressively earlier stages and potential to do so *in vivo*²⁴. The aim of these studies is to develop spectral histopathology based upon objective chemical information.

In order to develop spectral histopathology, a database of tissue spectra is required to enable spectral disease identification. The ideal situation would be to build this database using fresh or frozen tissue sections. However, historically, biobanks have been built using Formalin Fixed Paraffin Preserved Tissue (FFPP) sections, which are fixed using formalin and impregnated with paraffin wax to preserve the tissue for future analysis and provide support to aid microtomy for sectioning the tissue block to enable microscopic examination. Prior to histological and/or spectral analysis, the tissue sections generally undergo a

dewaxing process, to allow histological staining of the tissue for pathological examination and to reduce paraffin contributions in vibrational spectra, consequently, returning the tissue to as much of an *in vivo* state as possible ²⁵.

Ó Faoláin *et al.* investigated the efficacy of dewaxing procedures on formalin fixed, paraffin preserved (FFPP) cervical tissue on glass slides ²⁵. They reported that dewaxing procedures employing, the commonly used xylene and HistoClear solvents do not completely remove all of the paraffin wax. Although, they found hexane to be a much more efficient dewaxing agent, it requires 18 hours of tissue submersion and is not clinically used for dewaxing procedures ²⁵. An important advantage in using spectroscopy for diagnosis is the short diagnostic window; therefore, a dewaxing solvent that requires a long processing time period is not an attractive option for this field of study. Ó Faoláin *et al.* indicate that Raman spectroscopy is much more sensitive to assess the incomplete removal of wax than FTIR. This was concluded following analysis of Raman and FTIR spectra obtained from identically deparaffinised tissue sections in which spectral peaks characteristic of paraffin wax were more clearly resolved in Raman spectra (strong sharp bands), compared with FTIR spectra ²⁶.

The contribution of paraffin peaks in vibrational spectra is apparent in both infrared and Raman spectroscopy. However, these peaks appear more prominently in the spectra of the latter technique; thus, Raman spectroscopy was used in this study to analyse the efficacies of current dewaxing techniques.

Substrates are needed in spectral histopathology to support the samples during analysis. Samples are often relatively thin allowing incident light the opportunity of interacting with the substrate below. This interaction has an effect on the spectral

background; thus, the correct choice of substrate for spectroscopic analysis is essential for reducing this background and optimising the quality of the spectral data²⁷. Commercial glass microscope slides exhibit a very large fluorescent background under excitation in the near infrared, and are thus not suitable. Therefore, common spectroscopy substrates currently used include quartz, CaF₂ and low-E microscope slides, the latter being relatively low cost.²⁸

Recently, the choice of substrate has been a hot topic within the spectral histopathology field, as spectral artefacts have been identified in FTIR transfection analysis using highly reflective low-E slides^{29,30}. However, when analysing tissue, a 2nd derivative spectrum minimises these contributions allowing for spectral histopathological diagnosis³¹. Both quartz and CaF₂ are transparent over a large range of the mid-IR and are therefore suitable for transmission measurements, although CaF₂ has been shown to be better for Raman measurements, and so is an obvious choice for use of both complementary techniques. The choice of substrate is also important if spectral diagnoses are going to be effective in the clinical setting, substrates that can easily fit into current methodologies (due to size, solubility etc.) are advantageous and also cost needs to be minimised to ensure efficient health services.

Vibrational spectroscopy has the potential to revolutionise the clinical environment, allowing for increased efficiency within the diagnostic regime with corresponding decreases in mortality, morbidity and economic impact upon the health services³². In order to achieve this potential, research needs to be performed to understand the impact of sample preparation upon the vibrational spectrum. We present, for the first time, a study of the effect and efficiency of the dewaxing process, using a clinical standard HistoClear procedure, by

substrate and tissue type utilising Raman spectroscopy in order to develop the basis of standard approaches for spectral histopathology.

Experimental

Study participants

Tissue sections cut, by microtomy, at both 4 μm onto glass microscope slides and 10 μm onto spectroscopic substrates: low-E MirrIR slides (Kevley Technologies, Chesterland, OH, 44026, USA), Spectrosil quartz (Starna Scientific) and calcium fluoride (CaF_2) (Crystran), were obtained from formalin fixed paraffin preserved (FFPP) tissue blocks from the Brain Tumour North West (BTNW) bio-bank under ethical approval (BTNW/WRTB 13_01). The substrates had not been used for prior investigations and were fresh for this study. The measurements were taken from multiple slides and multiple places on each slide so batch to batch variability should not affect the trends in the data shown. The tissue sections used from each sample were cut consecutively with one section used for Raman analysis and one for haematoxylin and eosin staining. Patient data consisted of histological information, patient gender and date of birth, origin of metastasis/histological subtype. A total of 48 tissue specimens were obtained from 41 different patients. Tissue consisted of normal brain samples ($n=7$), glioblastoma multiforme (GBM) brain samples WHO (World Health Organisation) grade IV ($n=5$) and metastatic brain samples ($n=29$). Table 1 displays further information about the tissue specimens.

Dewaxing and Haematoxylin and Eosin staining of tissue

Tissue sections on the microscope slides needed to undergo staining with haematoxylin and eosin (H&E) for parallel histological examination. The sections were de-waxed before staining, carried out by: 2 x 5 minute baths of HistoClear followed by 2 x 5 minute baths of ethanol. The tissue sections were washed in distilled water for 5 minutes after de-waxing, prior to H&E staining. Sections were bathed in haematoxylin for 5 minutes and then washed in warm tap water to allow the nuclei to turn blue. The sections were then covered in eosin for 4 minutes and rinsed with distilled water. Finally, the tissue sections were dehydrated in 2 x 5 minute baths of ethanol and cleared in 2 x 5 minute baths of histoclear, and then protected and preserved through the application of HistoMount and a coverslip. The sections were then microscopically examined in order to identify the metastatic sites present in the tissue.

Figure 1 shows the microscopic images of the H & E stained tissue samples at x 100 magnification. It can be observed that normal brain, metastatic and GBM brain tissue architecturally differ from one another and between the metastatic types.

Tissue section preparation for Raman spectroscopic analysis

The tissue sections on Raman substrates needed to be de-waxed prior to Raman analysis in order to reduce the paraffin peak contributions in the spectra. The de-waxing procedure consisted of 3 x 5 minute baths of HistoClear followed by 3 x 5 minute baths of

ethanol. The sections were left to air dry for 30 minutes, placed in a Petri dish and stored in a desiccator until spectroscopic analysis.

Raman spectroscopy instrumentation and analysis

Spectroscopic measurements were carried out using a Horiba Jobin-Yvon LabRAM HR800 spectrometer. An air cooled CLDS point mode diode 785 nm laser with a single edge filter (cut off to 100 cm^{-1}) and an output power of 300 mW was used to acquire spectra; which was used with a grating of 300 gr/mm and blazed at 1000 nm. Point spectra were acquired using a x 100 (Olympus MPlanN, NA = 0.9, spotsize $\sim 1\mu\text{m}$) objective and immersion point spectra were taken using a x 60 (Olympus LUMPlanFLN, NA = 1.0, spotsize $\sim 1.5\mu\text{m}$). Immersion spectroscopy was used for measurement of the tissue samples for spectral histopathology. Immersion Raman utilises an immersion lens which is in direct contact with a liquid that the sample under analysis is submerged in, such as deionised water used in this study. Bonnier *et al.* describe the use of immersion Raman spectroscopy and demonstrate its successful use for improving spectral quality^{34,35}.

The confocal hole was set at $100\text{ }\mu\text{m}$ for 785 nm spectral collections. The detector used was an Andor charged coupled device (CCD). A video camera within the Raman system was used to take images of the specimens. The instrumentation was calibrated before operation to silicon at the spectral line of 520.8 cm^{-1} . Spectra were acquired using the 785 nm laser at 100% exposure for 30 s and accumulated twice. From each tissue section 20 spectra were acquired from different regions, depending upon the size of the tissue slice.

For all tissue samples, sample analysis by spectral acquisition was carried out as it would be in the clinic. i.e all and any normal tissue was analysed, and no particular area was targeted (eg white/grey matter). Similarly, for tumoral sections, all cancerous areas were analysed irrespective of the origin of the structure, again mimicking clinical practice.

Data pre-processing

Pre-processing was carried out on the raw data using LabSpec 6 spectroscopy software suite (HORIBA Scientific, Japan) and MATLAB version 7.11.0 (R2010b) (The MathWorks, Inc., USA) using in-house written software. Pre-processing methods were kept to a minimum to enable better reproducibility; background subtracted was performed through the application of a fifth order polynomial and smoothed using 7 point smoothing (Labspec 6) and vector normalised (Matlab) using in-house written code.

Atomic force microscope (AFM)

The atomic force microscope (AFM) model that was used to image the samples for surface morphology for this study is the MFP-3D-BIO (Asylum Research, USA), with Olympus silicon AC160 cantilevers. The tips were 160 nm long with resonant frequencies typical of 320 kHz. A/C mode was employed for operation to reduce tip/sample.

Results and Discussion

Dewaxing efficiency of spectroscopic substrates

Raman spectra of the three substrates: low-E, Spectrosil and CaF_2 , were acquired under identical conditions to generate spectral ‘fingerprints’ of the substrates, shown in Figure 2, and thus ascertain the impact of their contribution to the spectral background.

It can be observed that low-E has the highest intensity baseline and CaF_2 has the lowest intensity baseline of the three substrates; indicating that spectra taken from samples on CaF_2 are less affected by substrate background than either low-E or Spectrosil and should display background peaks of lower intensities.

The spectra of dewaxed tissue samples on the three different substrates were compared to further investigate the level of influence substrate type has on the outcome of spectra. Figure 3 displays average spectra of dewaxed tissue on the three substrates and a paraffin spectrum for comparison

A paraffin spectrum displays significant peaks at 888 cm^{-1} , 1061 cm^{-1} , 1131 cm^{-1} , 1171 cm^{-1} , 1294 cm^{-1} , 1417 cm^{-1} , 1440 cm^{-1} , 1462 cm^{-1} (Figure 3), which can be assigned to C-C stretching and CH_2 and CH_3 deformations within the molecule²⁵. It can be seen from Figure 3 that the spectra from the dewaxed tissue samples on Spectrosil and CaF_2 exhibit residual paraffin peaks. However, dewaxed tissue spectra on low-E do not display visible paraffin peaks.

In order to further investigate any substrate effect on the dewaxing process, paraffin wax was analysed on the substrates without the presence of tissue specimens. Paraffin wax was cut at $10\text{ }\mu\text{m}$ sections and mounted onto the three different substrates. The substrates

were then dewaxed by the same method as the FFPP tissue samples and analysed; Figure 4 displays the resulting spectra. Residual wax, still present on both the Spectrosil and CaF_2 substrate, could be seen visually both macroscopically and microscopically, shown in Figure 5, and its presence was confirmed by paraffin peak contributions in their spectra. The low-E substrate did not retain any visual paraffin wax and no paraffin peaks were present in the 10 spectra taken from the substrate. This shows, for the first time, a substrate effect that occurs during the dewaxing process inferring that as a result of surface chemistry or morphology, low-E slides facilitate the removal of wax more readily than CaF_2 and Spectrosil. From Raman analysis and visual inspection, it is clear that, using the same dewaxing protocol, the low-E substrate is fully dewaxed, yet the CaF_2 and Spectrosil substrates retain paraffin wax.

Atomic force microscopy (AFM) was utilised to assess the three substrates' surface roughness. The AFM images of the three substrates are displayed in Figure 6, showing the surface morphology at a nanoscopic level. The low-E substrate was observed to have a far smoother surface than either CaF_2 or Spectrosil with an average surface roughness of 1.10 nm compared to 4.76 nm and 3.88 nm respectively. Low-E slides are coated with metal oxide³⁶; this could explain why their surface is far smoother than the other substrates which are only polished.

The clinical application of spectral histopathology is the ultimate aim of this field. As such, the adherence to current clinical process will be advantageous. The use of Low-E slides holds a number of advantages for this, such as low cost, their microscope slide size and robustness when compared to other substrates. Although substrate spectral background is

higher, all tissue spectral peaks that are detected when using other substrates are present in the spectrum.

Spectral Histopathology: Dewaxing Efficiency by Tissue Types

Although low-E substrates clearly perform better in terms of wax removal from the tissue sections using routine clinical protocols, CaF_2 is commonly used in Raman spectroscopic studies due to its low contribution to the spectral background (Figure 2). It is of interest to investigate whether the tissue type mounted on these substrates also contributes to the residual signals. The vector normalised mean Raman spectra of dewaxed sections of normal (157 spectra from 7 patients), metastatic (668 spectra from 29 patients) and GBM (127 spectra from 5 patients) brain tissue on CaF_2 substrates are displayed in Figure 7. It can be observed from the averaged spectrum of normal tissue that the paraffin peaks (asterisked peaks) are not fully removed by the dewaxing process, but notably the characteristic features are of a much lower intensity than those in the spectra of metastatic and GBM tissue Figure 8 shows the average intensity and standard deviation of the intense paraffin peaks at 1061, 1131 and 1294 cm^{-1} . As can be seen, there is a trend to greater paraffin retention in normal to the cancerous states, metastatic tissue retaining the most paraffin, after the same processing procedures. Further imaging studies are planned to examine the impact of the substrate upon paraffin retention, as there seems to be an interplay of tissue dependence and substrate dependence where the paraffin clumps upon the substrate surface, as can be seen in Figure 5.

Abnormal tissue can be of very different morphology than normal tissue. A difference in tissue density could provide an explanation for the inconsistency of the dewaxing efficiency, and thus the variation of paraffin peak intensity between the normal brain and

cancerous brain tissue spectra. For breast cancer Li *et al.* state that the amount of fibroglandular and adipose tissue is strongly related to the risk of developing cancer. They explain that, although no direct evidence has been found to link dense mammographic tissue with the increased chance of developing breast cancer, the correlations observed have encouraged the use of tissue density for breast cancer monitoring. They go on to support the observations of this correlation through their findings that the mammograms of cancerous breast tissue are far denser than those of normal breast tissue³⁷. Berrtholdo *et al.* correlate increased choline signals from Magnetic Resonance Spectroscopy as a measure of malignancy in brain tumours due to increased glial cell density as choline is a marker of cellular membrane turnover reflecting cellular proliferation³⁸. Indeed, it should be noted that, whereas in this study complete removal of wax was observed for tissue samples on low-E slides, O' Faoláin *et al.*³⁹ reported incomplete wax removal from normal parenchymal tissue from the placenta, dewaxed using a xylene based protocol also measured in low-E slides.

The results indicate that tissue processing still remains an issue for Spectropathology, particularly using Raman spectroscopy. For clinical relevancy, however, and indeed acceptance of the techniques by the clinical community, it is important that the sample preparation and measurement protocols for Raman spectroscopic analyses are consistent with current clinical practice. Choice of substrate for routine clinical analyses may be dominated by economic considerations, thus favouring low E slides. Paraffin embedding facilitates tissue cutting, but also is commonly employed, worldwide, for archiving tissue samples. The availability of a wide range of pathologically characterized samples for study potentially enables extensive retrospective studies using spectroscopic and other techniques. The embedding process and wax itself can, however, contribute significantly to the spectroscopic

signature of the tissue⁴⁰. An alternate method of “digital dewaxing” biological specimens to remove paraffin contributions of the spectrum has been proposed by Gobinet *et al.*, recognising that chemical dewaxing methods are known to be inefficient for the complete removal of wax in tissue and can cause alterations to the samples. Their method of dewaxing consists of an estimation of the paraffin sources in the spectrum using Independent Component Analysis (ICA), followed by a Non-negatively Constrained Least Squares (NCLS) method to subtract the contributions. This enables removal of the paraffin signals to allow analysis of the underlying tissue spectrum³³. However, although “digital dewaxing” has been demonstrated⁴¹, it is also often important to compare spectroscopic profiling with parallel histological analyses, requiring chemical dewaxing of sections, a process which adds to the sample variability. The observation of variable dewaxing efficiencies depending on tissue pathology adds complexity to the challenge, perhaps requiring a combination of established clinical dewaxing protocols with computational procedures.

Conclusion

This study shows the influence that Raman substrates have on resulting spectra from Raman analysis. Spectral backgrounds of the substrates show that the baseline of low-E is the highest and CaF₂ the lowest of the three substrates. It has been established through observation and investigation that CaF₂ and Spectrosil substrates retain paraffin wax after the dewaxing procedure is carried out whereas low-E does not. This is attributed to the difference in surface roughness and chemistry between substrates. AFM demonstrated that low-E substrates are far smoother than either CaF₂ or Spectrosil substrates with average roughness of 1.10 nm compared to 4.76 nm and 3.88 nm respectively.

This study has also observed the difference between the dewaxing efficiency between normal brain and cancerous brain tissue. This has been attributed to a change in density between normal and cancerous, which causes the denser cancerous tissue to retain wax better than the, less dense, normal tissue. It is important to note therefore that tissue processing procedures for spectral histopathology of normal tissue may not be optimised for abnormal regions.

Acknowledgements

The authors would like to acknowledge the support of the Sydney Driscoll Neuroscience Foundation, Rosemere Cancer Foundation, Brain Tumour North West, the Centre for Materials and Science at the University of Central Lancashire, the European Community Action Scheme for the Mobility of University Students and the Association of British Spectroscopists. The Focas Research Institute is supported through the National Biophotonics and Imaging Platform (NBIP) Ireland funded under the Higher Education Authority PRTL (Programme for Research in Third Level Institutions) Cycle 4, co-funded by the Irish Government and the European Union. The authors thank Dr Alex Henderson for the in-house written Matlab code, Dr Luke O'Neill, Focas Research Institute for assistance with AFM measurements and Mr Reece Hall for assistance with SEM/EDAX measurements.

References

1. X Prize.
2. S. Frankel, G. D. Smith, J. Donovan and D. Neal, *The Lancet*, 2003, 361, 1122-1128.
3. R. M. Hoffman and A. Y. Smith, *Asian J. Androl.*, 2011, 13, 369-373.
4. D. Hessels, H. G. Rittenhouse and J. A. Schalken, *EAU Update Series*, 2005, 3, 200-213.
5. J. B. Lattouf and F. Saad, *BJU Int.*, 2002, 90, 694-699.
6. S. S. Raab, D. M. Grzybicki, J. E. Janosky, R. J. Zarbo, F. A. Meier, C. Jensen and S. J. Geyer, *Cancer*, 2005, 104, 2205-2213.
7. D. I. Ellis, and R. Goodacre, *Analyst*, 2006, 131, 875-885.
8. S. E. Taylor, K. T. Cheung, Patel, II, J. Trevisan, H. F. Stringfellow, K. M. Ashton, N. J. Wood, P. J. Keating, P. L. Martin-Hirsch and F. L. Martin, *British journal of cancer*, 2011, 104, 790-797.
9. R. S. Da Costa, B. C. Wilson and N. E. Marcon, *Curr Opin Gastroenterol*, 2005, 21, 70-79.
10. M. G. Shim, L.-M. Wong Kee Song, N. E. Marcon and B. C. Wilson, *Photochemistry and Photobiology*, 2000, 72, 146-150.
11. T. C. Bakker Schut, G. J. Puppels, Y. M. Kraan, J. Greve, L. L. van der Maas and C. G. Figdor, *International journal of cancer. Journal international du cancer*, 1997, 74, 20-25.
12. J. Sulé-Suso, A. Forster, V. Zholobenko, N. Stone and A. El Haj, *Applied spectroscopy*, 2004, 58, 61-67.
13. F. M. Lyng, E. Ó. Faoláin, J. Conroy, A. D. Meade, P. Knief, B. Duffy, M. B. Hunter, J. M. Byrne, P. Kelehan and H. J. Byrne, *Experimental and Molecular Pathology*, 2007, 82, 121-129.
14. A. Podshyvalov, R. K. Sahu, S. Mark, K. Kantarovich, H. Guterman, J. Goldstein, R. Jagannathan, S. Argov and S. Mordechai, *Appl. Opt.*, 2005, 44, 3725-3734.
15. S. Koljenovic, L. P. Choo-Smith, T. C. Bakker Schut, J. M. Kros, H. J. van den Berge and G. Puppels, *Lab. Invest*, 2002, 82, 1265-1277.
16. C. Beleites, G. Steiner, M. G. Sowa, R. Baumgartner, S. Sobottka, G. Schackert and R. Salzer, *Vibrational Spectroscopy*, 2005, 38, 143-149.
17. R. Manoharan, K. Shafer, L. Perelman, J. Wu, K. Chen, G. Deinum, M. Fitzmaurice, J. Myles, J. Crowe, R. R. Dasari and M. S. Feld, *Photochem Photobiol*, 1998, 67, 15-22.
18. R. K. Dukor, M. N. Liebman and B. L. Johnson, *Cellular and molecular biology (Noisy-le-Grand, France)*, 1998, 44, 211-217.
19. M. J. Baker, E. Gazi, M. D. Brown, J. H. Shanks, N. W. Clarke and P. Gardner, *Journal of Biophotonics*, 2009, 2, 104-113.
20. D. C. Malins, N. L. Polissar and S. J. Gunselman, *Proc. Natl. Acad. Sci. USA*, 1997, 94, 259-264.
21. M. J. Baker, E. Gazi, M. D. Brown, J. H. Shanks, P. Gardner and N. W. Clarke, *British journal of cancer*, 2008, 99, 1859-1866.
22. M. Isabelle, N. Stone, H. Barr, M. Vipond, N. Shepherd and K. Rogers, *Spectroscopy* 2008, 22, 97-104.
23. M. J. Romeo and M. Diem, *Vib Spectrosc*, 2005, 38, 115-119.
24. C. Kendall, M. Isabelle, F. Bazant-Hegemark, J. Hutchings, L. Orr, J. Babrah, R. Baker and N. Stone, *Analyst*, 2009, 134, 1029-1045.
25. E. Ó Faoláin, M. B. Hunter, J. M. Byrne, P. Kelehan, H. A. Lambkin, H. J. Byrne and F. M. Lyng, *Journal of Histochemistry and Cytochemistry*, 2005, 53, 121-129.
26. E. Ó Faoláin, M. Hunter, J. Byrne, P. Kelehan, M. McNamara, H. Byrne and F. Lyng, *Materials Synthesis and Applications, Dublin Institute of Technology*, 2005, 38, 121-127.
27. F. Bonnier, A. D. Meade, S. Merzha, P. Knief, K. Bhattacharya, F. M. Lyng and H. J. Byrne, *Analyst*, 2010, 135, 1697-1703.
28. F. Bonnier, P. Knief, A.D. Meade, J. Dorney, K. Bhattacharya, F.M. Lyng, H.J. Byrne, *Proc. of SPIE-OSA Biomedical Optics*, 2011, SPIE Vol. 8087, 8087F

29. J. Filik, M. D. Frogley, J. K. Pijanka, K. Wehbe and G. Cinque, *Analyst*, 2012, 137, 853-861.
30. P. Bassan, J. Lee, A. Sachdeva, J. Pissardini, K. M. Dorling, J. S. Fletcher, A. Henderson and P. Gardner, *Analyst*, 2013, 138, 144-157.
31. M. Miljkovic, B. Bird, K. Lenau, A. I. Mazur and M. Diem, *Analyst*, 2013, 138, 3975-3982.
32. J. R. Hands, P. Abel, K. Ashton, T. Dawson, C. Davis, R. Lea, A. McIntosh and M. Baker, *Analytical and Bioanalytical Chemistry*, 2013, 1-9.
33. C. Gobinet, D. Sebiskveradze, V. Vrabie, A. Tfayli, O. Piot and M. Manfait,, *16th European Signal Processing Conference (EUSIPCO)*. 2008.
34. F. Bonnier, S. M. Ali, P. Knief, H. Lambkin, K. Flynn, V. McDonagh, C. Healy, T. C. Lee, F. M. Lyng and H. J. Byrne, *Vibrational Spectroscopy*, 2012, 61, 124-132.
35. F. Bonnier, A. Mehmood, P. Knief, A. D. Meade, W. Hornebeck, H. Lambkin, K. Flynn, V. McDonagh, C. Healy, T. C. Lee, F. M. Lyng and H. J. Byrne, *Journal of Raman Spectroscopy*, 2011, 42, 888-896.
36. P. Bassan, A. Sachdeva, J. Lee and P. Gardner, *Analyst*, 2013, 138, 4139-4146.
37. L. Li, Z. Wu, L. Chen, F. George, Z. Chen, A. Salem, M. Kallergi and C. Berman, *Conference proceedings : ... Annual International Conference of the IEEE Engineering in Medicine and Biology Society. IEEE Engineering in Medicine and Biology Society. Conference*, 2005, 3, 3253-3256.
38. D. Bertholdo, A. Watcharakorn, M. Castillo, *Neuroimaging Clinics*, 2013, 23(3), 359-380
39. E.O. Faolain, M.B. Huinte, J.M. Byrne, P. Kelehan. M. Mcnamara, H.J. Byrne, F.M. Lyng, *Vibrational Spectroscopy*, 2005, 38 (1-2), 121-127
40. E.O. Faolain, M.B. Huinte, J.M. Byrne, P. Kelehan. P. Lambkin, H.J. Byrne, F.M. Lyng Faolain, *J Histochem Cytochem*, 2005, **53**, 121-129
41. A. Tfayli, C. Gobinet, V. Vrabie, R. Huez, M. Manfait, O. Piot, *Appl Spectrosc*, 2009, **63**, 564-570

List of Tables and Figures

Table 1 Patient details with histological subtype and metastatic origin.

Figure 1 Microscopic images of H&E stained tissue samples of normal brain, metastatic (from oesophagus and stomach, breast, colon/rectum, lung and melanoma as labelled above) and GBM brain WHO grade IV (x 100). Scale bar represents 50 microns.

Figure 3 Averaged spectra of 458 CaF₂ acquisitions, 210 low-E acquisitions and 465 Spectrosil acquisitions from all tissue specimens and a background-subtracted spectrum of paraffin wax. The tissue spectra have been vector normalised and offset for visual clarity. The asterisks above the peaks correspond to the paraffin contributions.

Figure 4 Vector normalised, background corrected spectra of substrates after dewaxing from: 1 CaF₂ acquisition, 1 Spectrosil acquisition and 10 averaged low-E acquisitions. The spectrum of paraffin wax is included as a reference. The spectra have been appropriately scaled and offset for visual clarity.

Figure 5 Microscopic Raman images at x 10 of the substrate surfaces after dewaxing. Wax residuals can be observed on the CaF₂ and Spectrosil substrates. Scale bars represent 0.5 mm.

Figure 6 AFM images of Spectrosil, CaF₂ and Low-E substrates.

Figure 7 Averaged immersion spectra of 127 GBM acquisitions, 668 metastatic acquisitions and 157 normal brain acquisitions. Normal tissue spectrum is shown with its standard deviation in red (top), GBM tissue spectrum is shown with its standard deviation in green (middle), and metastatic tissue spectrum is shown with its standard deviation in blue (bottom). Spectra have been vector normalised, the backgrounds have been corrected using a 5th order polynomial fit and subtraction and 7 points of smoothing. The asterisks correspond to paraffin peaks from residual wax in the tissue.

Figure 8 The average intensity and standard deviation of three intense paraffin peaks at 1061, 1131 and 1294 cm⁻¹ for the three tissue types; Normal tissue (blue), Glioblastoma multiforme (red) and Metastatic brain cancer (green)

Table 1 Patient details with histological subtype and metastatic origin.

BTNW no.	Gender	DOB	Origin of Metastasis/histological subtype
119	F	26/06/1963	Breast
707	F	07/08/1945	Breast
756	F	15/03/1957	Breast
888	M	25/11/1948	Colon/rectum
985	M	05/02/1933	Melanoma
988	M	30/12/1949	Oesophagus & stomach
1001	F	20/12/1944	Lung
690 / 1012	F	25/10/1960	Breast
1004	F	03/09/1956	Breast
998 / 1010	M	25/07/1946	Colon
1020	F	05/06/1948	Breast
2	F	28/10/1937	GBM
3	F	22/09/1981	GBM
4	M	08/12/1942	GBM
5	F	29/10/1958	GBM
7	M	14/04/1939	Normal Brain
10	F	13/06/1929	GBM
78	F	24/09/1955	Lung
106	F	14/02/1965	Normal Brain
132	F	24/06/1943	Normal Brain
136	F	25/09/1956	Normal Brain
137	M	26/04/1944	Colon/rectum
164	M	10/04/1954	Oesophagus & stomach
184	F	21/11/1948	Lung
215	M	21/01/1973	Lung
274	M	12/07/1940	Colon/rectum
295	F	12/06/1936	Lung
358	M	08/05/1935	Melanoma
409	F	08/08/1925	Colon/rectum
444	M	30/01/1978	Normal Brain
509	M	11/02/1930	Melanoma
517	F	05/06/1955	Lung
521	M	18/01/1949	Oesophagus & stomach
562	F	12/03/1953	Lung
567	F	09/04/1947	Melanoma
668	F	30/08/1943	Colon/rectum
678	F	13/11/1961	Normal Brain
688	F	15/06/1965	Melanoma
694	M	18/09/1951	Lung
721	F	04/01/1976	Oesophagus & stomach
772	M	21/09/1972	Normal Brain

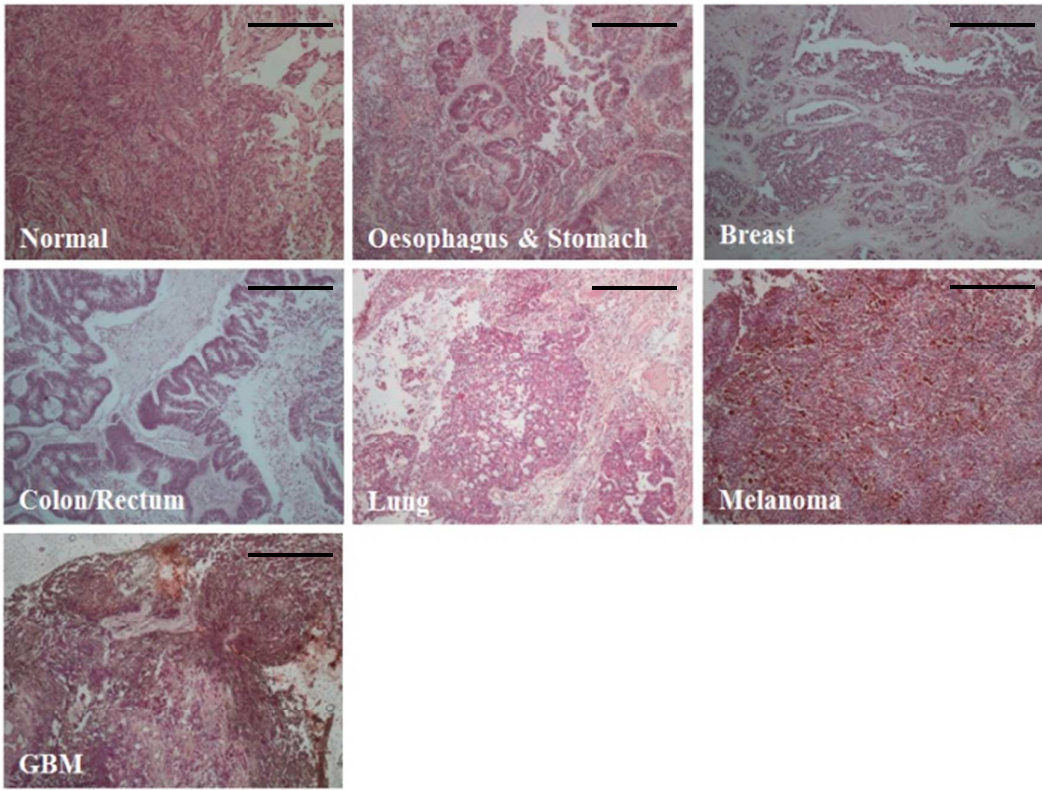


Figure 1 Microscopic images of H&E stained tissue samples of normal brain, metastatic (from oesophagus and stomach, breast, colon/rectum, lung and melanoma as labelled above) and GBM brain WHO grade IV (x 100). Scale bar represents 50 microns.

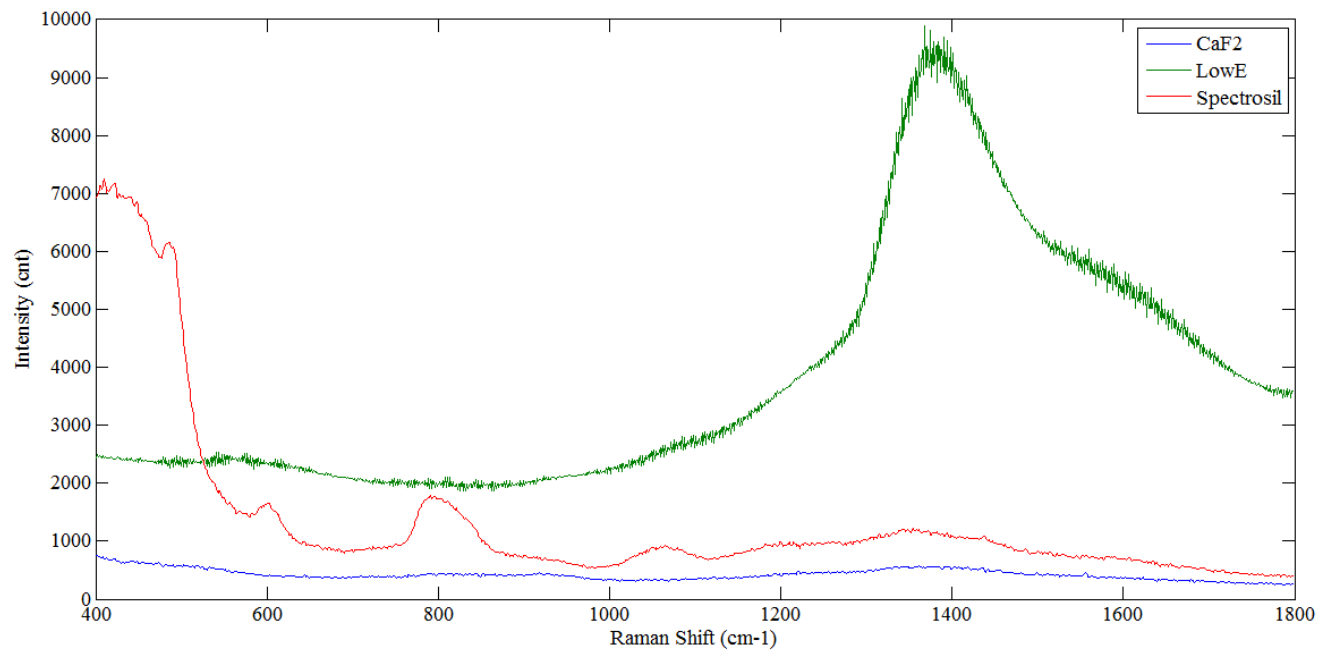


Figure 2 Raw spectra of the substrate backgrounds: CaF₂, low-E and Spectrosil.

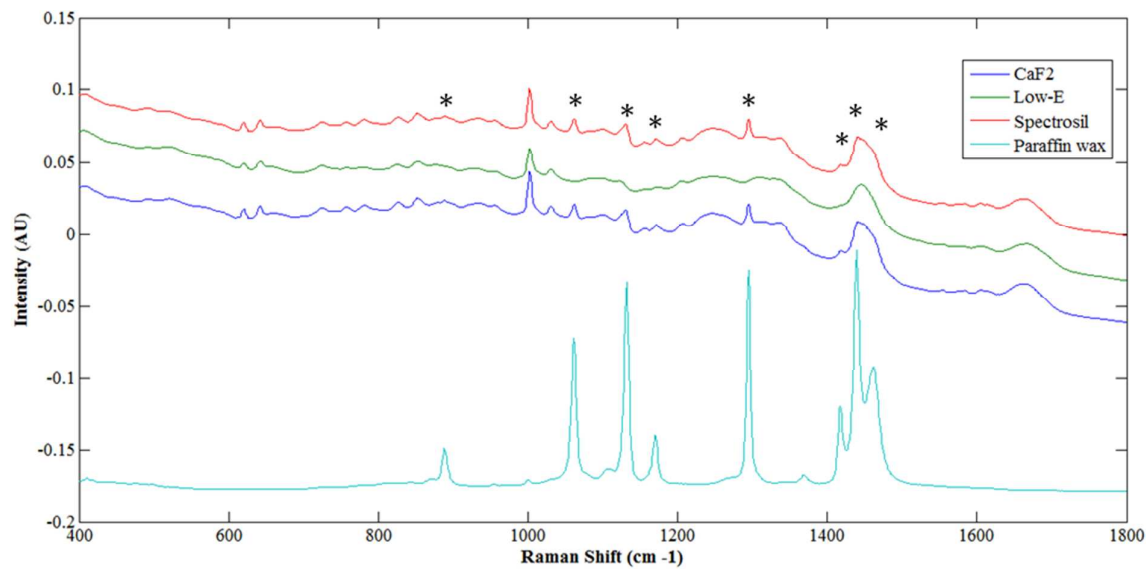


Figure 3 Averaged spectra of 458 CaF₂ acquisitions, 210 low-E acquisitions and 465 Spectrosil acquisitions from all tissue specimens and a background-subtracted spectrum of paraffin wax. The tissue spectra have been vector normalised and offset for visual clarity. The asterisks above the peaks correspond to the paraffin contributions.

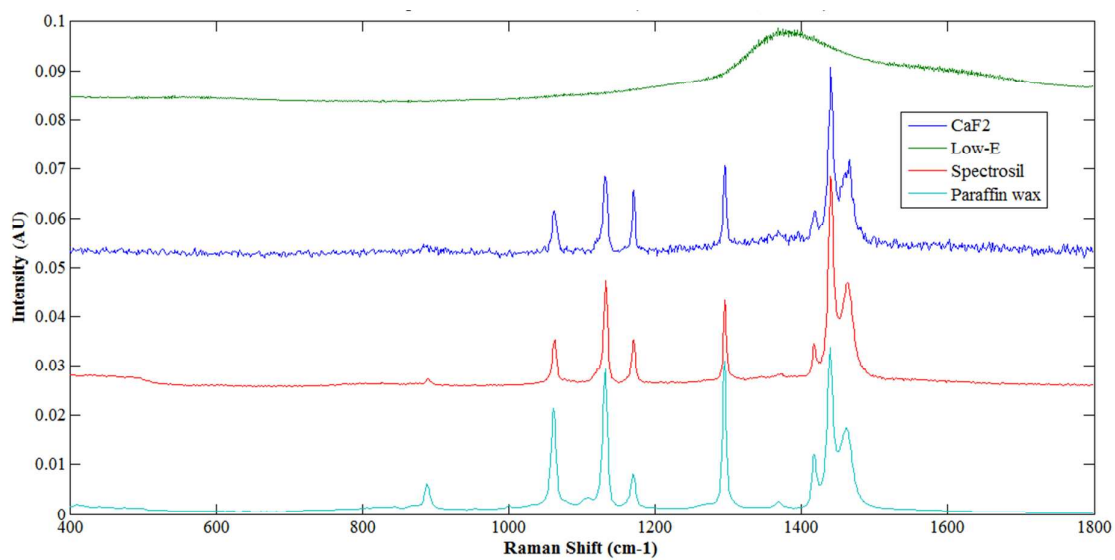


Figure 4 Vector normalised, background corrected spectra of substrates after dewaxing from: 1 CaF₂ acquisition, 1 Spectrosil acquisition and 10 averaged low-E acquisitions. The spectrum of paraffin wax is included as a reference. The spectra have been appropriately scaled and offset for visual clarity.

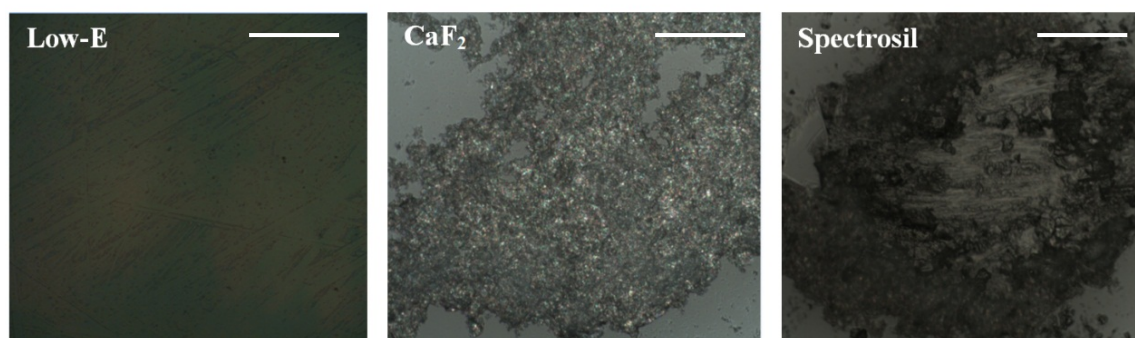


Figure 5 Microscopic Raman images at x 10 of the substrate surfaces after dewaxing. Wax residuals can be observed on the CaF₂ and Spectrosil substrates. Scale bars represent 0.5 mm.

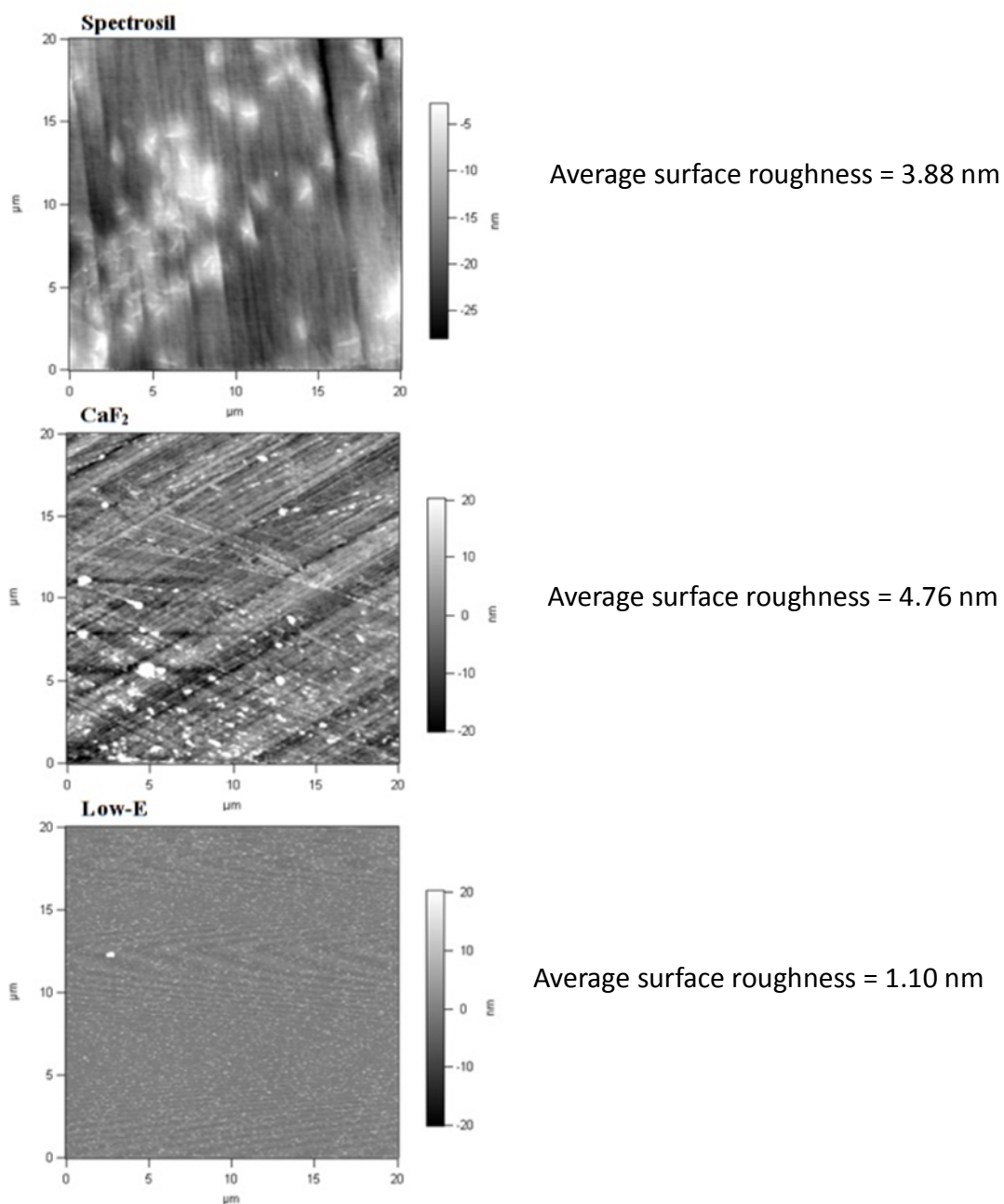


Figure 6 AFM images of Spectrosil, CaF₂ and Low-E substrates.

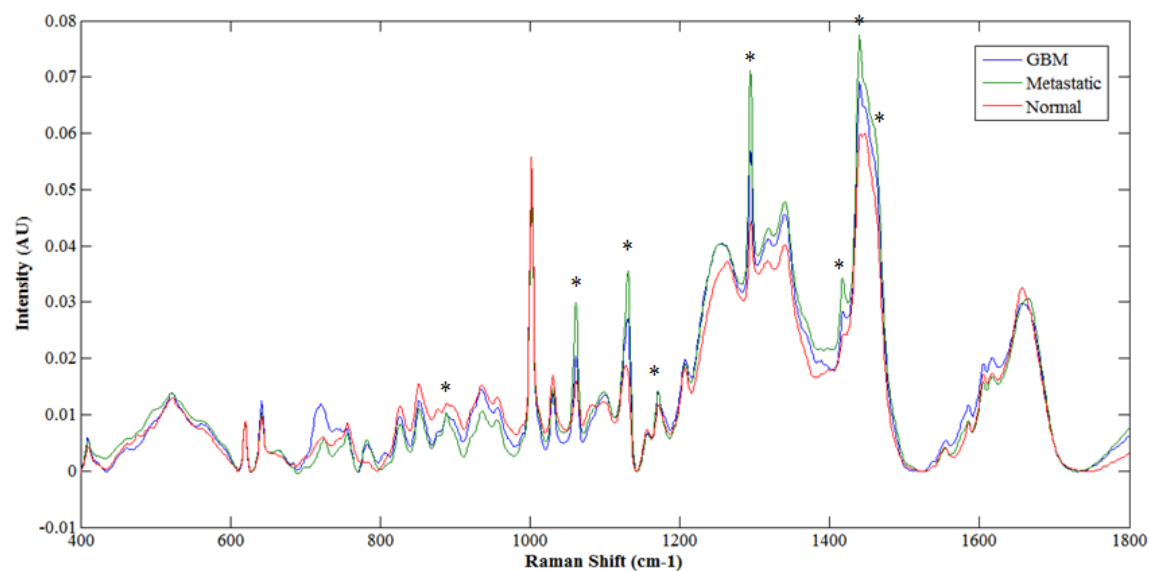


Figure 7 Averaged immersion spectra of 127 GBM acquisitions, 668 metastatic acquisitions and 157 normal brain acquisitions. Spectra have been vector normalised, the backgrounds have been corrected using a 5th order polynomial fit and subtraction and 7 points of smoothing. The asterisks correspond to paraffin peaks from residual wax in the tissue.

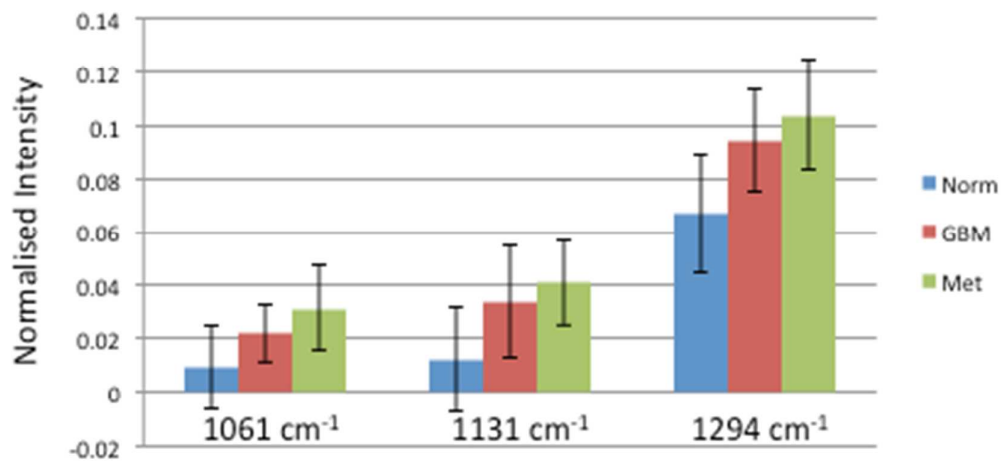


Figure 8. The average intensity and standard deviation of three intense paraffin peaks at 1061, 1131 and 1294 cm⁻¹ for the three tissue types; Normal tissue (blue), Glioblastoma multiforme (red) and Metastatic brain cancer (green)